**A FINITE ELEMENT EVALUATION OF AN EXPERIMENT**
**RELATED TO COATING DAMPING PROPERTIES**


THESIS


Armando DeLeon, Captain, USAF

AFIT/GA/ENY/09-M03


**DEPARTMENT OF THE AIR FORCE**
**AIR UNIVERSITY**

# *AIR FORCE INSTITUTE OF TECHNOLOGY*

**Wright-Patterson Air Force Base, Ohio**

# A FINITE ELEMENT EVALUATION OF AN EXPERIMENT RELATED TO COATING DAMPING PROPERTIES

THESIS

Presented to the Faculty

Department of Aeronautics and Astronautics

Graduate School of Engineering and Management

Air Force Institute of Technology

Air University

Air Education and Training Command

In Partial Fulfillment of the Requirements for the

Degree of Master of Science in Astronautical Engineering

Armando DeLeon, B.S.A.E.

Captain, USAF

March 2009

# A FINITE ELEMENT EVALUATION OF AN EXPERIMENT RELATED TO COATING DAMPING PROPERTIES

Armando DeLeon, BSAE

Captain, USAF

Approved:

_____          _____
Dr. Anthony N. Palazotto (Chairman)                                               Date


_____          _____
Dr. William P. Baker (Member)                                                         Date


_____          _____
Dr. Tommy George (Member)                                                           Date


_____          _____
Maj. Shad Reed (Member)                                                               Date

# Abstract

Typically turbine engine blades gain protection from thermal damage by the use of hard coatings, such as Magnesium Aluminate Spinel. Known as Thermal Barrier Coatings (TBC's), they have material properties that include several nonlinearities. It has been found that these TBC's create damping characteristics which are primarily due to their nonlinear dissipation of energy. In order to effectively represent their damping properties, it is necessary to create a method which combines experimentation and analysis. Previous work has shown the need for a beam bounded and loaded in such a fashion that external support energy dissipation functions i.e. boundary conditions and aerodynamics are eliminated. Thus, a new experimental apparatus and method was used to determine the nonlinear material properties of these materials. Investigators incorporated monofilament wires and magnets to approximate free-free boundary conditions. This allowed the non-linear damping properties of these materials to be approximated. This research included finite element analyses specifically created to put bounds on the experimentally developed material properties. Since prior work never established ranges of effective properties, the question that was addressed was how far off can a relationship be before it changes the overall result. Thus, this research varied several material parameters as well as experimental boundary conditions to evaluate their effect on the damping coefficients such as the loss factors as well as the material modulus.

# Acknowledgments

# Table of Contents

# List of Figures

# List of Tables

# A FINITE ELEMENT EVALUATION OF AN EXPERIMENT RELATED TO COATING DAMPING PROPERTIES

## I.  Introduction

### *Background*

Thermal Barrier Coatings (TBC) were first tested in turbine sections of gas turbine engines in the early 70's, leading to successful integration into designs by the 80's (Miller 1997).  Due to the extreme thermal and corrosive environments within a modern turbine engine, ceramic based coatings are the coating of choice and are used to extend the useful life of turbine blades.  Temperatures in the high pressure turbine are on the order of 1500°C.  This necessitates the coatings to be ceramic based which required new technologies to apply them successfully.  In addition to thermal considerations, the combustion waste gases produce a corrosive environment for the alloys used in modern turbine blades.  These coatings thus preserve and extend the service life of high pressure turbine blades.  Recently, a novel use of the coatings has been postulated.  In addition to using them for thermal and environmental protection, they could also be used for vibration protection throughout the different stages of the gas turbine.

*Damping*

The airflow through the modern turbine engine includes turbulence that creates low order vibrations. These vibrations can induce resonant frequencies leading to material fatigue. Of particular importance is High Cycle Fatigue (HCF). HCF is the largest cause of component failure in modern military gas turbine engines (Cowles, 1996). The atmosphere contains turbulence and in addition, the stator blades and dynamic turbine blades that make up the various stage of the engine itself create additional instabilities. Since these disturbances are inevitable, various methods are used in an attempt to attenuate the resulting vibrations. One of the basic strategies for dealing with these vibrations is to avoid aerodynamic excitation of the resonant frequencies in the engine components which lead to damage. (Blackwell, Palazotto, George, and Cross, 2007; Ivancic and Palazotto, 2005; Limarga, Duong, Gregori, and Clarke, 2007). This is done by minimizing the time that the engine operates in those power bands that tend to excite those resonant frequencies. These vibrations can also be reduced with damping. Damping reduces oscillations in vibratory system through dissipation of energy. Damping methods can be classified as either active or passive. The active methods include dampers and pads that act to dissipate energy (Limarga et al., 2007). However, these add mass and complexity to an engine and are not suitable for wide frequency ranges. The passive method is to use a coating that can act to dissipate energy over a band of frequencies. This method has the advantages of simplicity, less mass, and minimal maintenance. If the coatings can attenuate the magnitude of the vibrations then

the turbines service life would be significantly extended (Ivancic and Palazotto, 2005).

One of the ceramic coatings of particular interest due to its damping capacity is

Magnesium Aluminate Spinel.  It has been shown to have superior damping capacity

compared to other ceramic coatings (Shipton, M. and Patsias, S. 2003).  This coating was

tested in previous work and this research primarily evaluated the results of those

experiments (Reed 2007, Pearson 2008).


## *Experiment*


Clearly a passive damping method based on a hard ceramic coating shows

promise.  To date however there are still hurdles that need to be overcome before this

method can be widely employed.  Although these coatings provide a certain amount of

damping, quantifying that property has proven problematic.  One of the reasons that the

material properties of these coating materials is so hard to quantify is the fact that they

are coatings.  These materials are brittle and cannot be tested as standalone specimens.  In

order to qualitatively asses their properties, it is necessary to test coated specimens.  By

coating an underlying linear material of known properties, the coating properties can be

gleaned from experiments.  This is a phenomenological approach that gathers data and

attempts to use assumptions to create a model that describes the non-linear properties of

theses coatings.  This research utilizes data collected by Pearson (2008), who utilized a

procedure developed by Reed (2007).  Reed's experimental procedure followed previous

work that attempted to characterize the damping properties of mag spinel by various

methods (Blackwell, Palazotto, George, and Cross, 2007; Allen 2005; Lee 2006; Shipton, M. and Patsias, S. 2003).  Reed's work is based on linear assumptions to approximate the behavior of the coatings.

Over the course of several different experiments it has been shown that these type of materials display strain dependent damping and stiffness behaviors (Blackwell, Palazotto, George, and Cross, 2007).  Past work has also shown that boundary condition effects are of significance when performing vibration and damping experiments (Bishop, J. E. and Vinra, V. K. 1992).  In particular, the energy dissipation at the non-ideal boundary condition can lead to difficulties when characterizing the damping properties of mag spinel (Allen 2005).  In addition, studies have attempted to quantify the difference between performing characterizations in air and in a vacuum.  It has been shown that the air provides damping that pollutes the data collected regarding the damping properties of the coating (Allen 2005, Lee 2006).  Several of the coated samples looked at previously were chosen to be plates to allow common turbine vibrational modes to be investigated and to simulate the cantilevered condition of the turbine blades (Blackwell 2003).  In addition, repeatability has been a problem with regard to boundary conditions used with the plate (Lee 2006).  Also, the material has been shown to exhibit strain hardening dependent on cycle accumulation (Reed 2007).  All of these findings necessitated developing a different approach.

To address several of the shortcomings in previous attempts to characterize the damping properties of these ceramic coatings, Reed developed a procedure that incorporated both experimental and finite elements.  The experimental approach

consisted of a Ti-6Al-4V beam suspended by monofilament wires to approximate a free-free boundary condition while being excited with a magnetic couple. The objective was to excite the first bending mode in the beam to obtain consistent strain at the point of interest i.e. the center of the beam. This magnetic couple was achieved by attaching permanent magnets at one of the nodes and driving them with a wound magnet. This produced a moment in the beam that resulted in exciting the first bending mode. This was done in a vacuum chamber to minimize air damping. The coated beams were also initially excited for numerous cycles in an attempt to increase repeatability of results. The data collected using this set-up results in a Frequency Response Function that requires analysis to arrive at the properties of interest.

The experimental procedure can be used for forced response experimentation, free-decay or other techniques. Reed compared the results of various techniques using this set-up and based his results on the free-decay method. However, researchers favor the forced response method due to its ease of performing and simpler method of analyzing the data. Thus, Pearson (2008) followed that technique in his research. His results were heavily dependent on the half-power bandwidth method that underlies the forced response technique.

## *Experiment Results*

Results obtained by Pearson are comparable to the results obtained by Reed. Although there are differences, considering the simplicity in using the half-power

bandwidth versus the free-decay method, the approximations made, and the materials non-linear nature, the results were encouraging. However, the underlying linear assumptions, made by Reed (2007), in developing the procedure he followed were not tested. The results from both experiments could match and still be different than the true values by a significant amount. In addition, there was a discrepancy between the two experiments that merits further mention and that was the damping approximations of the uncoated Ti-6Al-4V beam. The loss factor recorded by Reed was 0.0004 using the free decay method versus 0.0008 measured by Pearson using the half-power bandwidth method. This research further investigated this difference and the results will be discussed in Chapter III.

## *Objective*

This research investigated the results of the experimentation and analysis done by Pearson. Particular attention will be focused on the parameters chosen in the Finite Element Model (FEM) used in the procedure as described in Chapter I. Reed (2007) and Pearson (2008) used the same finite element software package (ANSYS) and model. This research used the finite element software package ABAQUS in an attempt to verify the results of previous research by comparing results to Pearson's work. Once this was done, an investigation was accomplished that shows how variations in several material parameters affect the results. The differences will be evaluated as a sensitivity analysis in

order to evaluate how the differences in FE parameters affect the estimation of material properties. The next three chapters deal with:

1) the procedural steps taken with regard to the FEM to characterize the material properties of mag spinel

2) comparison to Pearson's results as well as an investigation into the effects of the sweep direction and sweep rates performed by Pearson (2008)

3) FEM development and input parameter variations to include springs to model the monofilament wires

The Chapter after these three will focus on applying a load to the FEM that simulates the magnetic couple used in the experiment. This will be done in an attempt to validate the linear assumptions made in characterizing the material properties using the free-free set-up developed by Reed (2007).

# II. Procedural Steps

*Motivation*

A procedure was previously developed that used data collected on a coated beam in conjunction with a FEM to approximate the material properties of the coating. As stated, the coating material does not lend itself to direct testing, thus the need for a coated specimen. Since, the coating's properties are non-linear; the coated material needs to be linear. Otherwise, it would be extremely difficult to extract the different properties of the two materials. In addition, the need for an approximate free-free condition was shown in previous work (Allen 2005). Clamped boundary conditions tended to dissipate energy causing difficulties in separating out the damping properties of the coating. Finally, a vacuum chamber was used because air was also shown to provide damping and made it problematic to characterize the damping due to the coating. This experimental procedure was an attempt to address those concerns.

The experiment conducted by Reed and Pearson provided velocities at the center of the specimen as an input voltage's frequency was varied. Eighteen voltages were considered for three different specimens per coating for a total of 108 tests. Unfortunately, this information is not enough to characterize the coating properties. The FEM provided data that was impractical to collect within the experiment. The material properties of interest were the coating modulus and coating loss factor ($\eta_{coat}$) as functions of strain. The coating modulus was inferred based on its effect on experimental

frequency. The output of the FEM was compared to the experimental results while varying the model's coating modulus. This allowed the coating modulus to be approximated in conjunction with the associated strain as explained in more detail below. In addition the strain energy of the system is predicted by the FEM which is used to calculate $\eta_{coat}$. In previous work done by Reed and Pearson, a FEM was constructed using the commercial finite element software ANSYS. This model was used in an iterative fashion in conjunction with experimental data to approximate the material properties of mag spinel. During this research, a new FEM was created using the commercial finite element software ABAQUS.

## *Experimental Setup*

This Section will discuss the various items required to perform the experiment conducted by Pearson. All of the Figures (1-6) in this section are from Pearson's work (Pearson 2008). A more detailed experimental procedure can be found in Pearson's work (Pearson 2008). Figure 1 shows an overview of the experimental setup including the Laser Doppler Vibrometer (LDV), used to measure the velocities experienced by the center of the specimen. The vacuum chamber was able to achieve pressures of 25 torr, approximately 1/30th of the atmospheric pressure, and was used to minimize damping by the air. This has been shown to contribute significant damping in past experiments (Allen 2005, Lee 2006). The software and hardware system, VibrationVIEW 8500, was used in the experiment and it produced, and could vary, a sinusoidal signal while also

collecting the LDV output (*VibrationVIEW*2007).  The sinusoidal signal was amplified

and sent to a magnetic coil, as seen in Figure 2.  This coil accelerated the permanent

magnets seen in Figure 3 through magnetic induction creating a couple that excited the

first bending mode in the specimen.  VibrationView was used to vary the frequency and

voltage of the input signal.  The frequency was varied either from high frequencies to low

frequencies, or vice versa.  When the frequencies are changed from higher to lower it is

referred to as a downsweep.  The other direction is referred to as an upsweep.  Both

directions were accomplished in the experiment.

During testing, the specimen is supported by low gauge monofilament wire at the

bending nodes, as can be seen in Figure 4.  The low gauge monofilament wires were

connected to supports via clamps which were tightened to reduce specimen motion.  In

this way, a free-free condition was approximated.  The specimen can rotate freely about

the wires but it is restrained from movement in the longitudinal and the transverse

direction.

The specimen is excited at its first bending mode by the magnetic coil through a

series of frequencies as controlled by VibrationVIEW.  During this time, the LDV is

measuring the response as velocity changes at the center of the beam.  The frequency

sweep includes the resonance frequency of the specimen.  The result of one frequency

sweep at a voltage 50mV is shown in Figure 5.  This frequency response function (FRF)

is the output from VibrationView and shows the specimen's response (at its center) to an

input frequency.  As the frequency is changed, there are transient responses that must be

allowed to settle out of the specimen before the frequency can be changed.  This puts a

limit to the time it takes to perform a sweep.  The data that is investigated in this research

was obtained at a sweep rate of 2 Hz per minute.  This means that it took sixty seconds to

go from a frequency of 200 Hz to 202 Hz.  However, 2000 points were recorded over the

entire sine sweep with a data point taken every 0.005 Hz.  The time spent at each of those

points was inversely proportional to the total number of points.  There was an

investigation done to ensure that there was time for the transients to settle, to an

acceptable level, prior to collecting data (Pearson 2008).

There were 18 voltages tested for each specimen.  At each voltage, each

downsweep  and upsweep resulted in a FRF.  Both bare and coated specimens were tested

with a few differences.  The bare beam was tested at lower voltages due to the lightly

damped nature of Ti-6Al-4V.  The velocities of the bare specimens greatly exceeded the

coated specimens although the experiment remained within the elastic region since the

yield stress for Ti-6Al-4V is 980 MPa (*MatWeb material property data* 2008), which

corresponds to a strain value of 8900με.

The history effects of mag spinel was investigated by both Pearson (2008) and

Reed (2007) where it was shown that the response of the material was strongly influenced

by its history.  The specimen's coated with mag spinel were cycled prior to testing.  This

refers to the process of performing frequency sweeps at a near constant strain for a large

number of oscillations.  The specimens coated with mag spinel were cycled for nearly 4

million cycles (Pearson 2008).  The specimens exhibited strain hardening during cycle

buildup but exhibit strain softening with increasing voltage, as shown in Figure 6.  The

curve with the smallest amplitude correlates to the lowest voltage, as the voltage is

increased; the resulting curve amplitude increases correspondingly. The specimens were tested in an uninterrupted manner until the 18 voltage tests were complete in order to minimize any effects due to "resting" of the coating material (Pearson 2008). Three specimens coated with mag spinel were tested (Pearson 2008). This research investigates the results of analyzing one of those specimens. The specimen labeled #9 was chosen for this study because the results it produced were between the other two, with the assumption that its properties would be the most attributable to the coating itself and not skewed by some unknown effect.

The experiment presents certain variations that will be considered in this and subsequent chapters such as:

- positions of node points

- wrap around of the coating

- sweep rate and direction

- determination of the monofilament wires effect

An attempt was made to characterize the effect of these variables on the coating modulus, loss factor, and strain results determined in the previous work.
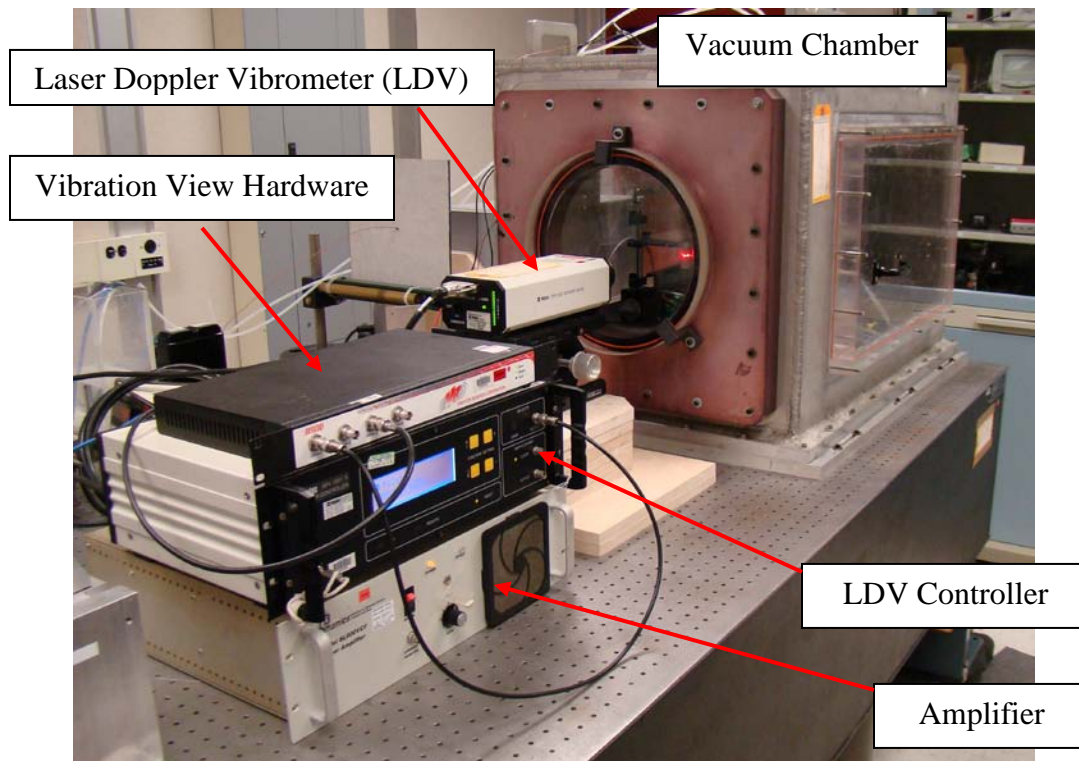
**Figure 1: Experimental Setup**
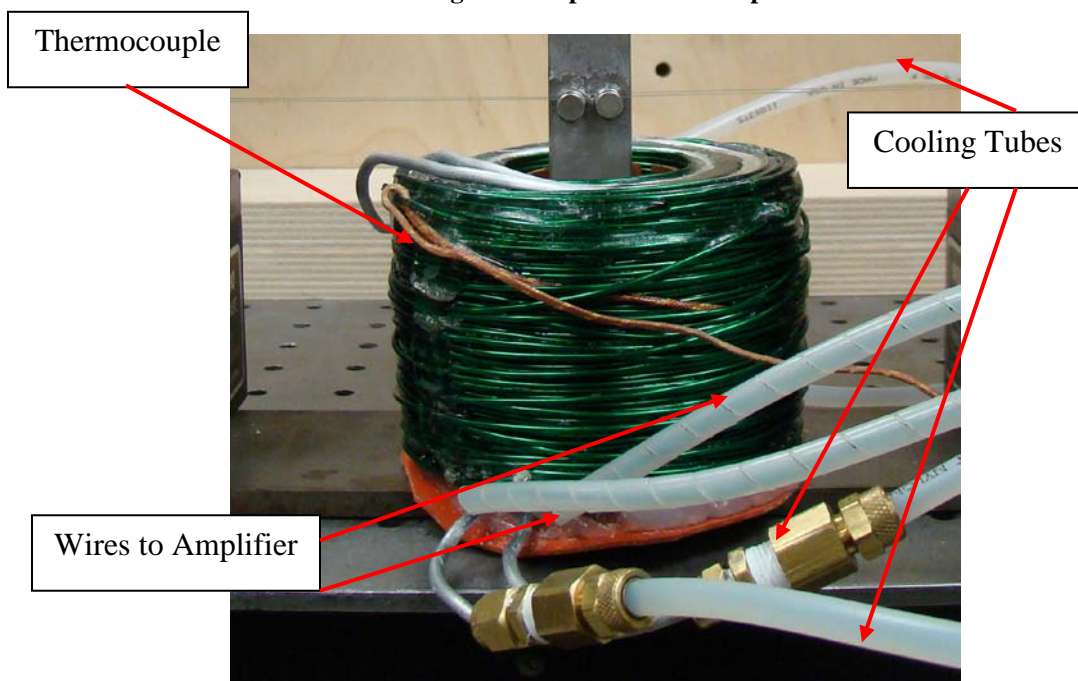


**Figure 2: Magnetic Coil**
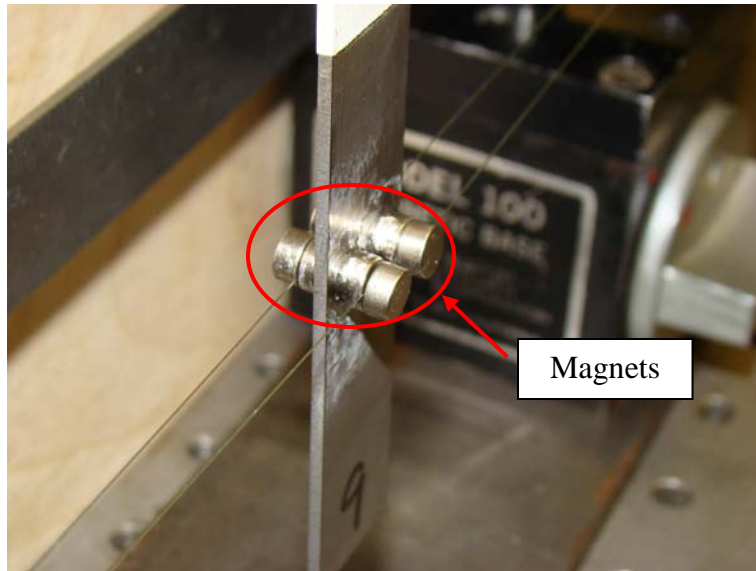
**Figure 3: Rare Earth Magnets**
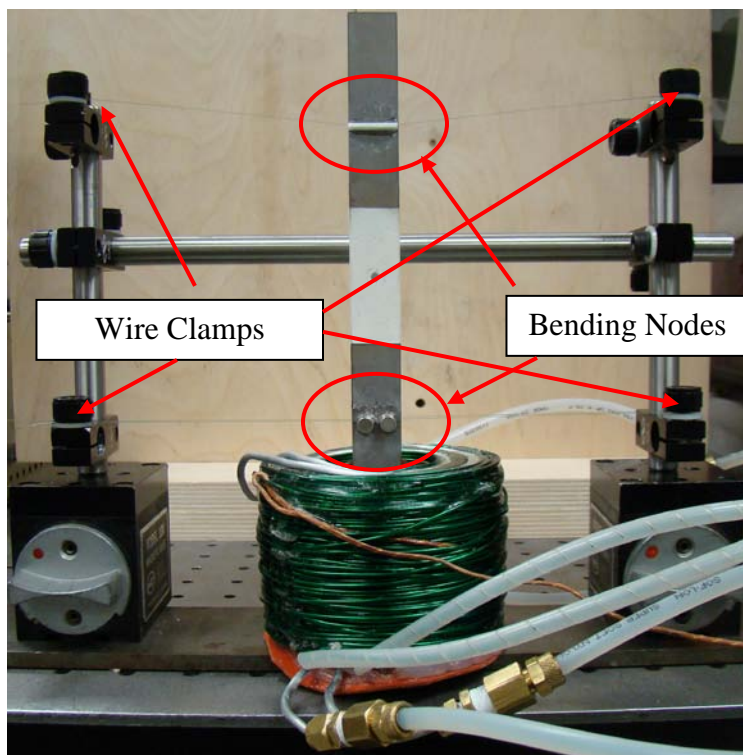


**Figure 4: Specimen Supports**
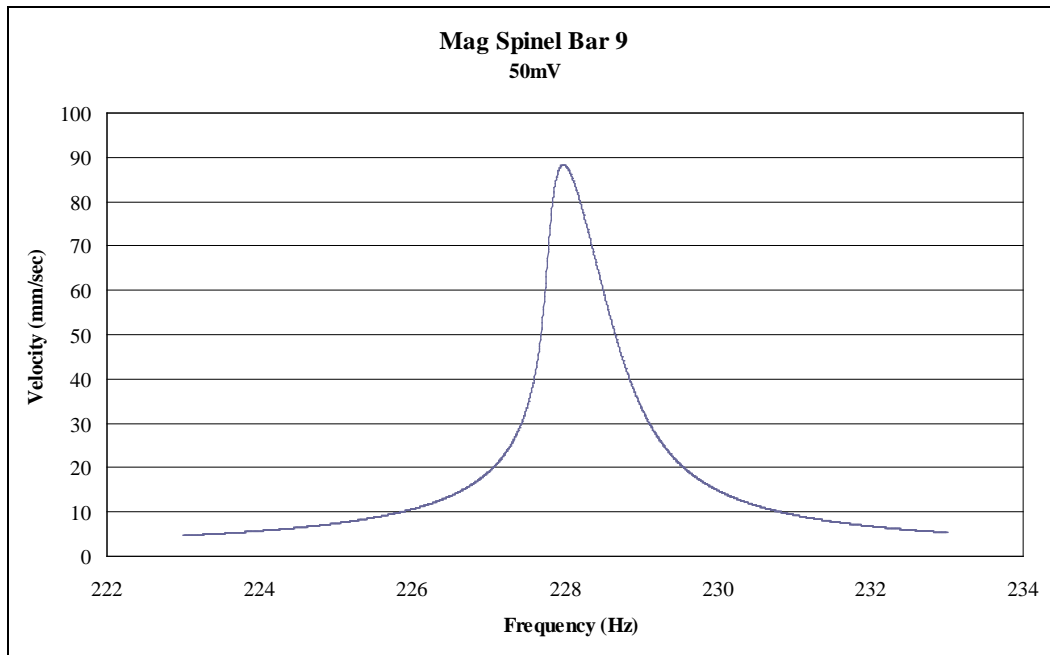
**Figure 5: Experimental FRF**
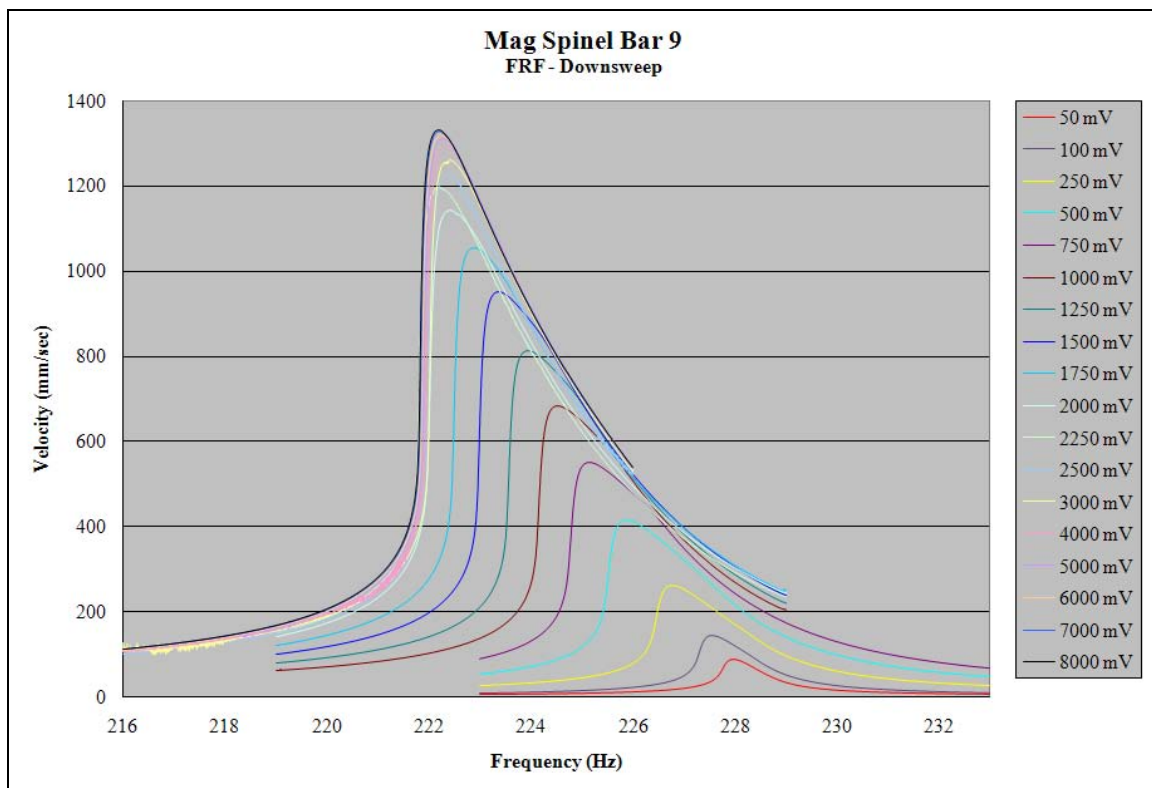


**Figure 6: Eighteen tested voltages**

## *Procedure*

In the previous section, a description was carried out on how the experiment was conducted and what data was collected. In order to characterize the material properties additional information is required. This information is obtained by extracting values from a FEM. Finite elements modeled the Ti-6Al-4V beam, the attached magnets, and the coating. The details of the modeling can be found in Chapter IV. The rest of this Section will detail the procedure used to approximate the material properties of the coatings using one experimental specimen.

The first step in this procedure is to perform a finite element analysis for each of the coating modulus ($E_c$) values listed in Table 1. The values of $E_c$ were chosen due to previous work as well as the results of the experiment. A frequency extraction is done with output consisting of eigenvalues and eigenfunctions. The eigenvalues are otherwise known as the natural frequencies of the system and are unique values. Each frequency corresponds to one eigenfunction. These are the natural modes of the system and only their shape can be determined uniquely. It is through this shape that we can determine the frequency of relevance to the experiment. The experiment was interested in the first bending mode. This is the shape that appears in Figure 7. The frequency of this mode shape is listed in Table 1 with Table 2 describing the symbols used. The frequencies listed were close to the frequencies seen in the experiment. If different frequencies had been observed in experiment then, the $E_c$ values would have changed accordingly.

**Table 1: Output FEM**

| $E_c$ (Gpa) | $f_n$ (Hz) | $x_{(L/2)}$ | $\varepsilon_{11}$ | $U_{sys}$ | $U_{coat}$ | SER |
|---|---|---|---|---|---|---|
| 35 | 216.18 | -0.537 | 287.10 | 9.52 | 1.79 | 0.188 |
| 40 | 218.36 | -0.533 | 280.87 | 9.71 | 1.96 | 0.202 |
| 45 | 220.45 | -0.530 | 274.91 | 9.88 | 2.12 | 0.214 |
| 50 | 222.44 | -0.527 | 269.19 | 10.05 | 2.26 | 0.225 |
| 55 | 224.34 | -0.523 | 263.71 | 10.20 | 2.39 | 0.234 |
| 60 | 226.16 | -0.520 | 258.44 | 10.35 | 2.50 | 0.242 |
| 65 | 227.90 | -0.517 | 253.38 | 10.49 | 2.61 | 0.249 |
| 70 | 229.58 | -0.514 | 248.51 | 10.62 | 2.71 | 0.255 |

**Table 2: Nomenclature**

| Symbol | Value |
|:------:|:------|
| $f$ | Frequency produced by FEM for first bending mode |
| X | Normalized Displacement produced by FEM for first bending mode, measured at node at center of beam at interface of coating and beam |
| $\tilde{\varepsilon}$ | Normalized Strain produced from FEM for first bending mode, measured at node at center of beam at interface of coating and beam |
| L/2 | Center of beam |
| $U_{coat}$ | Strain Energy of the coating, measured element by element |
| $U_{sys}$ | Strain Energy of the entire system to include the beam, coating, and magnets, measured element by element |
| SER | Strain energy ratio $U_{coat}/U_{sys}$ |
| $\delta$ | Displacement of the actual specimen in the experiment as measured by the LDV at the center of the beam |
| $\lambda$ | Scaling factor that allows the normalized strains produced by the FEM to be scaled to the actual values measured in the experiment. Computed by comparing the normalized displacements to the actual displacements |
| $\eta_{bare}$ | Loss factor of bare beam, calculated using the half-power bandwidth and equal to twice the damping ratio $\zeta$ |
| $\eta_{sys}$ | Loss factor of the system, calculated using the half-power bandwidth method and equal to twice the damping ratio $\zeta$ |
| $\eta_{coat}$ | Loss factor of the coating estimated using Equation 6 (Reed 2007) |
| $\varepsilon$ | Strain that has been scaled by using the normalized strain produced by the FEM and multiplying it by the scaling factor |
| $E_c$ | Young's modulus of the coating |

**Center of Specimen**

ODB: 48GPa_Constrained.odb   Abaqus/Standard Version 6.8-2   Sat Jan 24 13:56:39 Eastern Standard Time 2009

Step: Step-1
Mode     4: Value =  1.94993E+06 Freq =   222.24   (cycles/time)
Deformed Var: U   Deformation Scale Factor: +2.082e+01

**Figure 7: FEM Coated**



**Point of Interest: Interface**

ODB: Units_Check.odb   Abaqus/Standard Version 6.8-2   Thu Feb 05 07:29:25 Eastern Standard Time 2009

Step: Step-1
Mode     1: Value = -3.84229E-04 Freq =   0.0000   (cycles/time)

**Figure 8: FEM Point of Interest**

Since the amplitude of the eigenfunction is unknown, the mode shape is normalized.  By comparing the displacement at the center of the mode shape (X(L/2)) to the displacement that the actual specimen underwent in the experiment, it is believed that the output of the FEM can be "scaled".  Thus the FEM strain can be used in place of data collected by experiment.

Strains are normally measured with a strain gages.  In previous work, there were concerns concerning any adhesive contaminating the coating possibly resulting in changed damping properties (Reed 2007).  The FEM strains were corroborated by placing a strain gage on the bare portion of the specimen although interference from the magnetic coil was noted (Reed 2007).  The strain in the longitudinal direction is $\varepsilon 11$ and it is calculated from taking the nodal value at the interface between the coating and the titanium beam.  This strain value is calculated from the eight elements that connect to the node.  This is discussed further in the Chapter IV.   The loss factor can be simply and accurately measured by using the strain energy method (Johnson, Kienholz, and Rogers 1981).  This involves obtaining the elastic strain energy of both the system as well as the coating using finite element analysis.  The Strain Energy Ratio (SER) is calculated from the coating elastic strain energy ($U_{coat}$) and the total system elastic strain energy ($U_{sys}$) using Equation 1 (Reed 2007).

$$SER = \frac{U_{coat}}{U_{sys}} \qquad\qquad \textbf{(1)}$$

Thus, we see the reasons for the particular values extracted from the FEM and listed in Table 1. Figure 9 shows a graphical overview of the entire procedure used to approximate the material properties of the coatings.

The LDV took velocity readings at the center of the specimen. This was the location of the maximum strain in the specimen as it underwent its first bending mode. There was interest in obtaining higher strains due to a dearth of data for mag spinel above $500\mu\varepsilon$ (Reed 2007). Figure 7 and Figure 8 show both the position of the LDV reading as well as the position of interest. The strains at the interface are of particular interest since this is the convention used by previous researchers (Reed 2007). The linear nature of the Ti-6Al-4V beam is what allows the non-linear coating properties to be approximated. It should be noted that care was taken to ensure that the strains experienced by the beam did not exceed the yield stress of the Ti-6Al-4V. This would lead to deformations such that linear behavior could no longer be expected from the beam. Between the need to understand mag spinel's behavior at higher strains, and the need to remain in the elastic region of Ti-6Al-4V this is where the experiment attempted to excite the specimen. The steps taken in the procedure are now covered in further detail.

Iterate $E_c$

Run FEM

Extract Values
Frequency of First Bending Mode, $f$
Normalized Displacement (X) @ L/2
Normalized Strain $(\tilde{\varepsilon})$ @ L/2
Strain Energy of the Coating $(U_{coat})$
Strain Energy of the System $(U_{sys})$

$$SER = \frac{U_{coat}}{U_{sys}}$$

Resulting Values

$E_c$

$\eta_{coat}$

$\varepsilon$

Calculate, $\eta_{coat}$

$$\eta_{coat} = \frac{\eta_{sys}(SER+1) - \eta_{bare}}{SER}$$

Calculate, $\varepsilon$

$$\varepsilon = \lambda\tilde{\varepsilon}$$

Calculate, $\lambda$

$$\lambda = \frac{\delta}{X}$$

Polynomial Relationships:
$E_c$ vs. $f$
X vs. $E_c$
$\tilde{\varepsilon}$ vs. $E_c$
SER vs. $E_c$

Experimental Values
$\eta_{sys}$

$$\delta = \frac{\text{Velocity}}{f \times 2\pi}$$

**Figure 9: Overview of Procedure**

The first step of the procedure is to select and enter an $E_c$ into the material properties definition in the FEM for the coating. After extracting the values listed in Table 1 (with the exception of SER which is calculated) a new $E_c$ is entered and the FEM is re-analyzed. Thus, Table 1 is a compilation of several analyses with different $E_c$'s. $E_c$ can now be plotted versus the frequency also extracted from the FEM. A polynomial relationship is thus established between $E_c$ and frequency. The following polynomials are approximately linear. A cubic spline or other interpolating function would provide slightly better accuracy. The output of the FEM is only dependent on the input thus the resulting data points should be considered valid with the values between them requiring interpolation. In addition, the values used in the plot should be normalized in order to investigate the coefficients of the polynomial for behavior approaching linear behavior.

22

Although the polynomial shown in Figure 10 appears to have a coefficient of the quadratic term that is orders of magnitude smaller than the other terms, the units involved make that determination more difficult. The effects of the magnets cause the results to deviate slightly from a line. This polynomial will be useful for establishing the $E_c$ values related to the experimental frequencies. The frequencies output by the FEM are not the same ones seen in the experiment, although they are close. It must be noted that it is assumed that there exists a one for one correspondence between $E_c$ and natural frequency. If the $E_c$ corresponds to more than one natural frequency then this assumption is invalid and this technique would lead to inaccurate material properties.
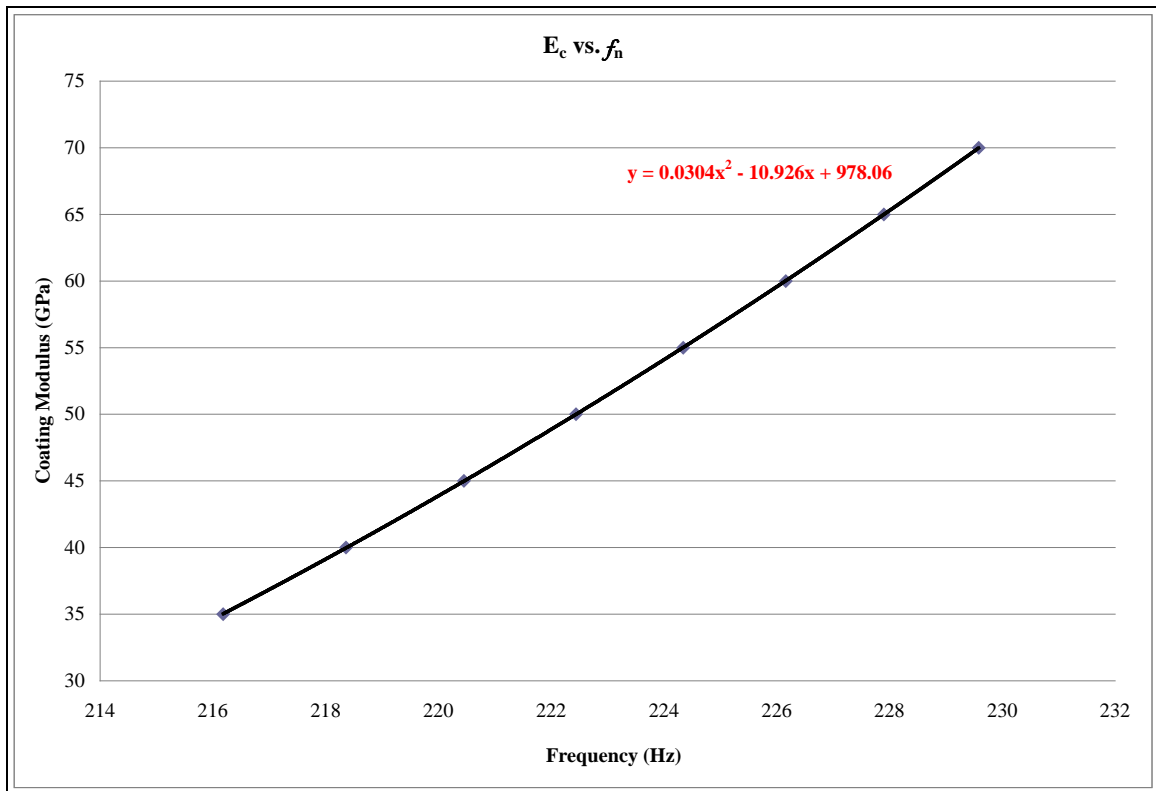


**Figure 10: Coating Modulus vs Frequency**

Using the FEM output, we next plot $X\left(\frac{L}{2}\right)$ from the mode shape versus the values

input for $E_c$. This is shown in Figure 11. This establishes the relationship between these

displacements and $E_c$ through a different polynomial. This follows the same assumption

as stated previously. If more than one mode shape exists for a particular $E_c$ then this

would lead to further error in the calculations of the material properties. The FEM cannot

be relied on as a check on the linear assumption. The material properties input into the

software correlated to a linear elastic model and so could not corroborate the linear

assumptions. These linear assumptions were necessary to the technique and have been

used to approximate the non-linear properties of materials in the past (Reed 2007).

**Normalized Displacement vs. E$_c$**

$y = -2E\text{-}06x^2 + 0.0009x - 0.5657$
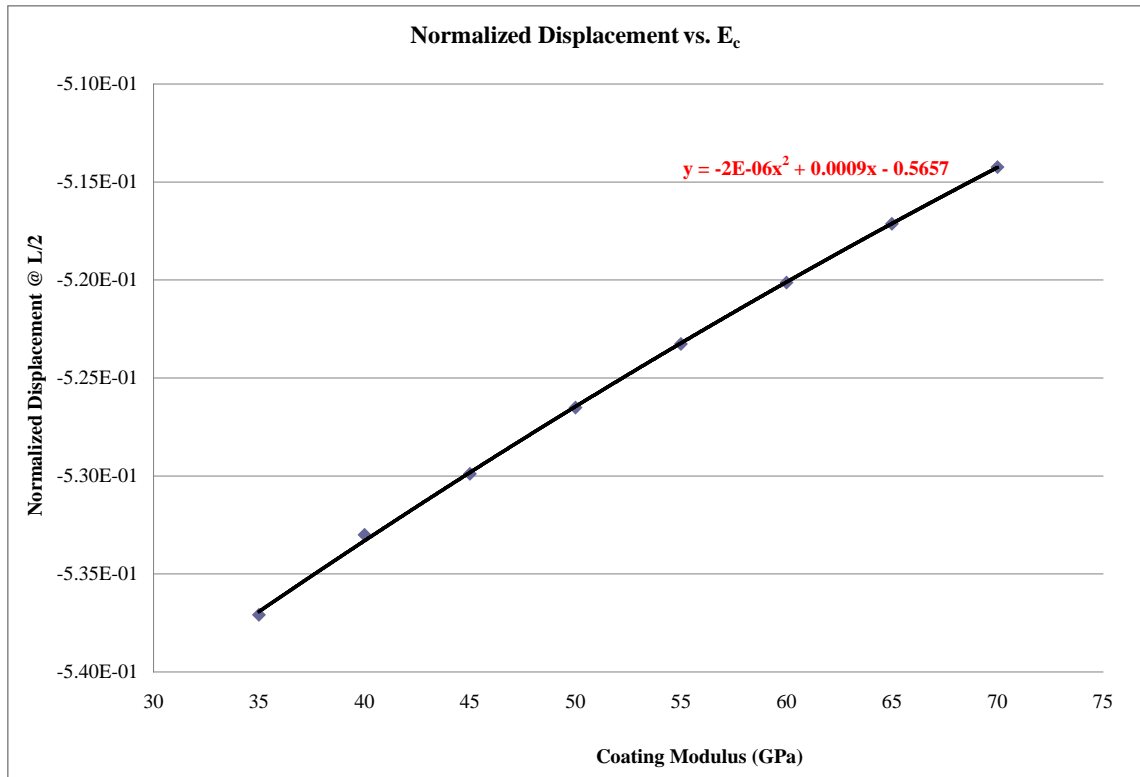
**Figure 11: X vs Coating Modulus**

The strains extracted from the FEM are normalized since the amplitude of the mode shape is undetermined. This normalization preserves the strains as related to the mode shape with the strains at the coating-beam interface of particular interest as stated earlier. These are the normalized strains $\varepsilon_{11}$ which are similarly plotted versus the values input for $E_c$ in Figure 12. This polynomial develops a useful relationship between the two quantities. We are thus able to compute a normalized $\varepsilon_{11}$ for a given $E_c$. Since the frequencies produced by the FEM for each $E_c$ input do not correspond exactly to the experimental frequencies, the extracted normalized strains must be "adjusted" to correlate to the actual frequencies.

**Normalized $\mu e_{11}$ vs. $E_c$**

$$y = 0.0045x^2 - 1.575x + 336.66$$
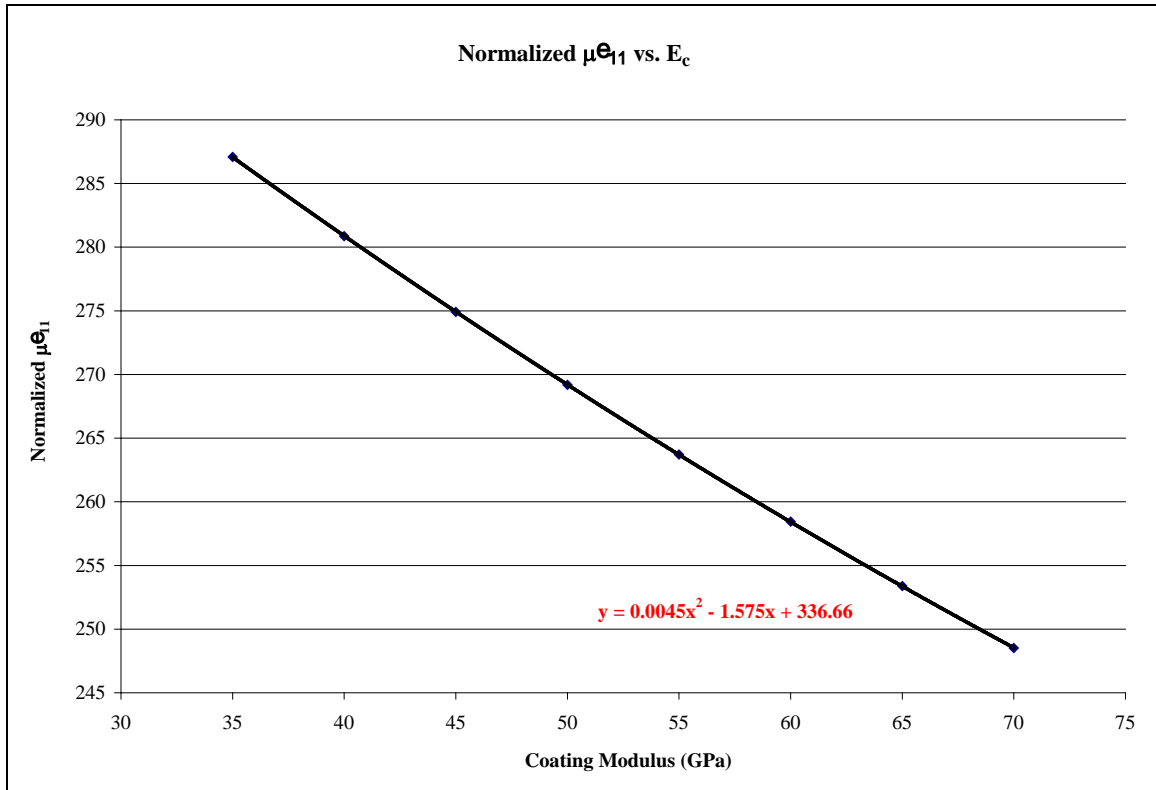


**Figure 12: Normalized $\varepsilon_{11}$ vs. Coating Modulus**

Our last polynomial relationship is developed from plotting the SER versus the values input for $E_c$ as shown in Figure 13. As discussed earlier, the SER along with experimental data will allow us to calculate $\eta_{coat}$.



**SER vs. $E_c$**

$y = -3E-05x^2 + 0.0058x + 0.094$
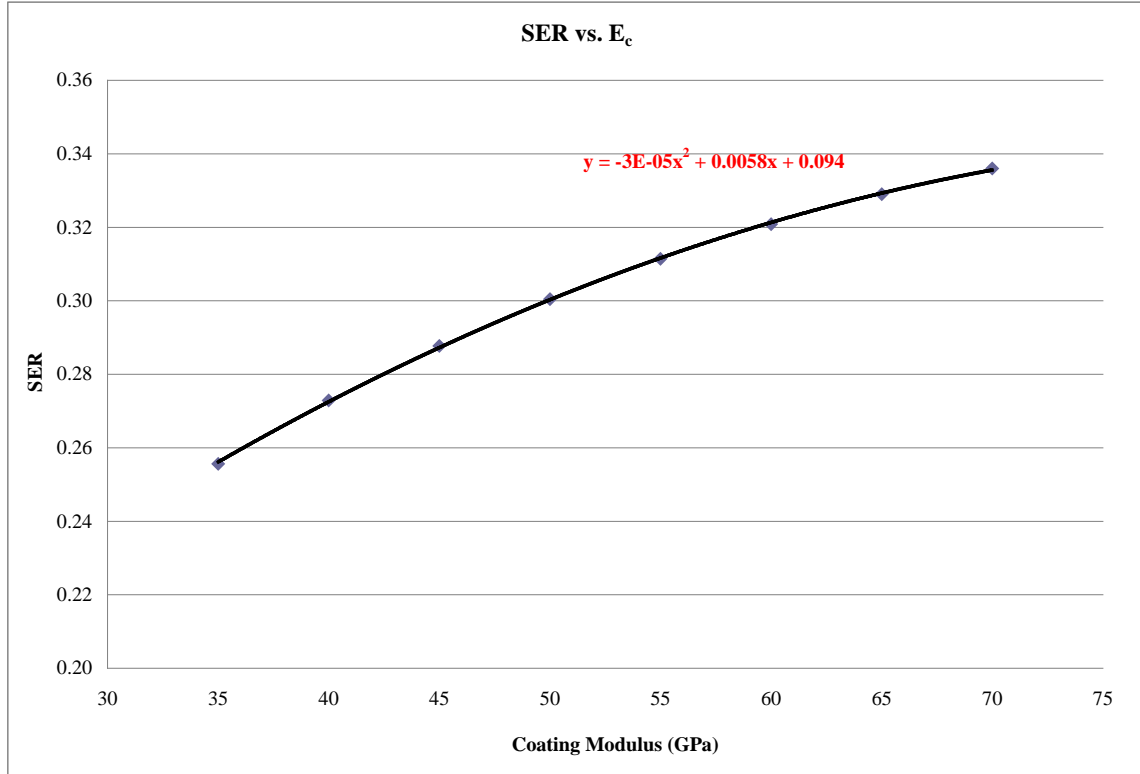
**Figure 13: Strain Energy Ratio vs Coating Modulus**

We need to examine the experimental data to proceed to the next step. Figure 14 displays the relationship between the natural frequency ($f_n$) and the measured velocity. There were two sweeps done per specimen during the experiment. There was a downsweep and an upsweep. The results are shown along with an average of the two values. We see that the sweeps resulted in very similar values for the $f_n$, diverging only

slightly at the higher velocities.  This is due in part to the magnetic coil effectiveness

reduction at higher voltages (saturation) and the damping of the coating increasing with

increasing strain.
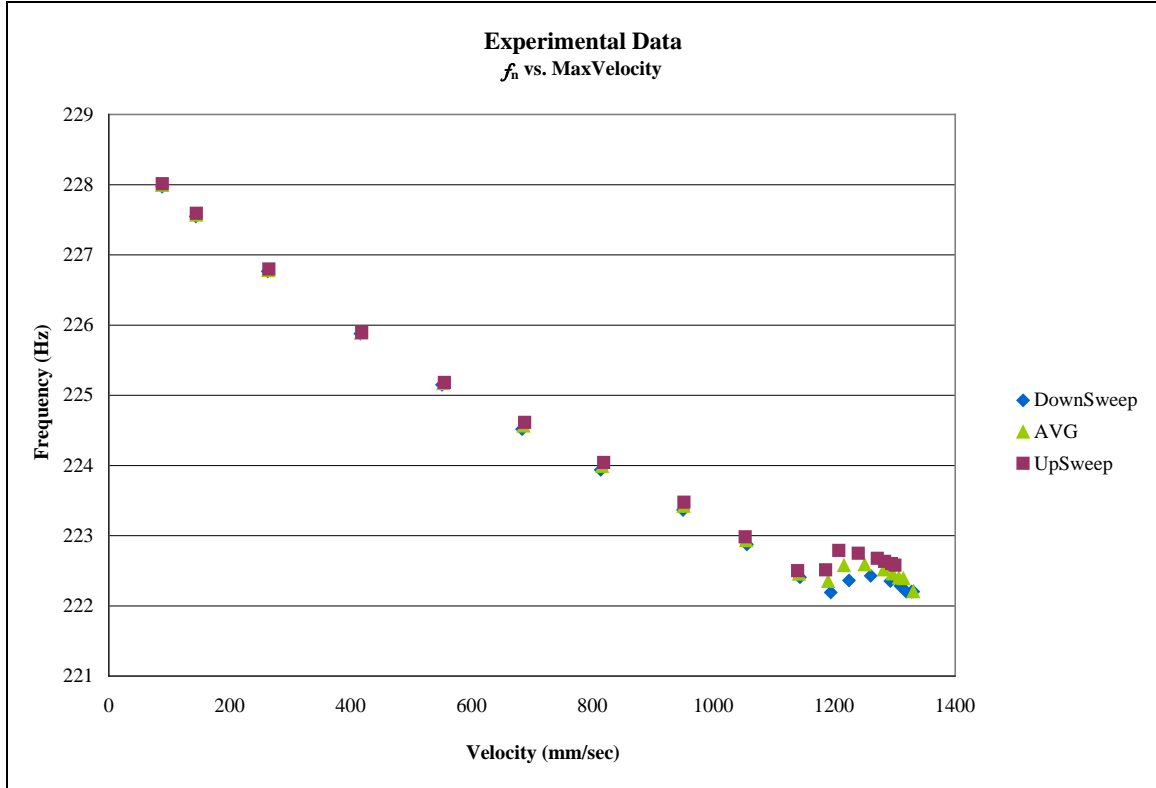


**Figure 14: Natural Frequency vs Maximum Velocity**

Using the $f_n$ obtained from the experiment and the polynomial relationship

described earlier, we can calculate the $E_c$ values for the given experimental $f_n$.  This

allows us to plot these $E_c$ values versus the measured maximum velocities corresponding

to each $f_n$.  There are 18 points on the graph which correspond to the 18 voltages tested in

the experiment. Figure 15 indicates that the coating modulus decreases with velocity, a sign of strain softening.
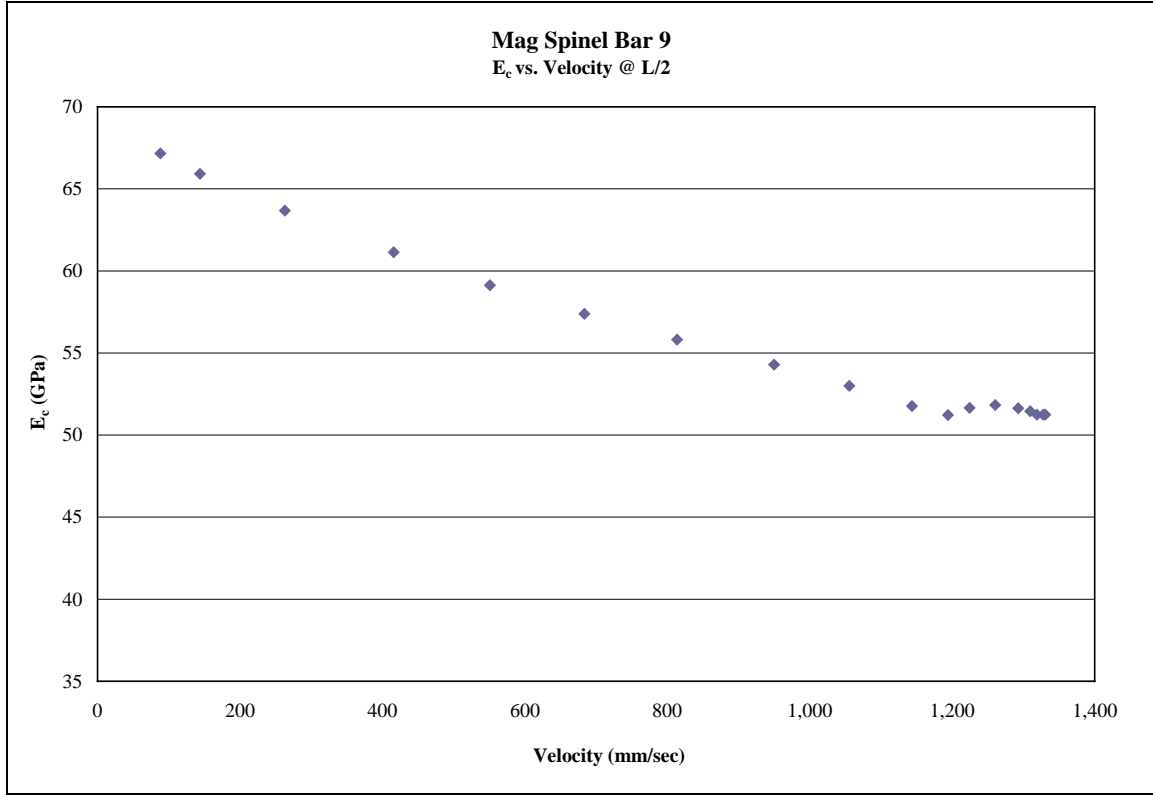


**Figure 15: Coating Modulus vs. Velocity**

By using the polynomial relating the normalized displacement (recorded at L/2) produced by the FEM eigenvector to the $E_c$ values, we can now use the corresponding $E_c$ values for each $f_n$ to establish normalized displacements versus velocity. Although the y-axis in Figure 16 displays negative values, the normalized displacements at L/2 are both negative and positive corresponding to the direction of the bending shape of the mode shape. The sign of the displacement corresponds to the direction of the deflection in the transverse direction. These values merely indicate that the FEM is deflected downward

for the first bending mode.  The experimental values likewise use sign as an indication of whether the specimen is moving toward or away from the LDV.
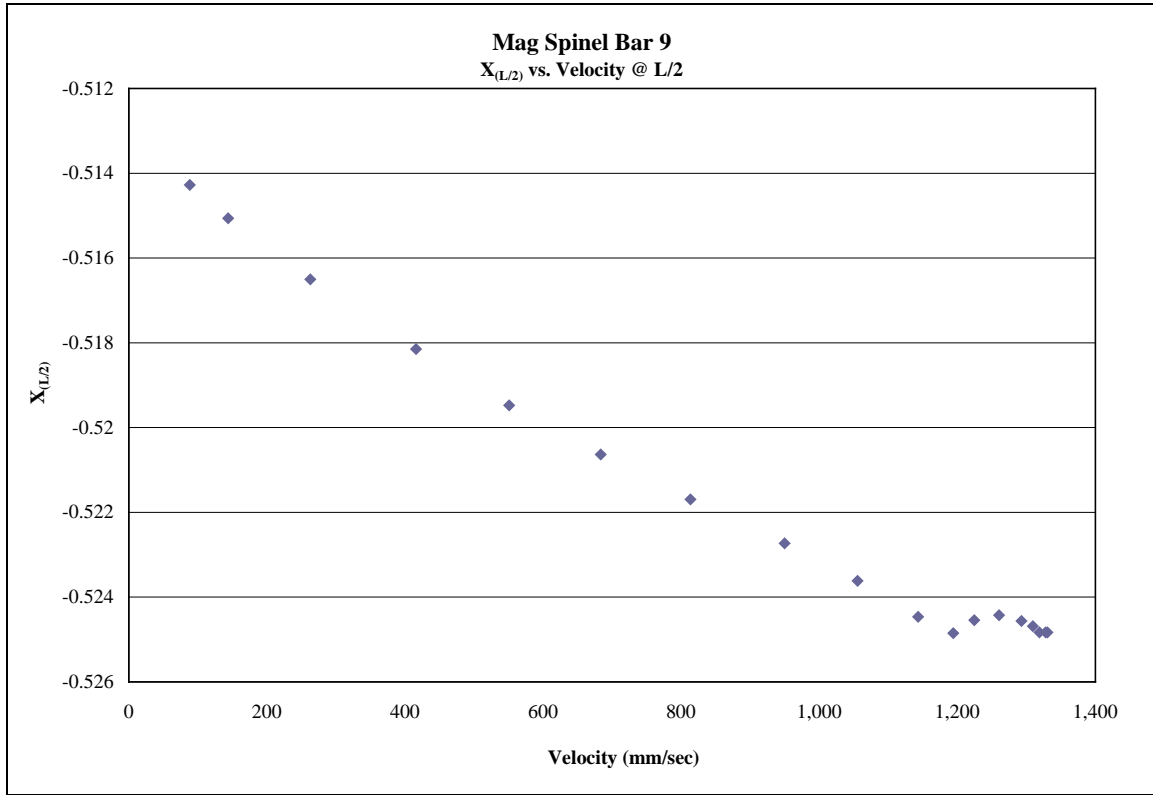


**Figure 16: X vs. Velocity**

Once again the polynomial relationship established between the $E_c$ values and a parameter obtained from the FEM will be used.  This will provide normalized strains $\varepsilon_{11}$ that correspond with the recorded maximum velocities.  Figure 17 indicates that the strain increase as the velocity is increased.  This infers that the displacement increases as the velocity increases.
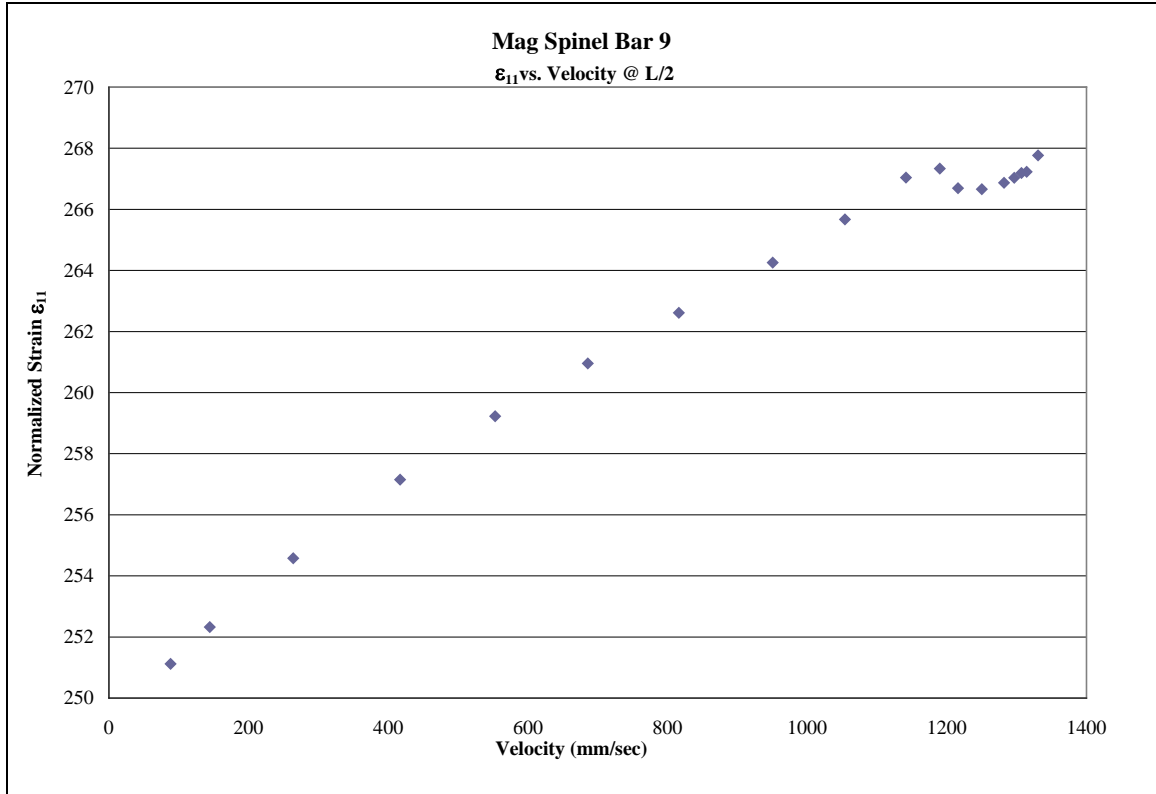
**Figure 17: Normalized Strain vs. Velocity**

Since we have now established the $E_c$ values corresponding to the experimental $f_n$'s, we can obtain the SER values by using the polynomial relationship we established above between SER and $E_c$ shown in Figure 13. This plot (Figure 18) shows the relationship between the SER values and the recorded maximum velocity. Again the 18 points represent the 18 tested voltages. We also see that at higher velocities the SER values do not change much. The trend at the higher velocities reflects the trends seen in Figure 14.
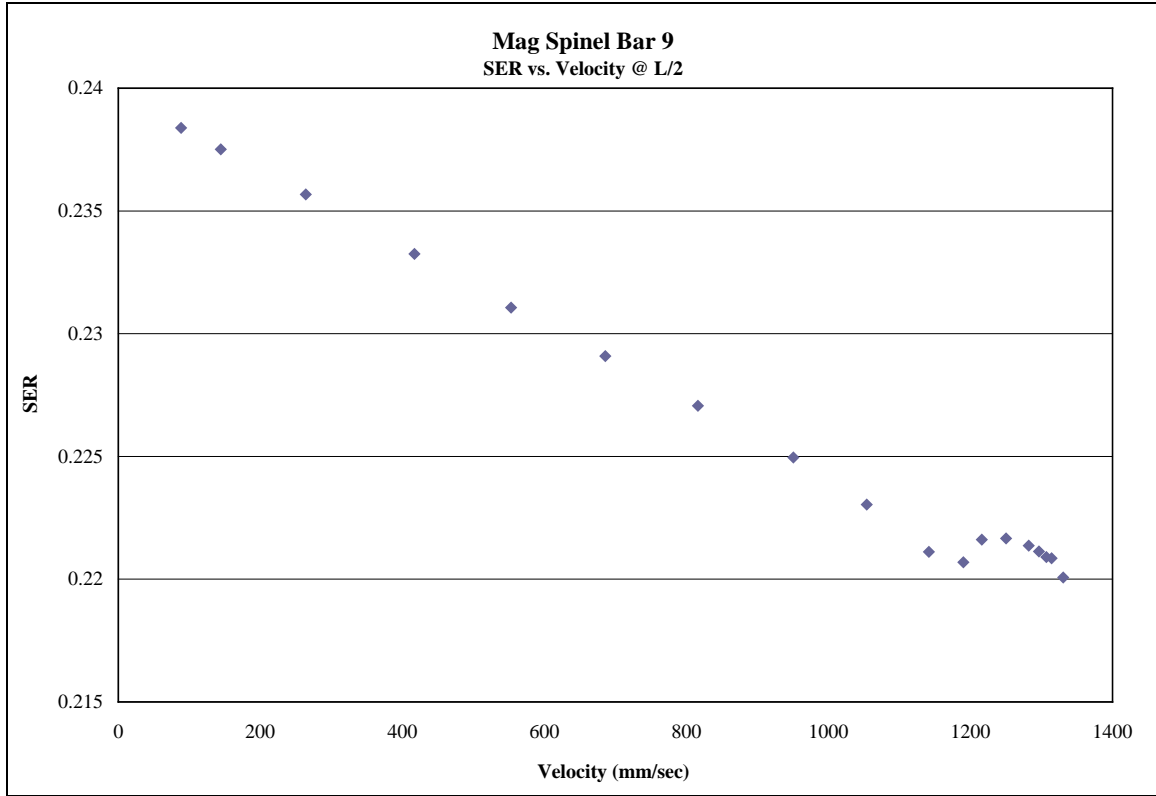
**Figure 18: Strain Energy Ratio vs. Velocity**

Previously, the simplifying assumption that the specimen can be treated as a lumped mass has resulted in Equation 2. In this equation displacement is designated as 's'.

$$s = A\sin(\omega t)$$
$$\frac{\partial s}{\partial t} = V = \omega A\cos(\omega t) \qquad \textbf{(2)}$$

Let us now calculate the displacements that correspond to the experimentally measured maximum velocities by using the following relationship:

$$\delta = \frac{V}{\omega}$$

$$\omega = f_n * 2 * \pi$$

**(3)**

Figure 19 shows the calculated displacement increasing with an increase in voltage. It appears to show evidence of magnet coil saturation at the higher voltages. As more voltage is input into the magnetic coil, the specimen does not increase its response very much. This also indicates increased damping by the coating, dissipating more energy at the higher strains.
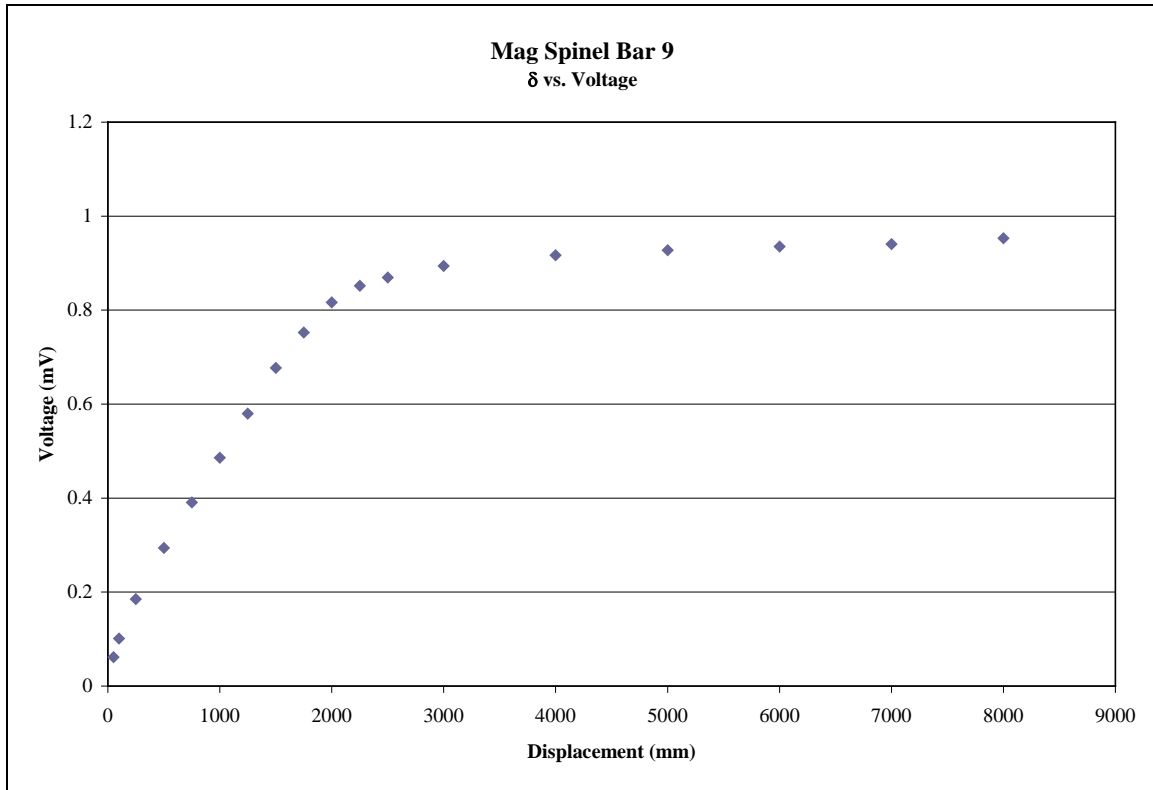


**Figure 19: Displacement vs. Voltage**

The LDV measured the velocities at the center of the specimen in mm/sec. Since Hz are measured in cycles/sec, the $f_n$'s must be multiplied by $2\pi$ to define the cycles as

physical motion. This means that the bar moves from its furthest position away from the LDV to its closest position in a cycle that is equivalent to π. The LDV measures the velocity that the center of the specimen is moving as it goes through these cycles. By dividing this measured velocity by the frequency we obtain the displacement. The only measured data we have is the velocity at $\left(\dfrac{L}{2}\right)$. By converting it into displacement at the natural frequency and the corresponding maximum velocity, we can compare it to the normalized displacement produced by the FEM at the same location on the model $\left(\dfrac{L}{2}\right)$ to obtain the scaling factor $\lambda$. The scaling factor is calculated using Equation 4.

$$\lambda = \frac{\delta}{X\left(\frac{L}{2}\right)} \tag{4}$$

The scaling factor is plotted against velocity in Figure 20. This relationship, between the measured displacements and the normalized displacements produced by the FEM, scales the obtained mode shape values to the experimental data. The reason for this is to obtain values that are required to calculate the material properties of the coating. The strains in particular are required to obtain context for the material properties. These properties can then be systematically compared against other coatings using the same scale.
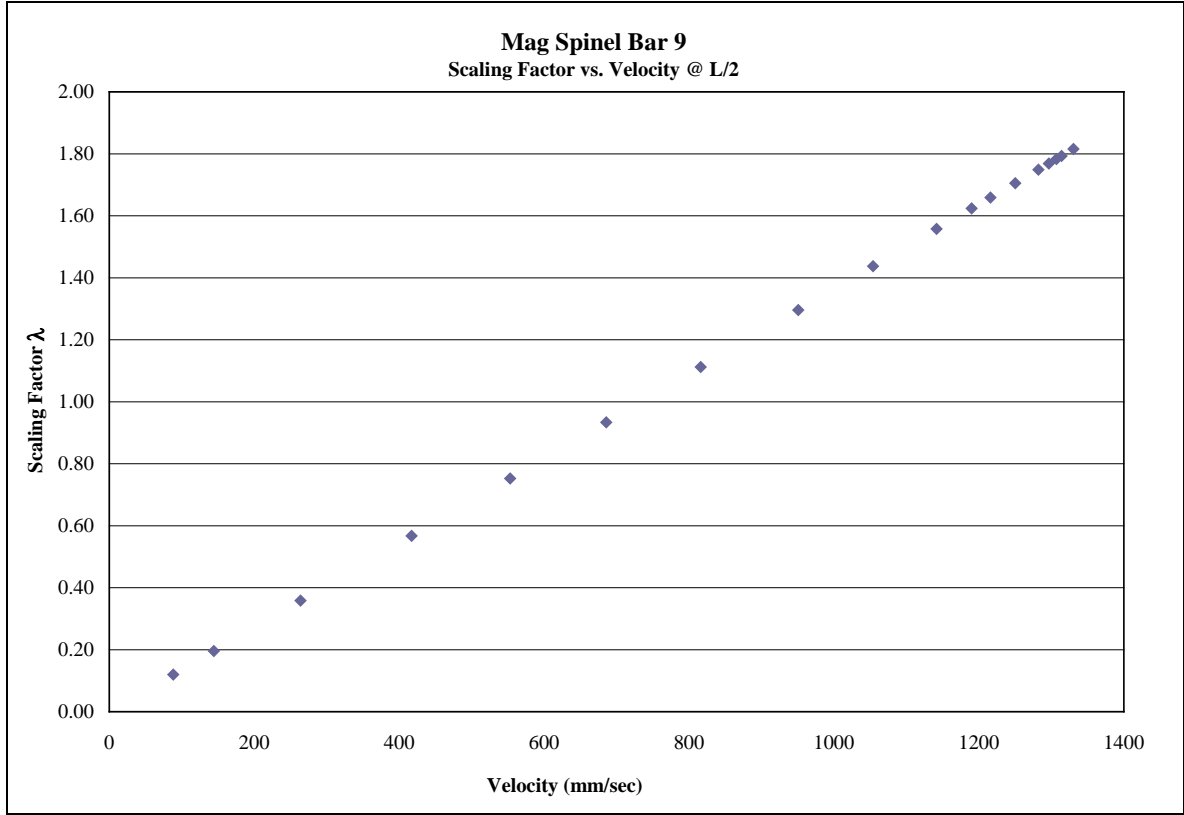
**Figure 20: λ vs. Velocity**

The actual strain experienced in the tested specimen can now be calculated by using the

scaling factor obtained from the displacement relationships and applying it to the

normalized strains obtained from the FEM mode shape using Equation 5. This strain is

plotted against recorded maximum velocities in Figure 21. It shows a linear relationship

between strain and velocity.

$$\varepsilon = \lambda \tilde{\varepsilon} \qquad \qquad (5)$$

34

**Mag Spinel Bar 9**
$\varepsilon_{11}$ vs. Velocity @ L/2
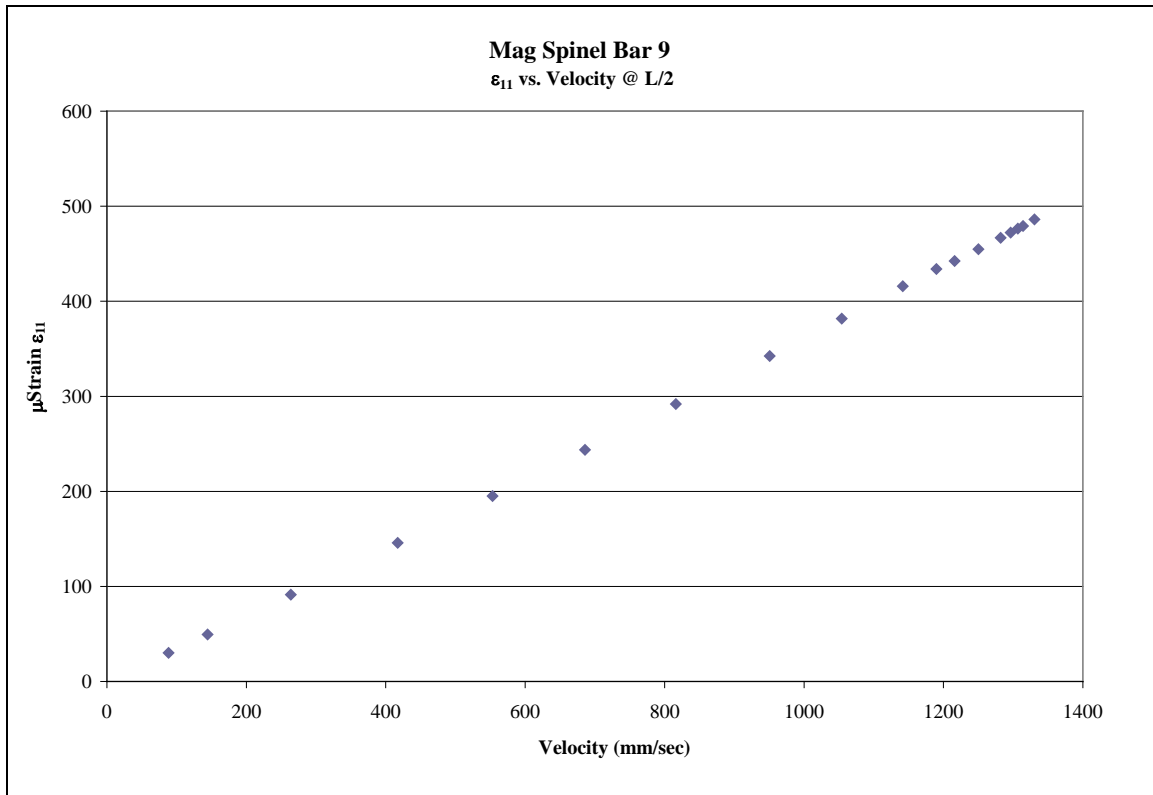
**Figure 21: Actual Strain vs. Velocity**

The material properties can now be plotted.  We can see in Figure 22 that the coating modulus is non-linear with respect to strain.  Figure 6 showed strain softening and now we can quantify that result using this plot, keeping in mind that this is one specimen.
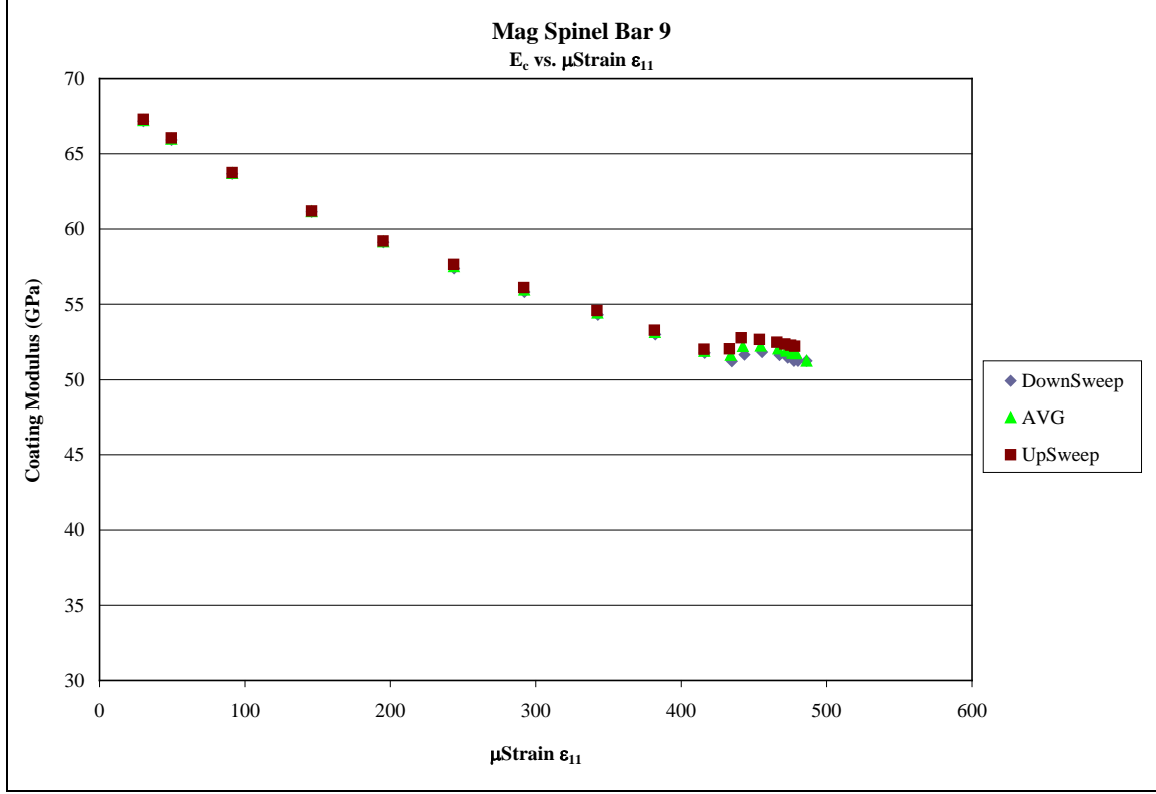
**Figure 22: Coating Modulus vs. μStrain**

The loss factor for the coating $\eta_{coat}$ is calculated using Equation 6. The full development of which can be found in Reed (2007). The SER values that were obtained for each natural frequency, as shown in Figure 18, will be used in this equation and the $\eta_{bare}$ can be approximated from the bare beam experiment data as $\eta_{bare} \approx 0.0004$.

$$\eta_{coat} = \frac{\eta_{sys}(SER+1) - \eta_{bare}}{SER} \tag{6}$$

The loss factor of the bare beam was approximated by using the half-power bandwidth technique that is based on a linear assumption. As stated previously, the beam itself must behave linearly if the non-linear coated properties are to be estimated accurately. Several bare beam specimens were tested at various voltages in atmosphere as well as in vacuum.

The low damping properties of the titanium resulted in only lower voltages being tested. The range of voltages was from 10mV – 500mV as opposed to the coated beams which were tested from 50mV – 8000mV. The lower damped beams had larger displacements per voltage as would be expected. At higher voltages, the natural frequency of the beams began to diverge from the lower voltage cases. Figure 23 is from Pearson's work.
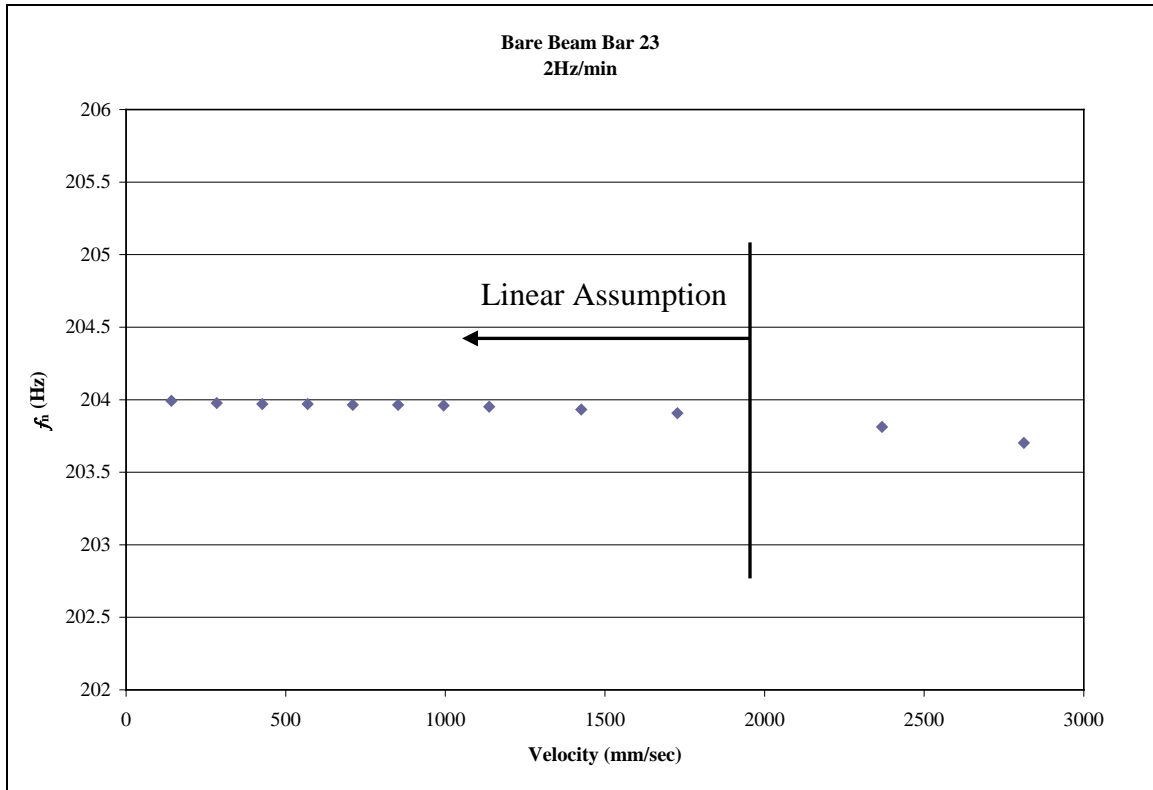


**Figure 23: Bare Beam Experimental Results**

The loss factor of the entire system $\eta_{sys}$ must still be calculated. This is done by using the half-bandwidth method (discussed in further detail in Chapter III) which assumes damping is of the viscous type and linear (Reed 2007). The $\eta_{sys}$ for each experimental sweep must be approximated with this method and was done for this work by analyzing

the data with a Matlab script. Once $\eta_{sys}$ for each sweep is obtained the $\eta_{coat}$ can be calculated using Equation 6 above.
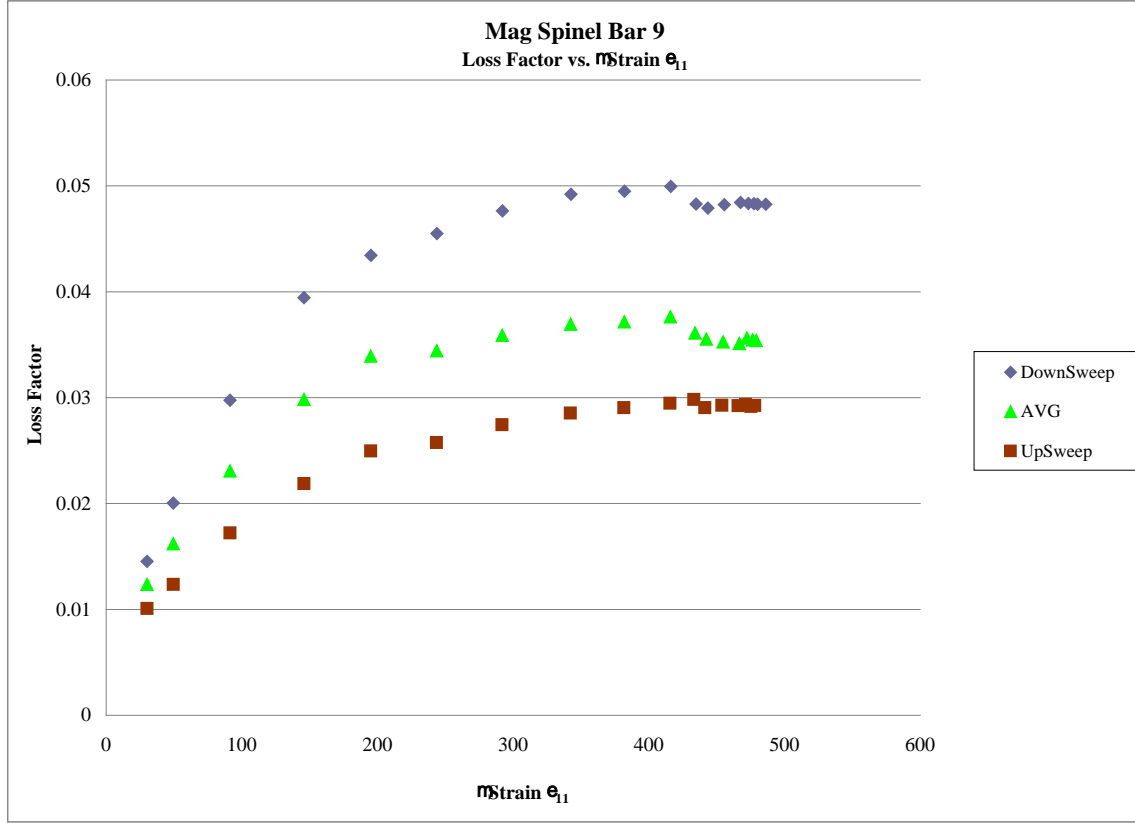


**Figure 24: Loss Factor vs. μStrain**

Once we have $\eta_{coat}$ for each voltage that was tested, we can plot the values versus the actual strain as shown in Figure 24. Thus far, the experimental results i.e. $f_n$ and maximum velocities were averaged but now not only are the maximum values used but the entire FRF is required for the half-power bandwidth method. Figure 24 shows that the upsweep and downsweep result in different values for $\eta_{coat}$. This is because the half-power bandwidth method was developed for linear modeling, while the coating is clearly non-linear in nature. This issue is explored further in Chapter III.
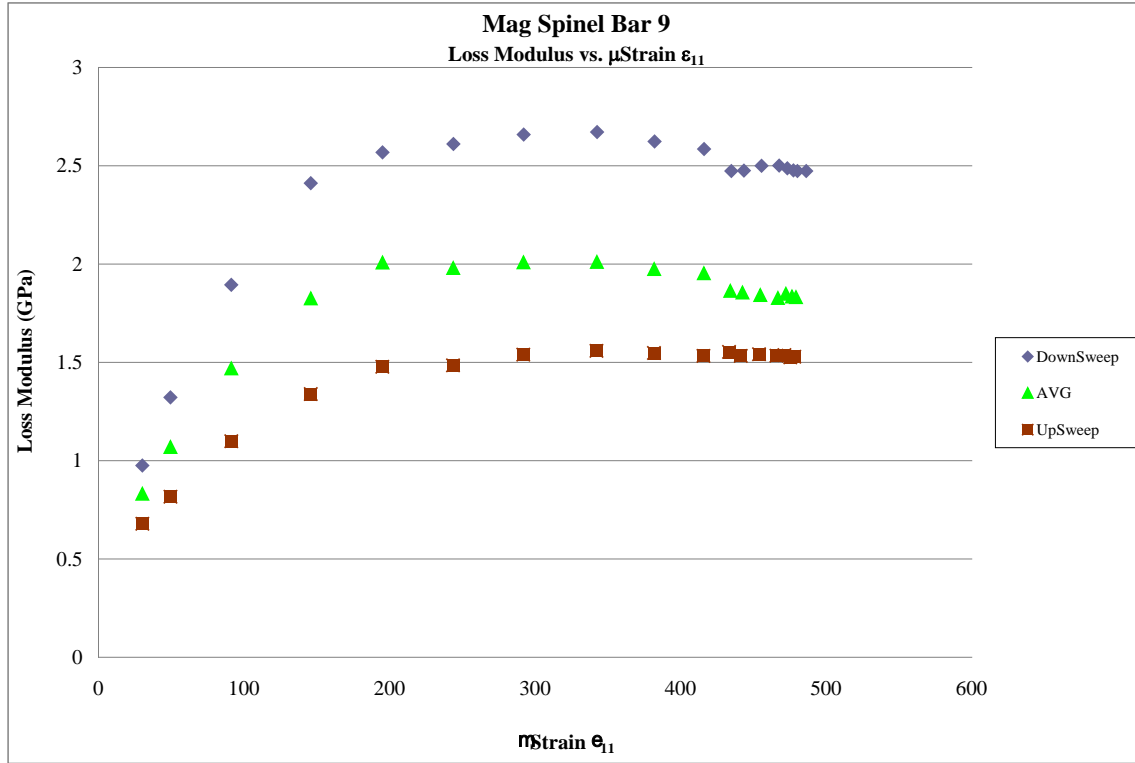
**Figure 25: Loss Modulus vs. μStrain**

The Loss Modulus is a damping term that describes the dissipation of energy into heat as a material is deformed. It is a more relevant measure since the response of a thinly coated structure is driven by its value (Torvik 2008). In Figure 25 it shows the same variability as the Loss Factor due to the sweep direction. This is due to its dependence on the Loss Factor as shown in Equation 7.

$$\text{Loss Modulus} = \eta_{coat} * E_c \tag{7}$$

# III.  Experimental Details

## *Objective*

In the previous chapter, the procedure developed by Reed (2007) and followed by Pearson (2008) was outlined.  In this Chapter the results will be presented and compared to Pearson's results.  The reason for this is that the experimental data used in the procedure was collected by Pearson.  This will allow a direct comparison of the FEM used in Pearson's research and the FEM developed during this research since the experimental data was the same in both cases.  The differences between the two will be investigated.  These differences show the effect that the FEM portion of the procedure has on the estimation of the material properties.  In addition, the half-power bandwidth is based on a symmetric bandwidth which is not the case here.  Various methods are discussed which attempt to compensate for this fact.  Finally, the sweep rate utilized by Pearson during his data collection (2008) is examined with regard to the bare beam with the purpose of validating the loss factor approximation made by Pearson in his research (2008).

## *Comparison*

As stated the experimental data used for this study was collected during Pearson's research.  The material properties obtained by both analyses can be plotted and compared.  Figure 26 compares the results for the coating modulus for mag spinel bar 9.  It is clear that there is a difference in the strains reported.  However, the larger difference is in the coating modulus estimations.  This is a result of a stiffer FEM.  As previously stated the beam's modulus that was used previously (Pearson 2008) was chosen so that the FEM would match the natural frequency seen in experiment.  This resulted in a modulus that was lower then what is usually reported for Ti-6Al-4V.  This was an attempt to account for model simplifications to include the absence of the monofilament wire supports as well as simplifying the model of the magnets.  In this research the published values for the bare beam were used.  However, this does not account for the total difference as shown in Table 3.  The lower modulus value used for the bare beam actually softens the FEM.  As the beam modulus is lowered we would expect to see the estimated coating modulus numbers increase.  This is due to the fact that the experiment recorded certain natural frequencies and as the FEM of the beam is softened, the coating model will show higher coating modulus numbers to compensate.
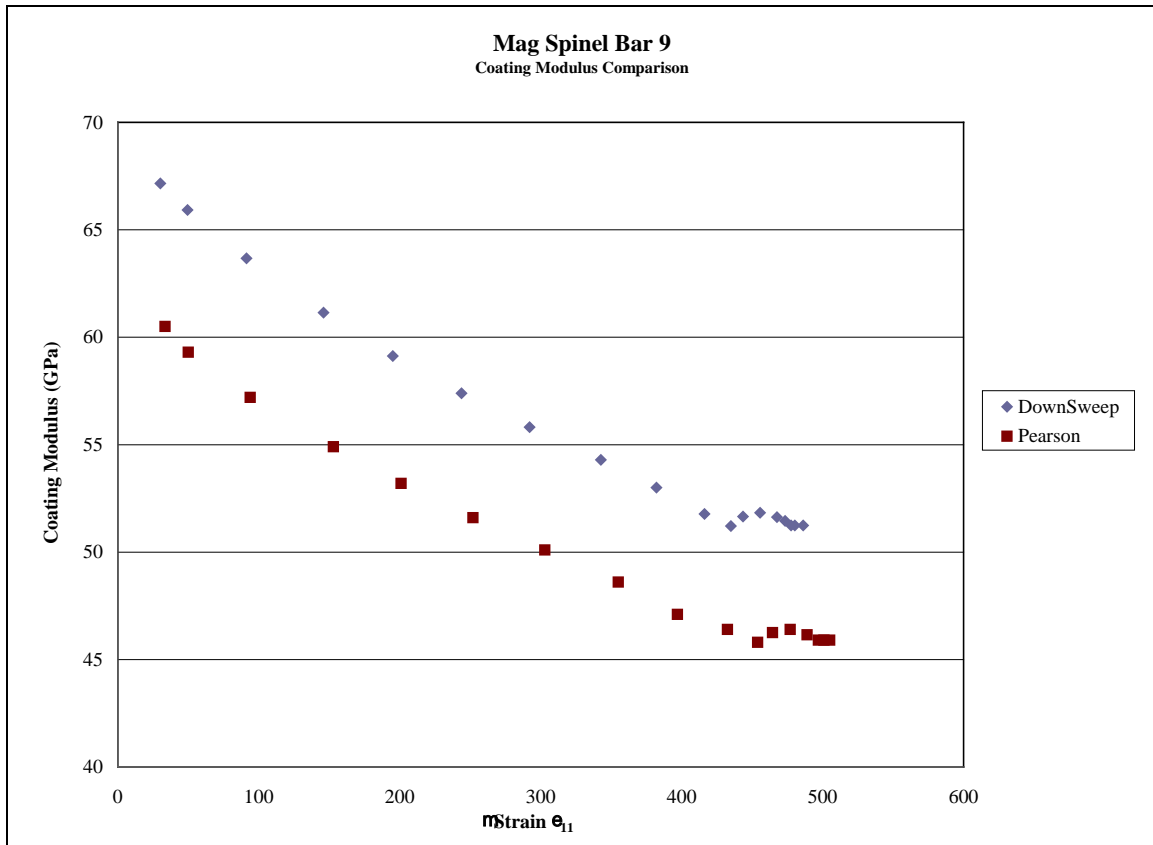
**Figure 26: Coating Modulus Comparison**

Figure 27 shows a similar difference in reported strains as the previous Figure. In this case the highest values reported by Pearson are above the results of using the downsweep data in this research. The differences are a direct result of the stiffer FEM used.

42
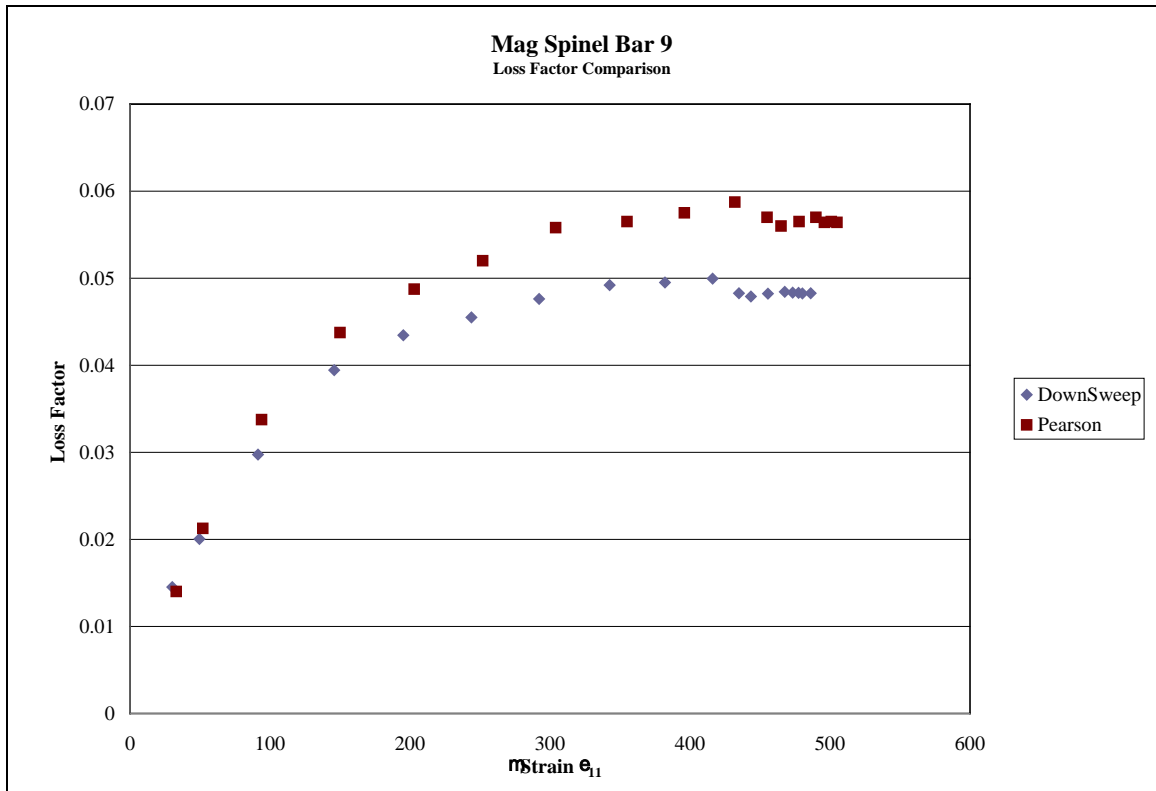
**Figure 27: Loss Factor Comparison**

Figure 28 again shows differences between the two analyses. Since the exact same experimental data was used for both analyses, the differences must lie in the output produced by the FEM. The differences are on the order of 10% with regard to reported strains. There are several possibilities to account for these differences as shown in Table 3.
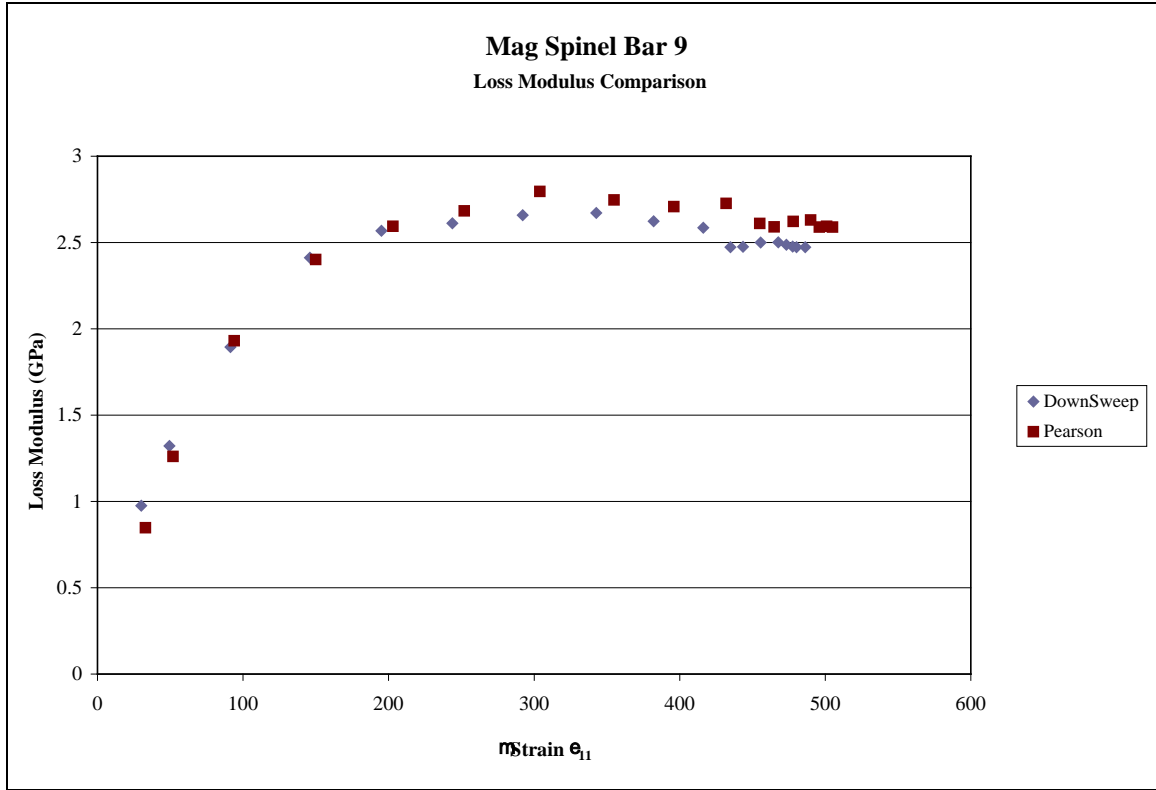
**Figure 28: Loss Modulus Comparison**

There were several differences between the FEM used by Pearson and the one used in this study. The element chosen, mesh density, Ti-6Al-4V material properties, and software package were all different. Each of these parameters adds uncertainty to the results and it is believed that all contribute to the overall differences. Table 3 shows the contribution of each parameter to the overall difference. The ANSYS element used (Solid 45) was assumed to be similar to the ABAQUS element C3D8. This is a first order 8 noded element that does exhibit some parasitic shear in bending. ABAQUS was used for the results shown in Table 3. All other parameters were held constant, in the FEM, as the parameters listed were varied as shown. The results were than compared to each other.

**Table 3: Parameter Comparison**

| Parameter | ANSYS | ABAQUS | Strain % Difference | Frequency % Difference |
|---|---|---|---|---|
| Element Type | Solid 45 (estimated w/C3D8) | C3D8I | 2.4% | 6.7% |
| Mesh Density (mm) @ Interface | 1.27X1.27X0.8 | 0.5X0.5X0.8 | 0.15% | 0.77% |
| $E_{beam}$ | 110.4 GPa | 113.8 GPa | -1.25% | -0.5% |
| Density$_{beam}$ (g/mm$^3$) | 4.39 | 4.43 | -0.5% | -0.6% |
| Software Pkg | Solid 45 | C3D8 | ? | ? |
| Maximum Difference | | | ~0.8% | ~6.4% |

## *Half-Power Bandwidth Method*

The loss factor of the bare beam was approximated by using the half-power bandwidth technique that is based on a linear assumption.  Figure 29 (Walker 2007) correlates the shape of an FRF to the materials behavior.  Clearly there are non-linear softening effects evidenced in Figure 30 (Pearson 2008).  Equation 8 below is used to determine the loss factor $\eta_{sys}$ from the FRF in the following manner.

$$\eta_{sys} = \frac{f_2 - f_1}{f_n} \qquad \textbf{(8)}$$

First, find the natural frequency marked $f_n$ in the equation.  Divide the maximum velocity associated with the natural frequency by the square root of two.  This provides a 3 dB drop in velocity.  This resulting velocity corresponds to two frequencies on the FRF as shown in Figure 31.  The loss factor is related to the damping ratio and the quality factor by Equation 9 below.

$$\eta_{sys} = 2\zeta = \frac{1}{Q} \tag{9}$$

One of the methods used by this investigation in an attempt to better approximate the material properties of the coating was to compensate for error associated with the estimation of the loss factor of the system ($\eta_{sys}$). Figure 32 from Pearson's work illustrates the fact that for a non-linear material there are instabilities in a downsweep at the lower frequencies.
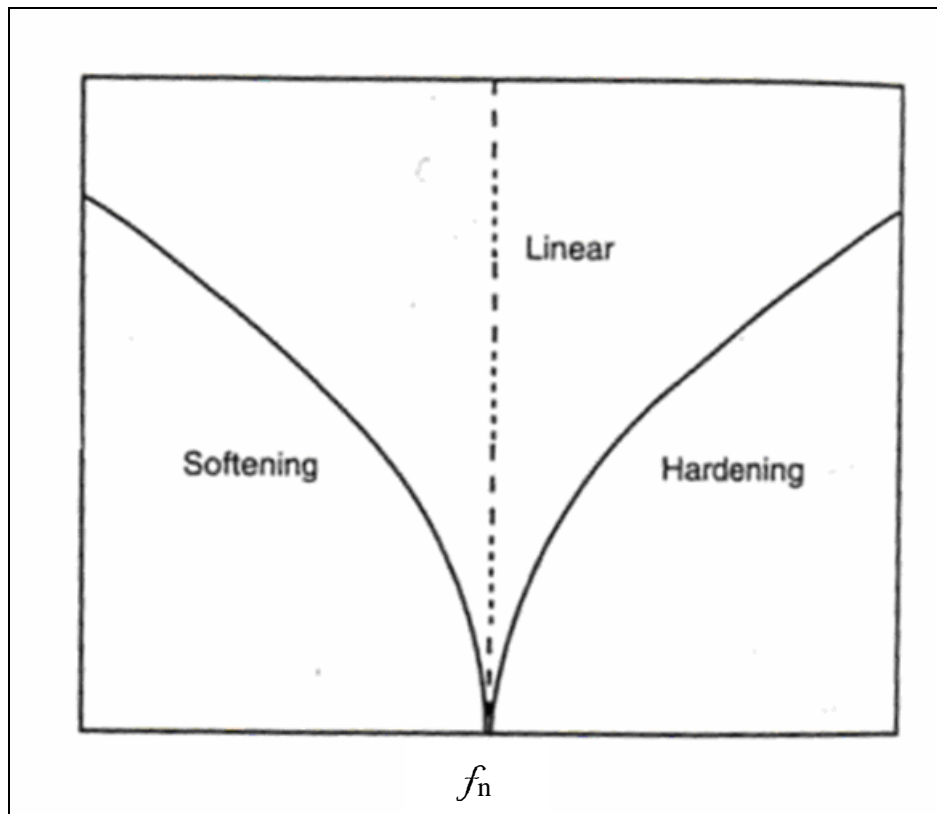


**Figure 29: Backbone Curve Linear & Non-Linear**
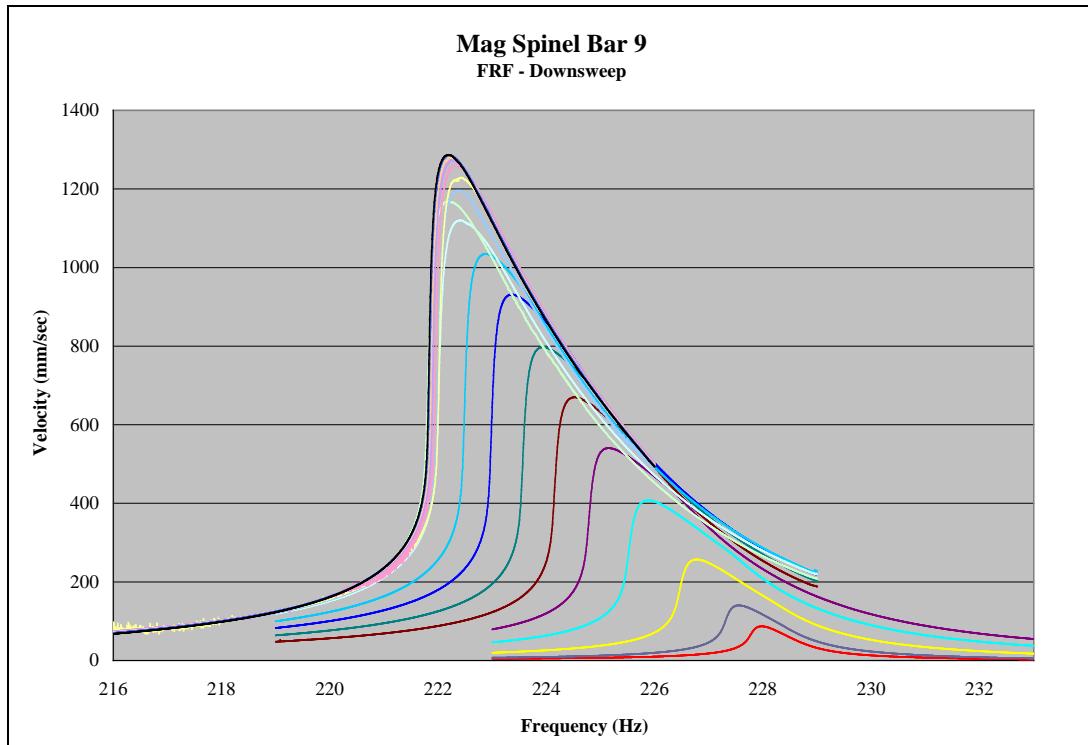
**Figure 30: Non-Linear FRF**
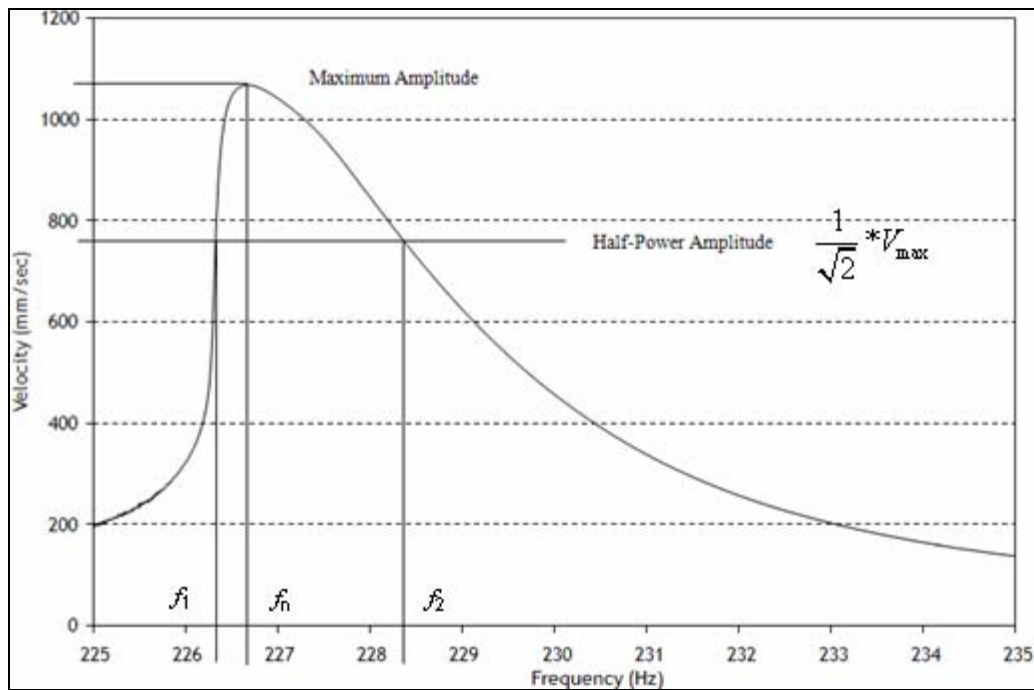


**Figure 31: Half-Power Bandwidth Calculation**

47
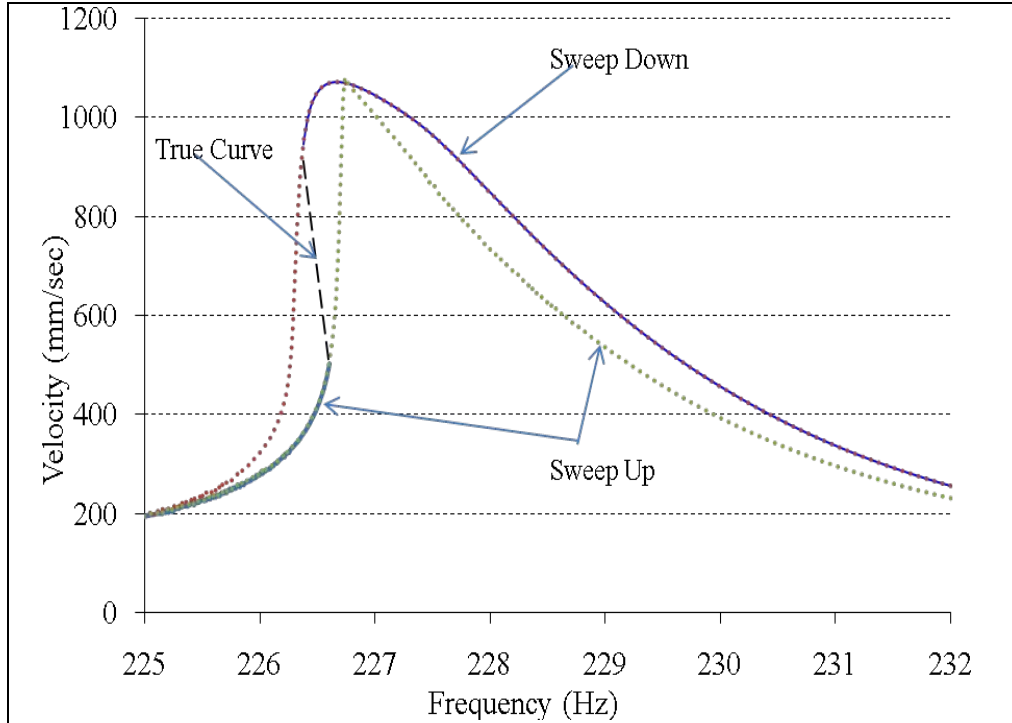
**Figure 32: Half-Power Bandwidth Considerations**

In an attempt to compensate for this, an upsweep was done (Pearson 2008). The downsweep and upsweep FRF's are shown in Figure 33. These two sets of data collected by Pearson (2008) are the basis for the analysis performed in this section. All of the calculations done using the half-power bandwidth were done by the author. In addition, the FEM created in this research was used in estimating the material properties of mag spinel shown in this section.
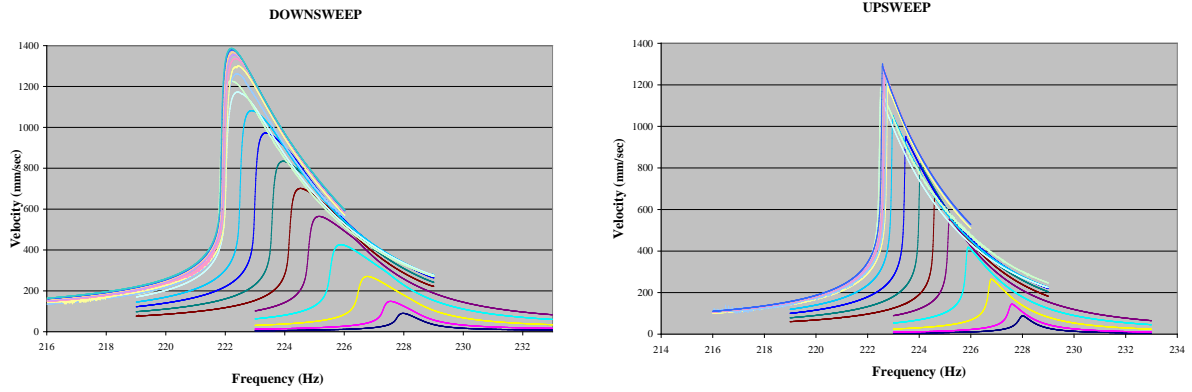
**Figure 33: DownSweep vs. UpSweep**

The first compensation attempt was to take an average of the velocities at each corresponding data point. This is shown in Figure 34. The result of this is an $\eta_{coat}$ that is roughly in between the values of the downsweep and the upsweep as expected. Unfortunately, we see that the average of the velocities results in a jump in values at approximately the same point needed for the half-power bandwidth calculation. A different approach was tried for a smoother line on the lower frequency side of the downsweep, because it is seen in Figure 34 that the average resulted in a line that is not quite what is depicted in Figure 32.
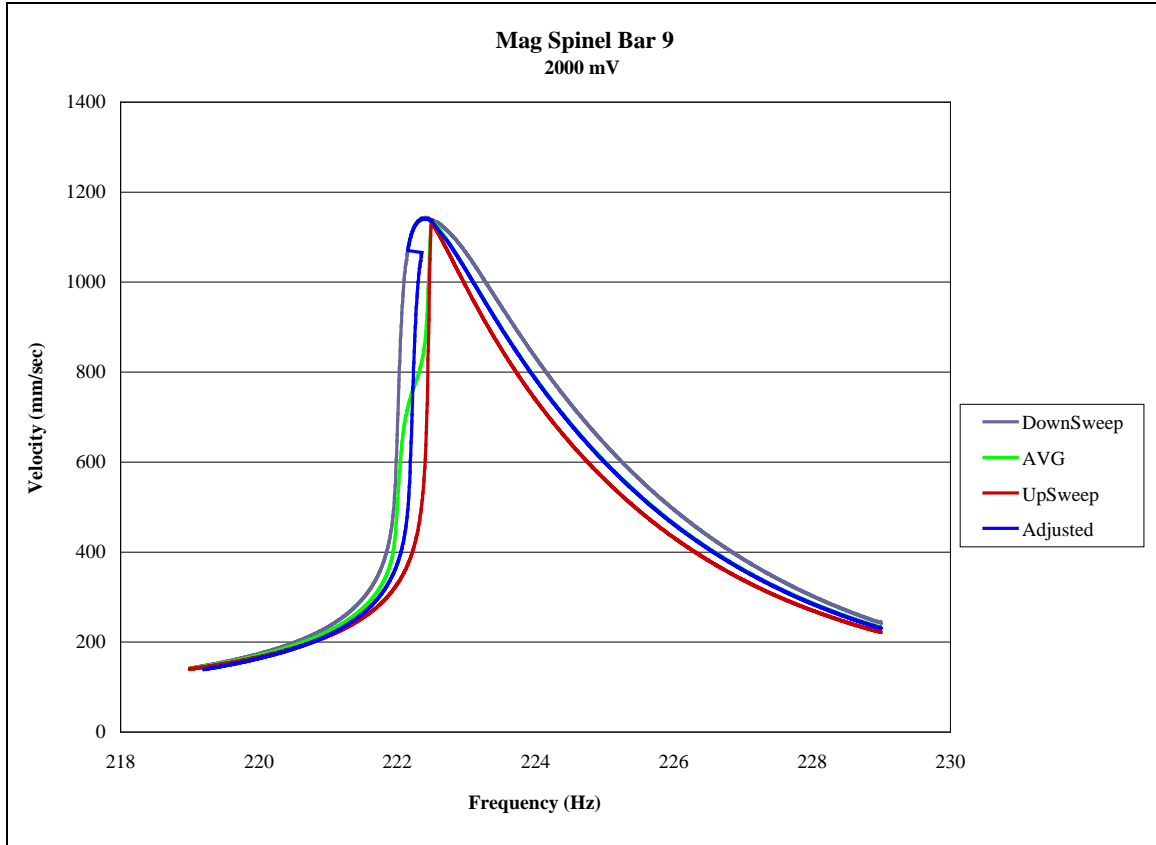
**Figure 34: Averaged and Adjustment Technique**

The downsweep line is shifted as an adjustment. The downsweep curve on the lower

frequency side was shifted to the average distance between the upsweep and downsweep.

The results are values only slightly different from the average obtained earlier as seen in

Figure 35. This is due to the fact that for the half-power bandwidth only three values are

used from the FRF while the average and adjustment result in different graphs the

bandwidth itself is only slightly changed. Indeed, in these two cases the natural

frequency $f_n$ remains approximately the same.
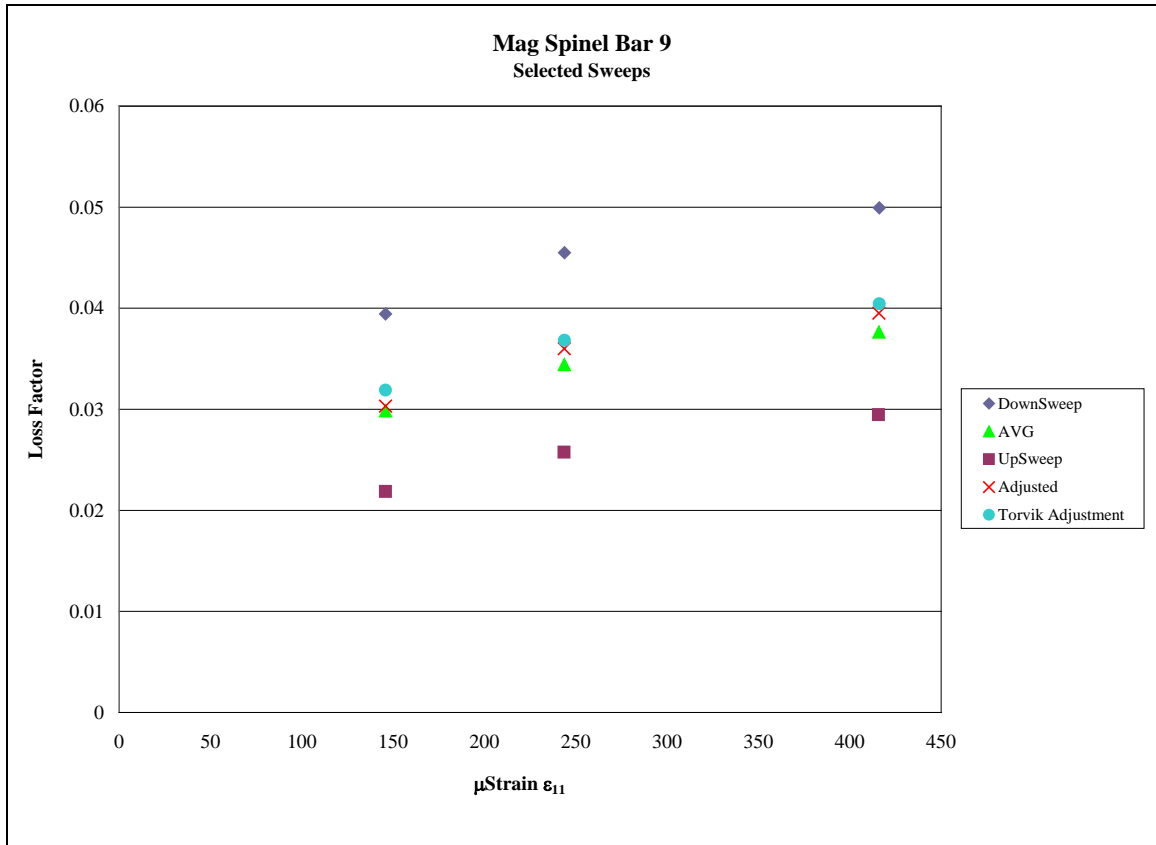
**Figure 35: Select Strain Results**

The next compensation attempt was to adjust the value of $f_n$ to reflect the fact that the

FRF of interest is not symmetric about $f_n$. A least squares fit with a 2nd order polynomial

was made to the natural frequencies of the 18 FRF's for Mag Spinel bar 9. This is shown

in Figure 36.
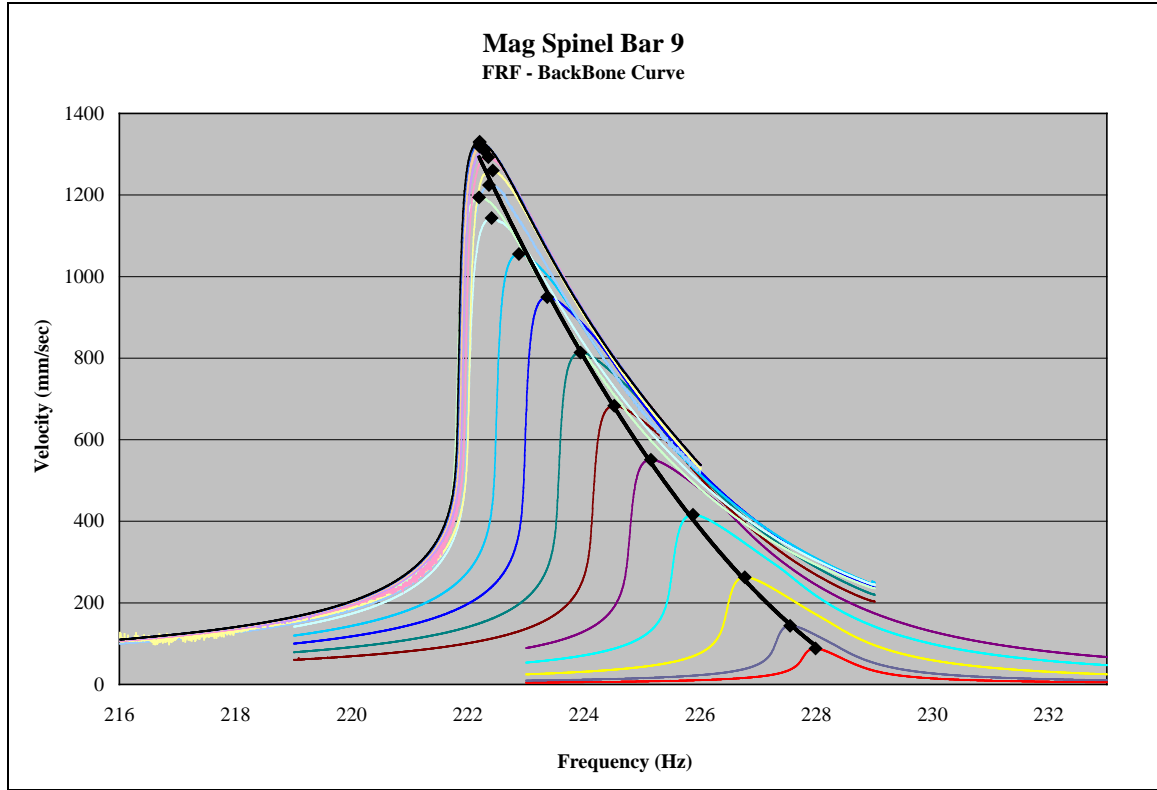
**Figure 36: BackBone Curve**

This polynomial is used to calculate a new $f_n$ that corresponds to the 3dB drop in voltage

as shown in Figure 31. The $\eta_{sys}$ that is determined with this technique is used to calculate

$\eta_{coat}$. This method does not use data from the upsweep. The results are compared in

Figure 39. As only the downsweep FRF's are used the results show a limited difference

in $\eta_{coat}$. The bandwidth does not change and the change in $f_n$ does not affect the results

by much.
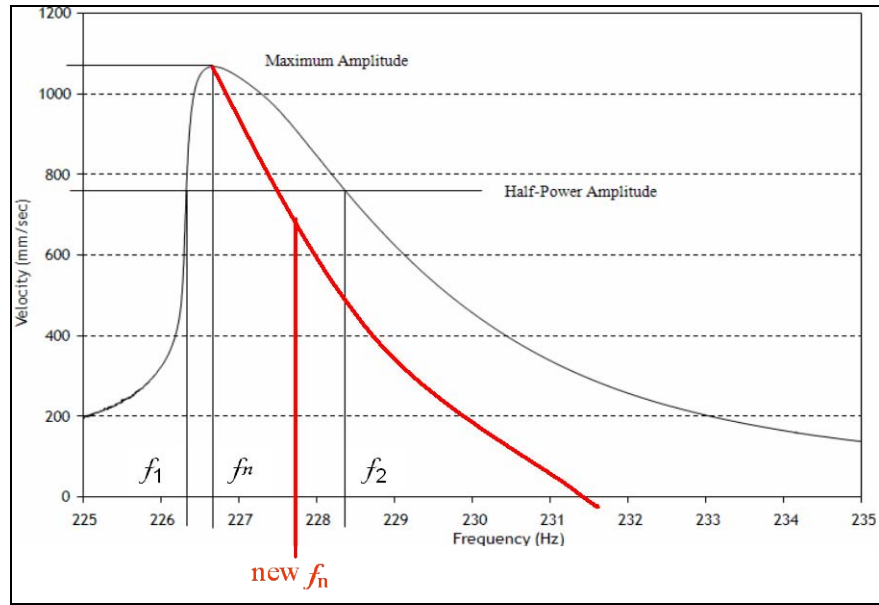
**Figure 37: Half-Power Bandwidth Polynomial**
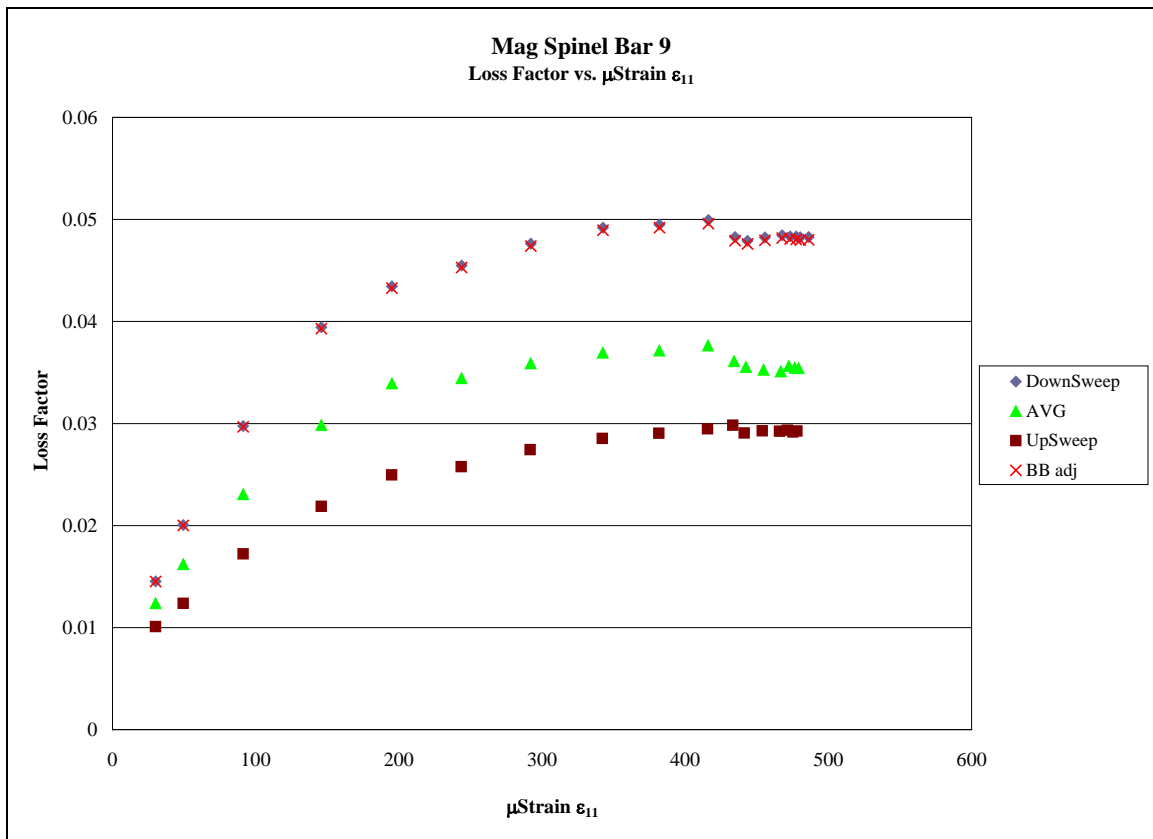


**Figure 38: Polynomial Adjustment Results**

The final compensation was based on work down by Torvik (2009). His work indicated that the $\eta_{sys}$ calculated from the downsweep could be multiplied by 0.8625. This parameter is based upon the assumption that the loss factor is a simple form of maximum strain at resonance and that the damping is relatively light.
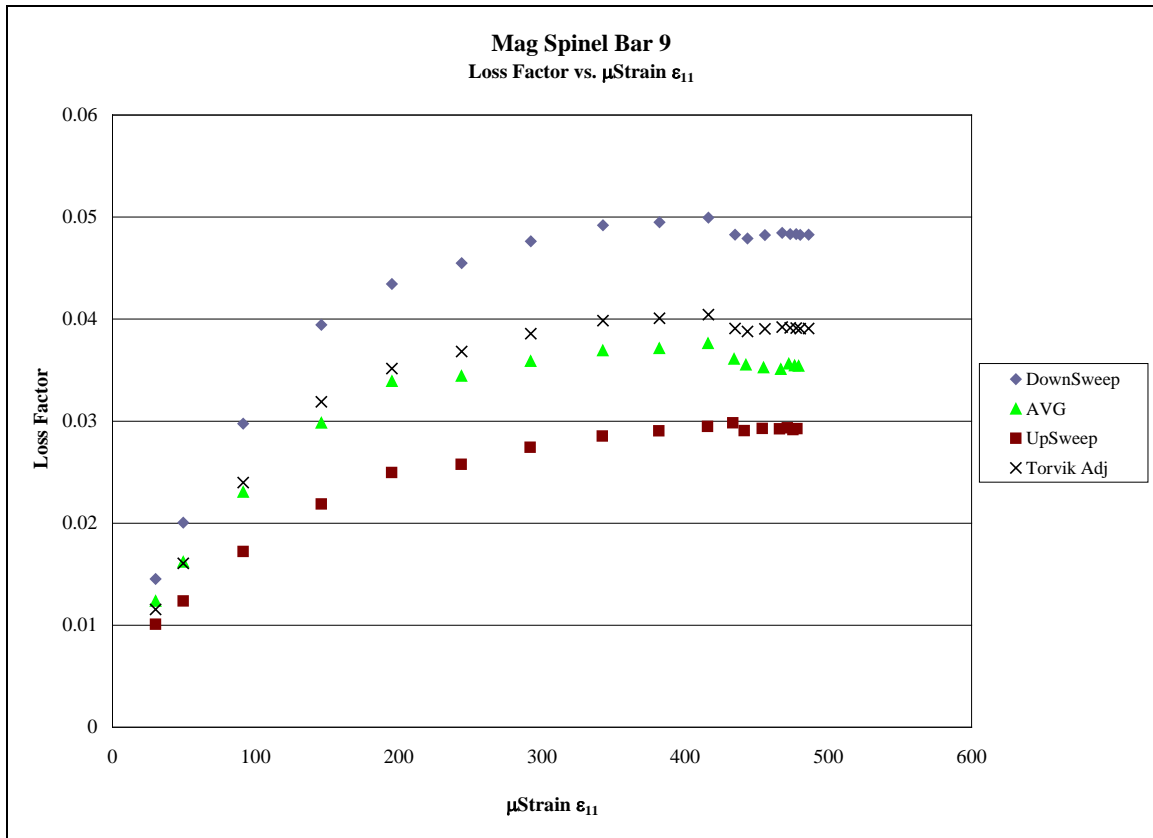


**Figure 39: Torvik Adjustment Results**
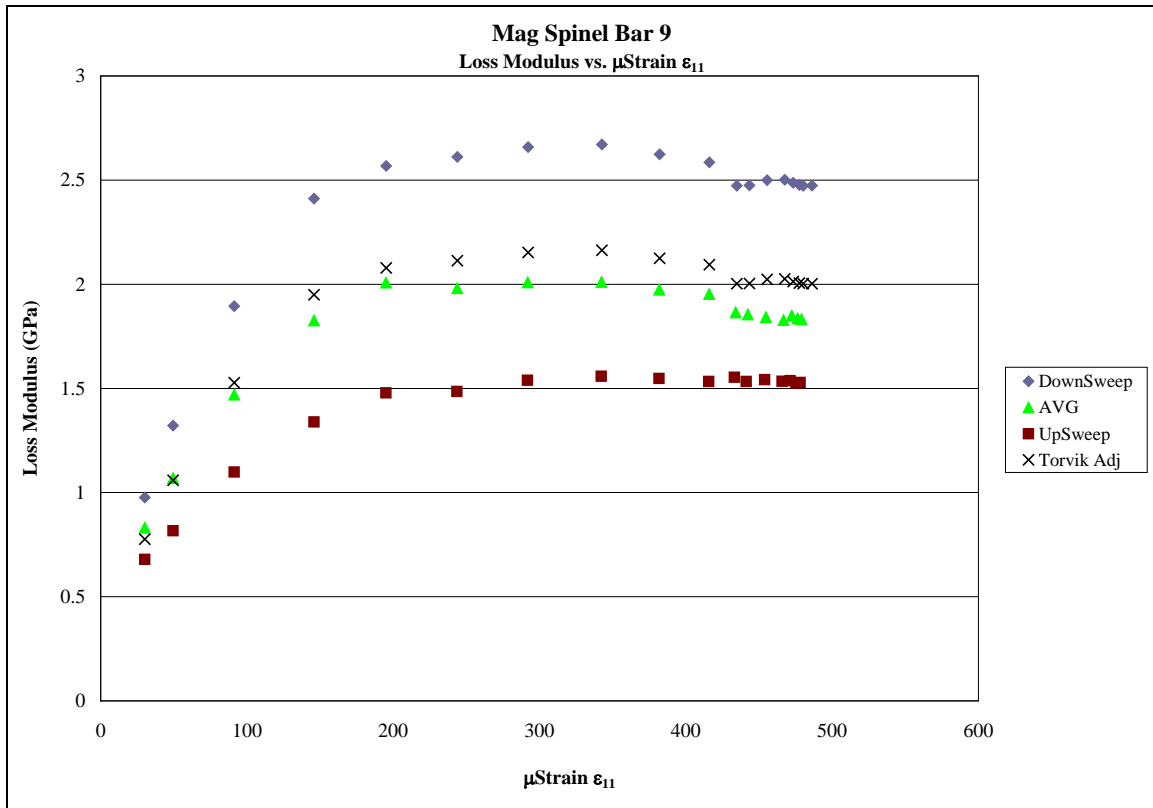
**Figure 40: Loss Modulus Comparison**

The results of this are shown in Figure 39 and Figure 40.  Coating modulus was shown in

Figure 22 to not be affected by the half-power bandwidth and so is not compared here.

## Sweep Rate

The sweep rate was investigated in this study as a possible cause of the bare beam loss factor reported in Pearson's work. A loss factor $\eta_{bare}$ of 0.0008 was reported from applying the half-power bandwidth method to FRF's collected during Pearson's experiment. Pearson tested several Ti-6AL-4V bars in vacuum and in atmosphere. This data set was analyzed in this research. Pearson did not examine the differences between the different titanium beams and the effects of the different sweep rates. Figure 41 plots the results of the downsweeps. The loss factor was calculated with the half-power bandwidth as shown in Equation 8. This figure includes data collected at atmospheric conditions as well as data collected in a vacuum. The atmospheric data show that as expected the damping increases with an increase in displacement. This displacement is directly related to velocity by Equation 3 as described previously. The effect of the air on damping measurements has been noted in previous research (Allen 2005). In addition, data was collected at two different sweep rates. A majority of the data was collected at a sweep rate of 4Hz/min. However, two different tests conducted on the same specimen in vacuum were done at 2Hz/min. Figure 41 also shows that the downsweeps cannot be used to approximate the loss factor of the bare beam. This is due to the fact that the downsweeps show an increase in damping as displacement increases. This phenomenon is attributable to the test set-up as it relates to minimally damped systems.
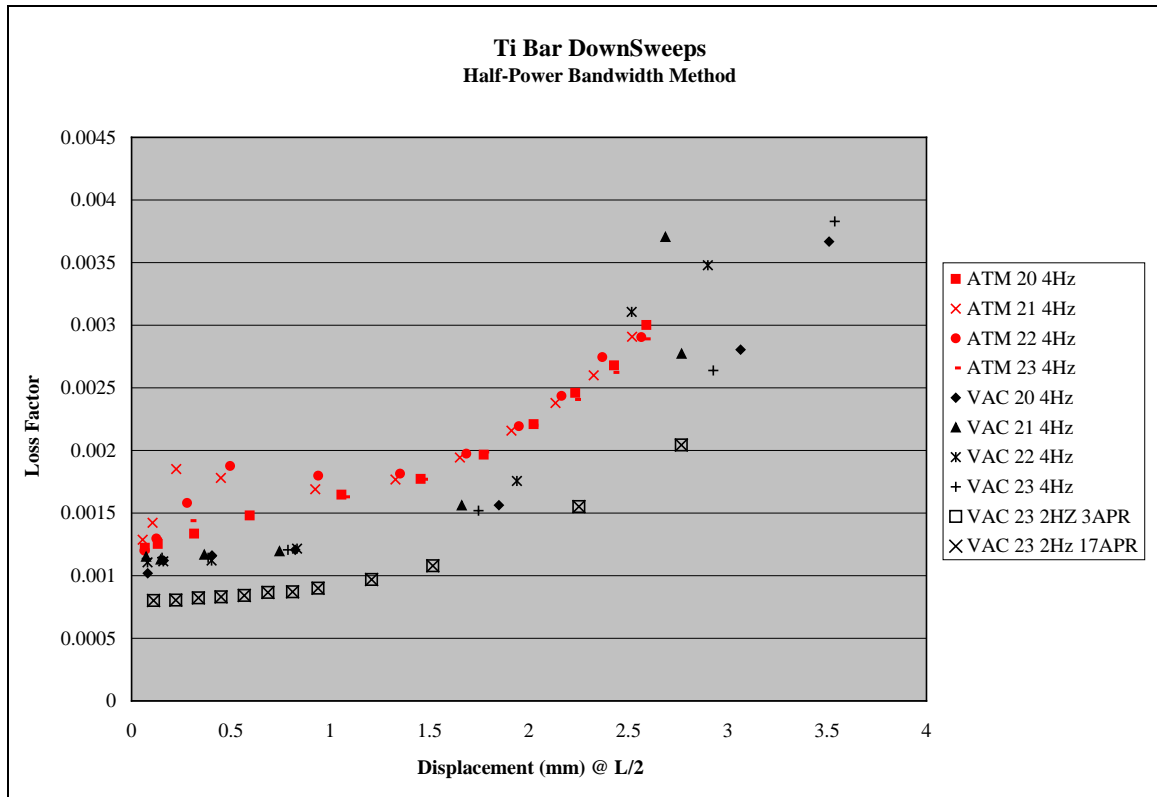
**Figure 41: Bare Beam Downsweep Tests**

Figure 42 shows the data from the upsweeps performed on the same bare beams as shown in Figure 41. Again the effects of the air can be clearly seen to be impacting the damping estimates. The upsweeps in vacuum show different trends than seen in the downsweeps under the same conditions. As displacement increase the loss factor decreases indicating a decrease in damping. Since, the specimens are Ti-6Al-4V; the loss factor is expected to remain unchanged. In addition, the sweep rates show a difference.
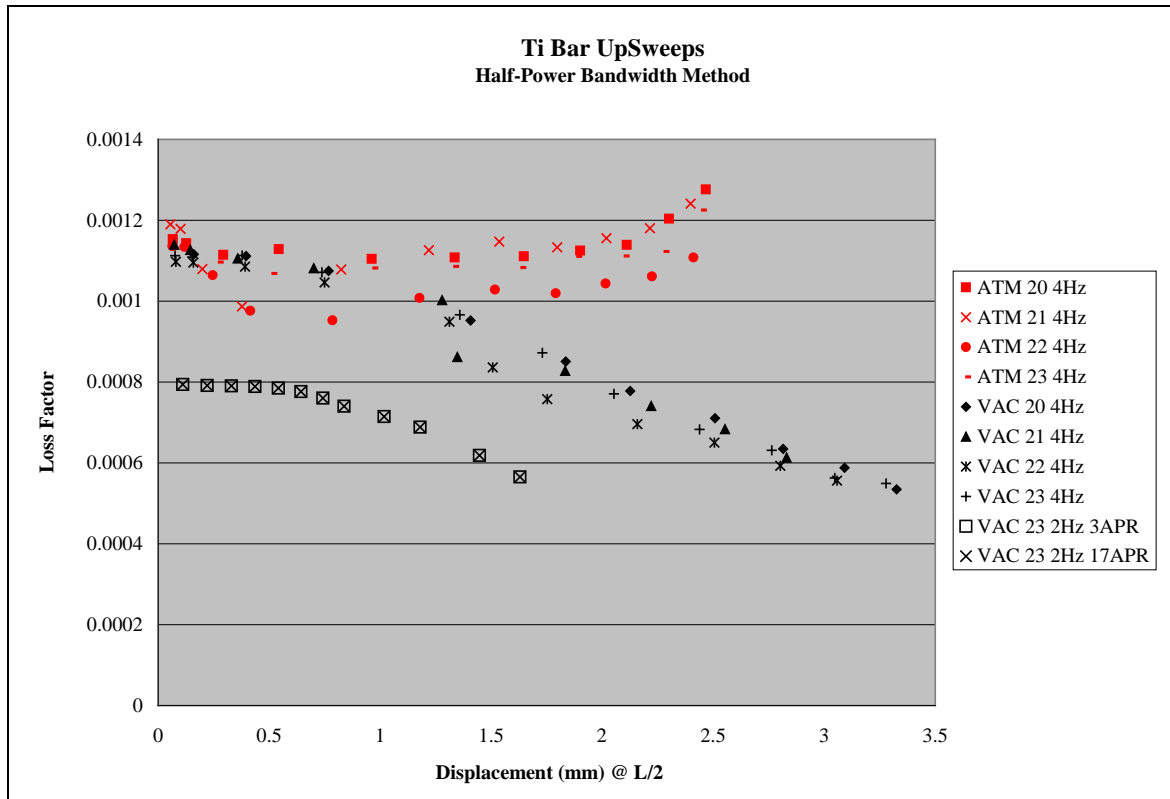
**Figure 42: Bare Beam Upsweep Tests**

Figure 43 plots the results of the different sweep rates performed with the same specimen to eliminate as many variables as possible. It confirms that the sweep rate does show a difference and that the loss factor decreases with increasing displacements. This may be a result of the non-linearity of the results at higher velocities as shown by Pearson in Figure 23.
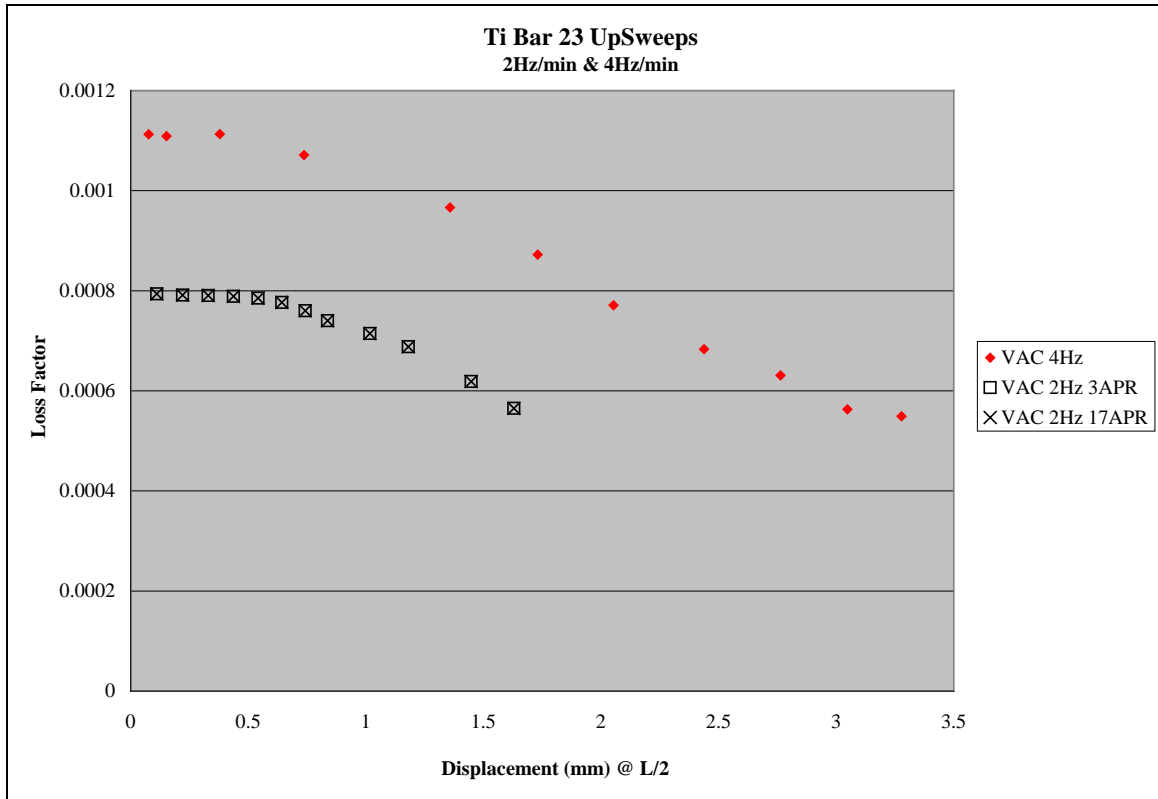
**Figure 43: Sweep Rate Differences**

The bare beam loss factor was studied in order to evaluate the test setup, since its properties are known, and also because it is a variable in Equation 6. In Reed's research (2007), it was found that using this test setup and the free decay method resulted in a loss factor of 0.0004 while Pearson used the same test setup and the forced response results with the half-power bandwidth method to approximate a loss factor of 0.0008. This value is shown in Figure 43 as the results for titanium bare beam 23 tested at 2Hz/min. This discrepancy was further investigated first by reexamining the data with the results shown and discussed above, and second the experiment was re-accomplished using titanium bare beam 23 in atmosphere. This experiment was limited to three voltages at two different sweep rates as shown in Figure 44. It was done as closely as possible to the experiment

conducted by Pearson (2008). Figure 44 again shows that in atmosphere the air provides damping that increases as the displacement of the bar increases as we should expect. The uspsweep in atmosphere shows a very similar increase in damping as displacement increases although not as rapid as the downsweep. By comparison in a vacuum the upsweep loss factor shows decreasing values as the displacement increases, as shown in Figure 42 and Figure 43. In addition to the sweep direction, the sweep rate must also be examined. It is here that the loss factor of the bare beam that was calculated in Pearson's work may be explained. Figure 44 shows that as the sweep rate was decreased the loss factor also decreased. The lowest sweep rate used during Pearson's experiment was 2Hz/min. This resulted in the loss factor of 0.0008 that Pearson calculated. It is believed that a slower sweep rate would result in a loss factor nearer to the value calculated by Reed using the free-decay method of 0.0004. The follow-up work described above and shown in Figure 44 confirms that this is indeed the case.
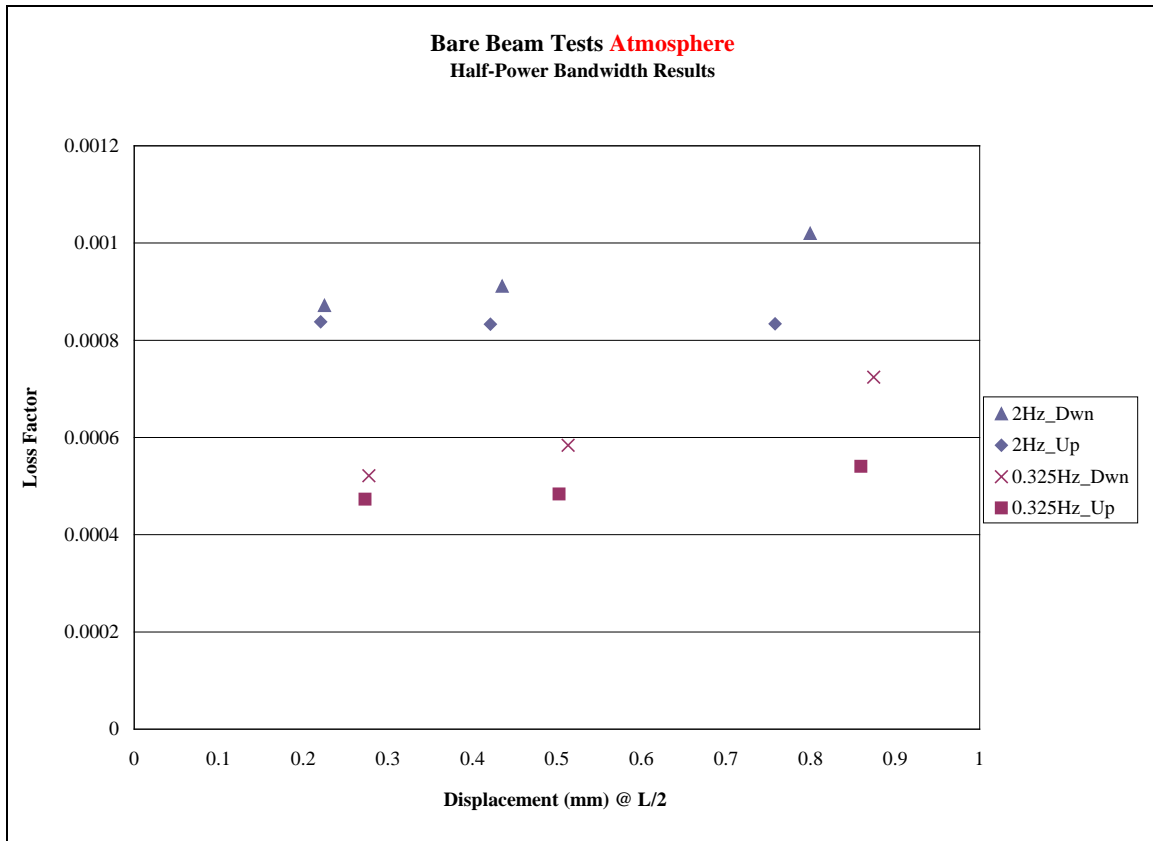
**Figure 44: Bare Beam Damping Determination**

# IV. Finite Element Model Parameter Evaluation

## *Objective*

During this study, several parameters were investigated to determine their impact on the results leading to material properties which were based on linear relationships. Therefore, the FEM included the support conditions by including the monofilament wires. Furthermore, several other parameters were evaluated such as element type; mesh density, modulus of the bare beam, and strain formulation. Other parameters that were investigated include effects of coating thickness variations and boundary conditions. One can see from Figure 45 that several external features need to be evaluated to see their effects. In order to remove boundary energy dissipation effects, an experiment was devised that reduced this energy loss. The closer a boundary duplicated a free-free condition the least chance of boundary effects on energy dissipation. The test set-up was evaluated in order to see how close it became to a free-free boundary.
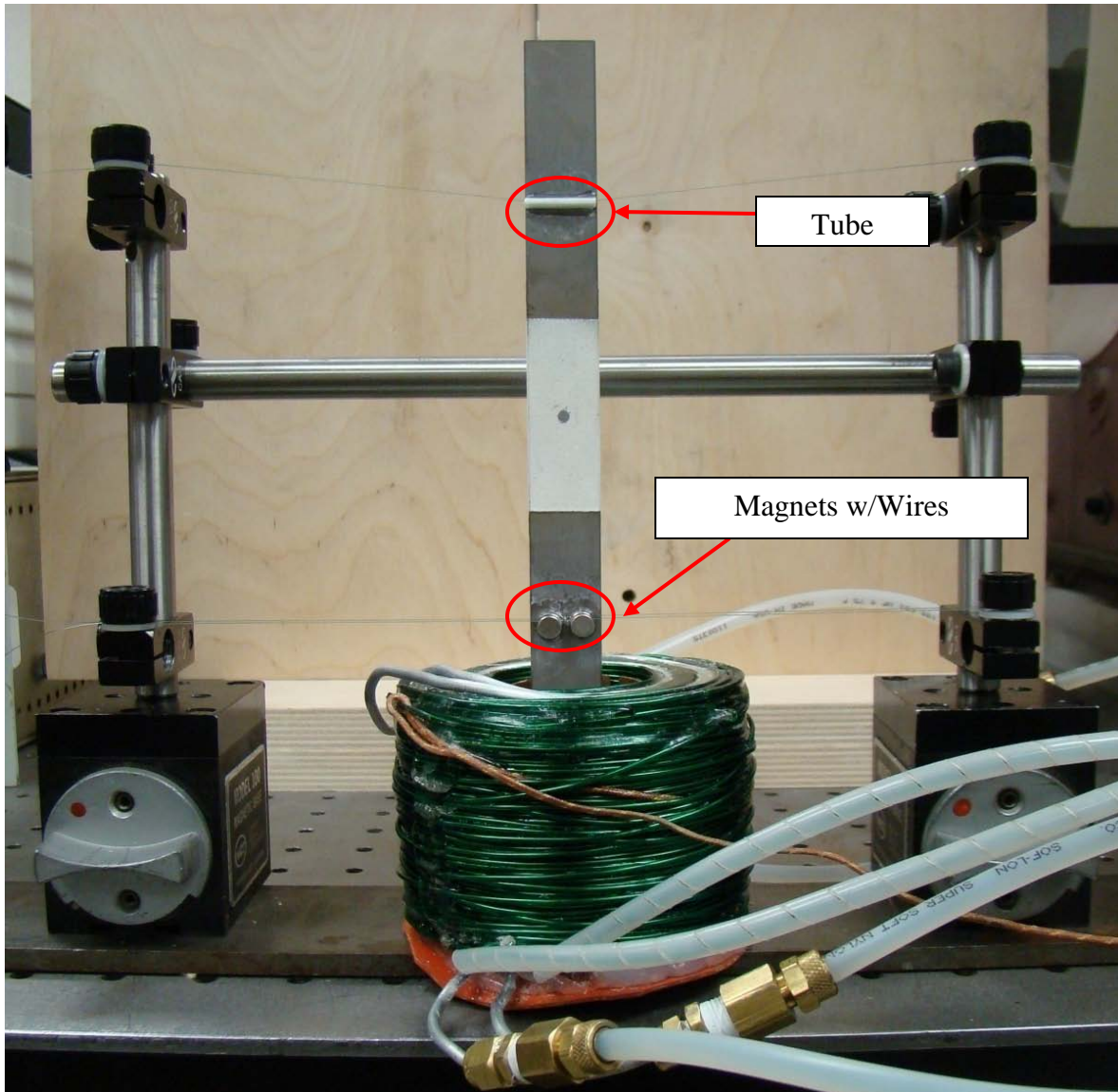
**Figure 45: Test Set-up**

## *Finite Element Model Development*

Several steps will be outlined that were taken during the creation of the FEM.  The first was to find the theoretical frequency for a free-free beam composed of TI-6AL-4V. Equation 10 was used to calculate the theoretical frequency (Timoshenko, Young, and Weaver, 1974).

*Theoretical value for a free-free beam first bending mode*

$$f = \frac{k_1^2 a}{2\pi} \qquad k_1 = \frac{4.730}{l} \qquad a = \sqrt{\frac{EI}{\rho A}} \tag{10}$$

Where:
$l$ – Beam Length
$E$ –  Beam Modulus
$I$ –  Moment of Inertia
$\rho$ –  Beam density
$A$ –  cross-sectional Area

Once this frequency was determined, a FEM of the beam was created and various elements used in an attempt to match the theoretical frequency as closely as possible. There were several elements to choose from in ABAQUS and four were used and compared.  Four of the elements were eight-noded linear brick elements and the other two were 20-noded quadratic brick element.  The results are displayed in Table 4.  It is clear from this comparison that the ABAQUS element denoted as C3D8I is the element of choice for this application as it most closely matched the theoretical frequency.  This is the element that was used during the remainder of this research.

**Table 4: Free-Free Element Comparison**

|  | Theoretical | ABAQUS | | | | | |
|---|---|---|---|---|---|---|---|
| Element Type | N/A | C3D8 | C3D8H | C3D8R | C3D8I | C3D20 | C3D20R |
| Young's Modulus$_{beam}$ (Gpa) | 113.8 | 113.8 | | | | | |
| Poisson's Ratio$_{beam}$ (Gpa) | N/A | 0.34200001 | | | | | |
| Density$_{beam}$ (g/mm^3) | N/A | 0.00443 | | | | | |
| Frequency (Hz) | **201.88** | 217.87 | 217.87 | 175.23 | **201.94** | 201.97 | 201.97 |
| Element # | N/A | 4800 | 4800 | 4800 | 4800 | 4800 | 4800 |
| Node # | N/A | 7728 | 12528 | 7728 | 31728 | 27805 | 27805 |
| Run Time (sec) | N/A | 12 | 11 | 9 | 19 | 54 | 52 |

This element is an attempt to remedy the problem of shear locking exhibited by the eight-node solid element.  This is due to spurious shear strain that is exhibited when beam bending modes are displayed (Cook et al 2004).  This software adds incompatible deformation modes to the standard eight-noded element to eliminate the artificial stiffening that occur in normal first-order elements.  These elements are somewhat more expensive due to the additional nodes, but they are less expensive then the second-order elements as shown in Table 4 (ABAQUS User's Manual v. 6.8).  Once the element type was chosen, the mesh density was investigated.  This consisted of comparing three models of the coated beam.  As the coating modulus has yet to be determined, 40 GPa was chosen for all three models for comparison.  Pearson's model consisted of 5632 3D 8-noded elements with an element size of 1.27 mm X 1.27 mm X 0.8 mm.  This was taken as the least dense mesh for this comparison.  The next model created had a slightly denser mesh overall.  However, at the eigenvector node locations and at the coating interface, the mesh was denser with an equivalent sided element measuring 0.5mm per side.  This was done in order to get a better estimate of strain.  The SER is dependent on the strain in the coating.  In addition, the monofilament wire supports used in the

experiment were located at the eigenvector nodes.  Thus the modeled supports were

projected to be located in similar positions.  Thus the finer mesh gets nearer to the

eigenvector nodes theoretically minimizing modeling error.  The model labeled as three

used the same 0.5mm per side element throughout.  Table 5 and

Table 6 show the results of this study.  We can see that the normalized strain values as

well as the normalized displacement values converged to a value.  The SER continued to

slowly converge with the energy dependent on the number of elements.  Model three was

chosen for the evaluation portion of this study based on its values converging with the

last model and its moderate number of elements.

**Table 5: Mesh Density (Free Free beam)**

| Model | Element Dimensions (mm) (L x W x H) | Node # | Element # |
|-------|-------------------------------------|--------|-----------|
| 1 | 1.27x1.27x0.8 | 77224 | 12000 |
| 2 | 0.7x0.56x0.6 | 307678 | 48720 |
| 3 | 0.5x0.5x0.6 | 416274 | 65892 |

**Table 6: Model Comparison (Free Free beam)**

| Model | $f_n$ [Hz] | $U_{sys}$ | $U_c$ | SER | $\varepsilon_{11}$ | | Transverse Displacement | |
|-------|-----------|-----------|-------|-----|---------|---------|---------|---------|
| | | | | | x/L=0.4 | x/L=0.5 | x/L=0.4 | x/L=0.5 |
| 1 | 218.22 | 15.84 | 5.15 | 0.325 | 2.579e-4 | 2.813e-4 | -0.4564 | -0.5335 |
| 2 | 218.35 | 83.11 | 26.51 | 0.319 | 2.59e-4 | 2.809e-4 | -0.4586 | -0.5334 |
| 3 | 218.35 | 109.3 | 31.36 | 0.287 | 2.59e-4 | 2.809e-4 | -0.4599 | -0.5334 |

 In this research, several simplifications occurred during the creation of this FEM.  One

of the assumptions that was duplicated from the prior work was the simplification of

66

omitting the bond coat from the FEM. Figure 46 below is from Pearson's thesis and shows the relative dimension of the bond coat to the coating and the titanium bar. It was assumed that the bond coat's interaction was relative to its dimensionality.
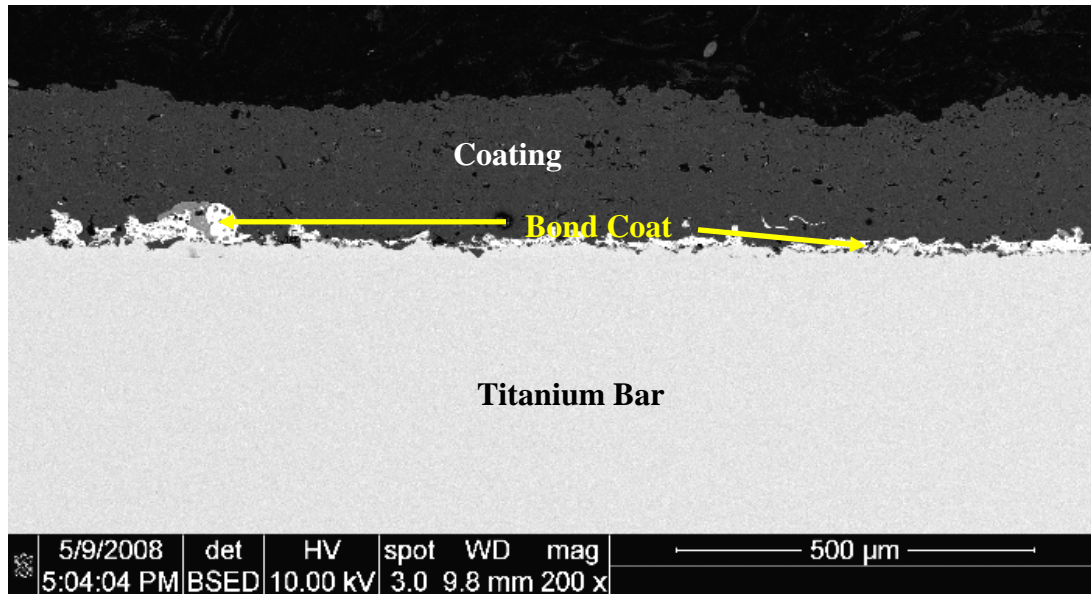


**Figure 46: SEM showing bond coat**

In addition, the magnets were modeled as simple rectangular blocks versus the actual cylinders that were used, as shown in Figure 47. The Figure consists of a picture of the magnets used in the experiment by Pearson (2008) and the modeled magnets. The magnets were modeled by adjusting the mass of the modeled magnets so that the mass of each rectangle block was equal to two actual magnets. Eight magnets were used in the experiment with four per side, stacked two high. The modeled magnets consist of four blocks, stacked two per side. This was done to eliminate a relatively unimportant variable that might otherwise appear when comparing any results to previous work.
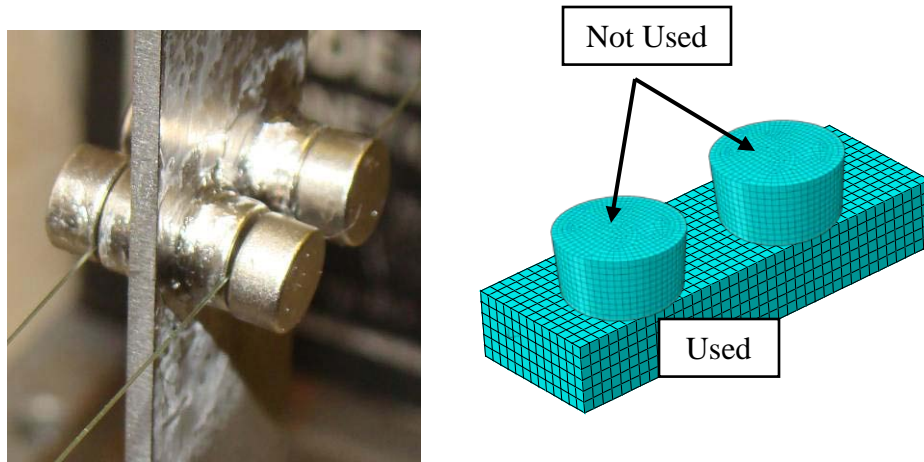
**Figure 47: Actual Magnet vs. Modeled Magnet**

## *Modulus of Bare Beam*

The beam used in this study was made of Ti-6AL-4V.  This is known as the "workhorse"
of the Titanium industry because it is the most common Ti alloy.  In previous work, the
FEM was "tuned" by varying the Modulus of Elasticity of the Ti-6AL-4V until the
frequency of the eigenvector matched the frequency measured in the experiment.  In
Pearson's work this value was approximately 110.5 GPa while in Reed's work this value
was approximately 118.5GPa.  The published value for Ti-6AL-4V is in the range of
113.8GPa – 115GPa (*MatWeb material property data,* 2008).  The discrepancy was
believed to be due to the effect of the magnets as well as the setup being an
approximation of free-free boundary conditions.  The monofilament wires (discussed
subsequently) were also thought to play a role.  In this study the published values were
used to examine the effects they had on the results.  In addition, the monofilament wires
were modeled in the FEM with the intention of verifying the premise that the

experimental setup could be modeled with FE by "tuning" the FEM using the modulus of
the Ti-6AL-4V.
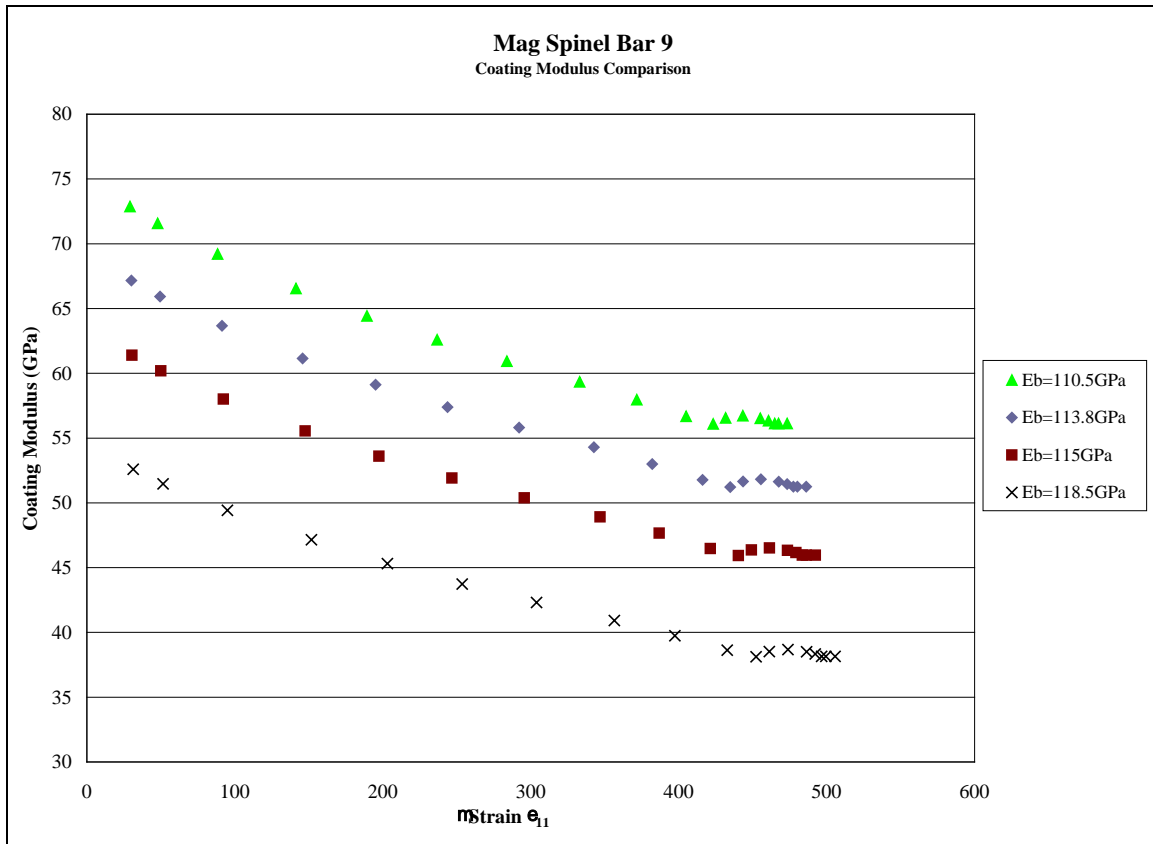


**Figure 48: Beam Modulus Comparison**

Figure 48 plots the $E_c$ for four values of $E_b$.  Table 7 shows that the differences do affect

the results.  In particular it shows that the increased $E_b$ stiffens the FEM as we would

expect.  Increased stiffness leads to lower $E_c$ at each strain experienced at the interface.

Table 7 shows the percent difference between the values is just over 38%.  In comparison

the percent difference between 110.5 GPa and 118.5 GPa is just under 7%.

**Table 7: Coating Modulus Differences**

| $\mu$Strain $\varepsilon_{11}$ | 110.5 (GPa) | 118.5 (GPa) | MEAN (GPa) | STD DEV | % Difference |
|---|---|---|---|---|---|
| 30 | 72.87 | 52.59 | 62.731 | 10.140 | 32.328 |
| 49 | 71.57 | 51.47 | 61.518 | 10.049 | 32.670 |
| 91 | 69.20 | 49.43 | 59.317 | 9.885 | 33.329 |
| 146 | 66.55 | 47.14 | 56.845 | 9.701 | 34.131 |
| 195 | 64.42 | 45.31 | 54.867 | 9.554 | 34.826 |
| 244 | 62.59 | 43.74 | 53.164 | 9.428 | 35.467 |
| 292 | 60.94 | 42.31 | 51.622 | 9.314 | 36.085 |
| 343 | 59.33 | 40.92 | 50.127 | 9.204 | 36.721 |
| 382 | 57.97 | 39.75 | 48.857 | 9.110 | 37.293 |
| 416 | 56.67 | 38.63 | 47.652 | 9.022 | 37.865 |
| 435 | 56.09 | 38.12 | 47.104 | 8.981 | 38.134 |
| 444 | 56.55 | 38.53 | 47.539 | 9.013 | 37.920 |
| 456 | 56.73 | 38.68 | 47.705 | 9.026 | 37.839 |
| 468 | 56.53 | 38.50 | 47.514 | 9.012 | 37.932 |
| 473 | 56.33 | 38.34 | 47.336 | 8.998 | 38.020 |
| 478 | 56.12 | 38.15 | 47.132 | 8.984 | 38.120 |
| 480 | 56.12 | 38.15 | 47.132 | 8.984 | 38.120 |
| 486 | 56.12 | 38.15 | 47.132 | 8.984 | 38.120 |

Figure 49 shows that the loss factor of mag spinel is affected by the choice of $E_b$. Table 8 confirms that these values are impacted by choice of $E_b$. This leads to a percent difference of approximately 12.4% as compared to the 7% difference between the inputs. It is clear that $E_b$ should be determined experimentally to ensure increased accuracy with this experiment. However, some of the disparity is explained by keeping in mind that the experimental data that was used to generate these values was the same in both cases. If the experimental data was generated with materials closer to those input into the FEM then the results would be closer.
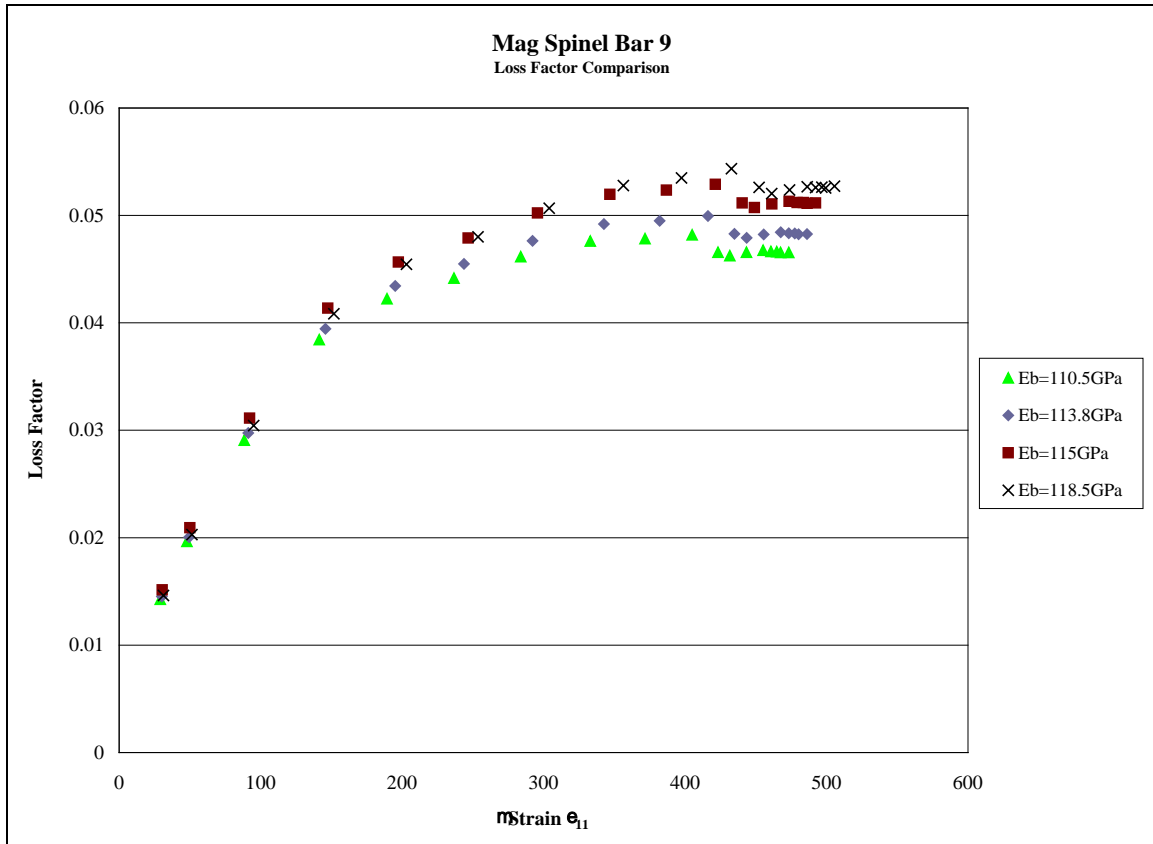


**Figure 49: Beam Modulus - Loss Factor Comparison**

**Table 8: Loss Factor Differences**

| μStrain $\varepsilon_{11}$ | 110.5 (GPa) | 118.5 (GPa) | MEAN | STD DEV | % Difference |
|---|---|---|---|---|---|
| 30 | 1.426E-02 | 1.462E-02 | 1.444E-02 | 1.807E-04 | 2.502 |
| 49 | 1.965E-02 | 2.029E-02 | 1.997E-02 | 3.223E-04 | 3.228 |
| 91 | 2.908E-02 | 3.044E-02 | 2.976E-02 | 6.796E-04 | 4.567 |
| 146 | 3.844E-02 | 4.085E-02 | 3.965E-02 | 1.206E-03 | 6.085 |
| 195 | 4.225E-02 | 4.545E-02 | 4.385E-02 | 1.601E-03 | 7.303 |
| 244 | 4.417E-02 | 4.801E-02 | 4.609E-02 | 1.918E-03 | 8.325 |
| 292 | 4.617E-02 | 5.067E-02 | 4.842E-02 | 2.254E-03 | 9.312 |
| 343 | 4.761E-02 | 5.278E-02 | 5.019E-02 | 2.584E-03 | 10.295 |
| 382 | 4.783E-02 | 5.348E-02 | 5.066E-02 | 2.825E-03 | 11.155 |
| 416 | 4.820E-02 | 5.434E-02 | 5.127E-02 | 3.075E-03 | 11.995 |
| 435 | 4.658E-02 | 5.262E-02 | 4.960E-02 | 3.019E-03 | 12.174 |
| 444 | 4.625E-02 | 5.204E-02 | 4.914E-02 | 2.894E-03 | 11.776 |
| 456 | 4.656E-02 | 5.238E-02 | 4.947E-02 | 2.908E-03 | 11.755 |
| 468 | 4.676E-02 | 5.266E-02 | 4.971E-02 | 2.954E-03 | 11.884 |
| 473 | 4.664E-02 | 5.259E-02 | 4.962E-02 | 2.973E-03 | 11.985 |
| 478 | 4.663E-02 | 5.262E-02 | 4.963E-02 | 2.998E-03 | 12.083 |
| 480 | 4.656E-02 | 5.256E-02 | 4.956E-02 | 3.000E-03 | 12.105 |
| 486 | 4.654E-02 | 5.272E-02 | 4.963E-02 | 3.087E-03 | 12.440 |

Figure 50 shows that the Loss Modulus is also affected by $E_b$ choice. Table 9 displays the percent difference between the two cases as just below 30% at the highest obtained strain.
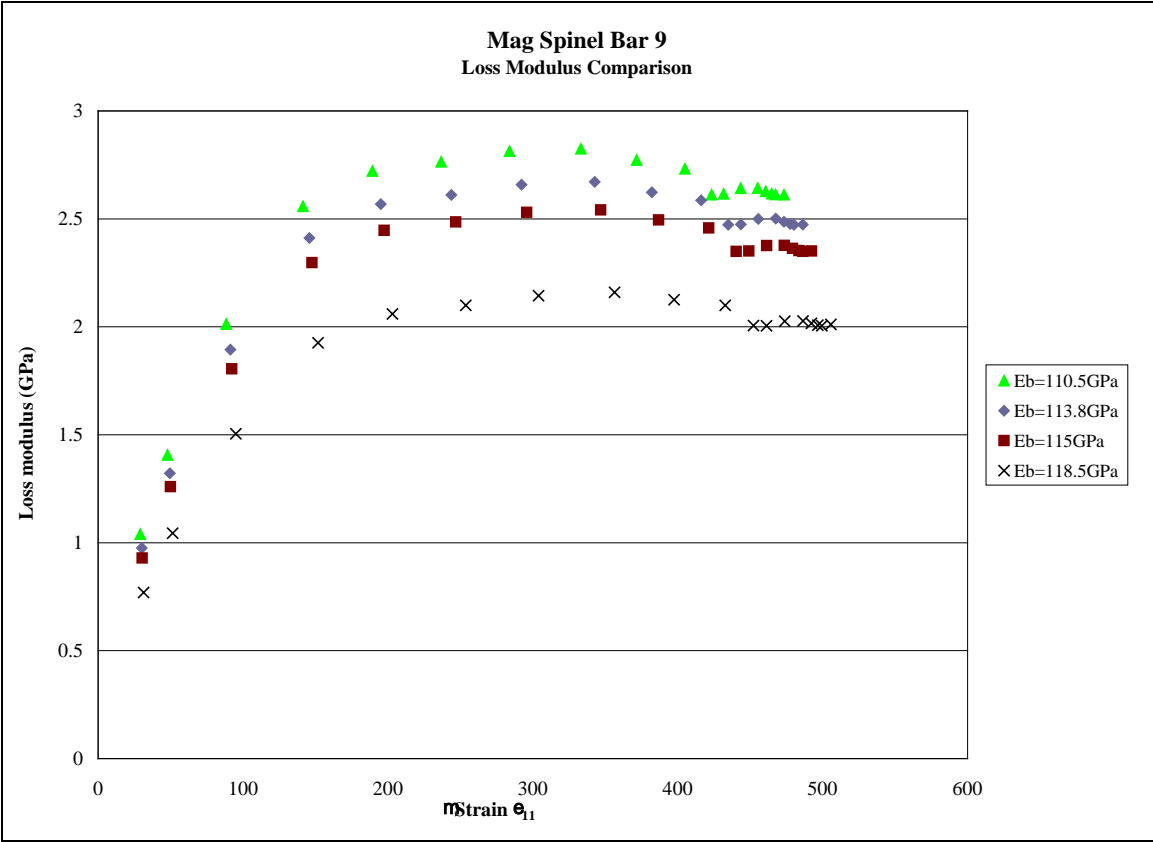


**Figure 50: Beam Modulus - Loss Modulus Comparison**

**Table 9: Loss Modulus Differences**

| μStrain $\varepsilon_{11}$ | 110.5 (GPa) | 118.5 (GPa) | MEAN (GPa) | STD DEV | % Difference |
|---|---|---|---|---|---|
| 30 | 1.039 | 0.769 | 0.90 | 0.135 | 29.886 |
| 49 | 1.406 | 1.045 | 1.23 | 0.181 | 29.521 |
| 91 | 2.013 | 1.505 | 1.76 | 0.254 | 28.872 |
| 146 | 2.558 | 1.926 | 2.24 | 0.316 | 28.192 |
| 195 | 2.722 | 2.060 | 2.39 | 0.331 | 27.699 |
| 244 | 2.765 | 2.100 | 2.43 | 0.333 | 27.344 |
| 292 | 2.813 | 2.144 | 2.48 | 0.335 | 27.000 |
| 343 | 2.825 | 2.160 | 2.49 | 0.332 | 26.679 |
| 382 | 2.773 | 2.126 | 2.45 | 0.323 | 26.413 |
| 416 | 2.731 | 2.099 | 2.42 | 0.316 | 26.167 |
| 435 | 2.612 | 2.006 | 2.31 | 0.303 | 26.265 |
| 444 | 2.615 | 2.005 | 2.31 | 0.305 | 26.439 |
| 456 | 2.642 | 2.026 | 2.33 | 0.308 | 26.378 |
| 468 | 2.643 | 2.028 | 2.34 | 0.308 | 26.345 |
| 473 | 2.628 | 2.016 | 2.32 | 0.306 | 26.334 |
| 478 | 2.617 | 2.008 | 2.31 | 0.305 | 26.341 |
| 480 | 2.613 | 2.005 | 2.31 | 0.304 | 26.319 |
| 486 | 2.612 | 2.011 | 2.31 | 0.300 | 25.989 |

## *Coating Thickness*

Table 10 is from Pearson's thesis and shows that there was variation in the coating

thickness. As stated earlier the bond coat was ignored in this analysis. In order to easily

see the effects on the material properties the nominal coating thickness of 0.25 mm was

doubled to 0.5 mm. In addition to the physical variation of the coating thickness there

was another reason to investigate the thickness. Figure 3 clearly shows that the coating

was on all four sides of the beam. This was not included in the FEM. This extra coating

accounts for approximately 5% of the total mass of the coating, assuming equal thickness

on all four sides. By varying the thickness of the coating we can compensate for this

effect.

**Table 10: Dimensions**

| Specimen | Thickness, $t_c$ (mm) | Width (mm) | Length, $L_c$ (mm) | Mass (g) | Density, $\rho_c$ (g/cm$^3$) |
|----------|------------|------------|------------|----------|------------|
| Bond Coat Only | | | | | |
| 1 | 0.0485 | 19.18 | 51.05 | 0.118 | 1.27 |
| 5 | 0.0478 | 19.13 | 51.66 | 0.072 | 0.80 |
| 6 | 0.0631 | 19.11 | 50.67 | 0.127 | 1.06 |
| 7 | 0.0552 | 19.08 | 51.36 | 0.144 | 1.43 |
| 8 | 0.0578 | 19.09 | 50.65 | 0.134 | 1.27 |
| Bond+Mag Spinel | | | | | |
| 2 | 0.268 | 19.35 | 50.83 | 1.453 | 2.681 |
| 3 | 0.256 | 19.30 | 51.33 | 1.447 | 2.774 |
| 4 | 0.250 | 19.35 | 51.31 | 1.302 | 2.552 |
| 9 | 0.256 | 19.34 | 52.07 | 1.491 | 2.822 |
| 15 | 0.267 | 19.33 | 52.30 | 1.551 | 2.800 |

Figure 51 shows the results of doubling the thickness of the coating from 0.25 mm per

side to 0.5 mm per side. This added mass creates a stiffer structure as we would expect.
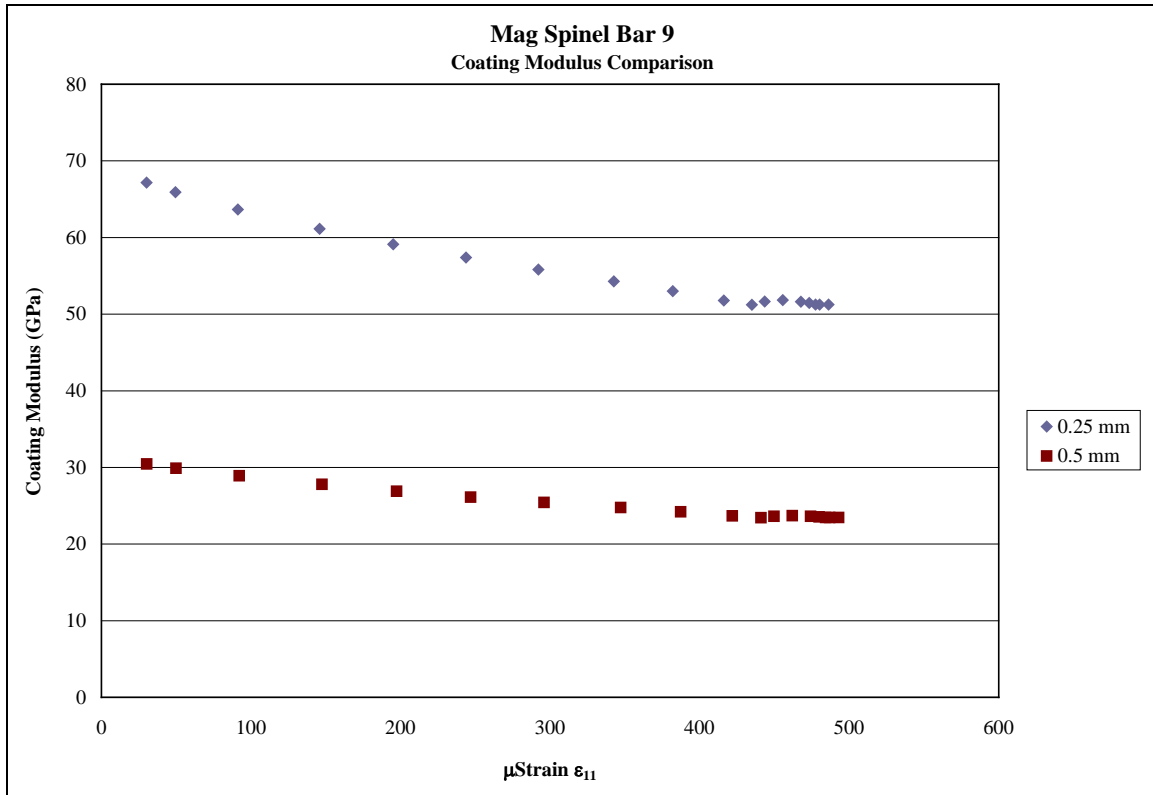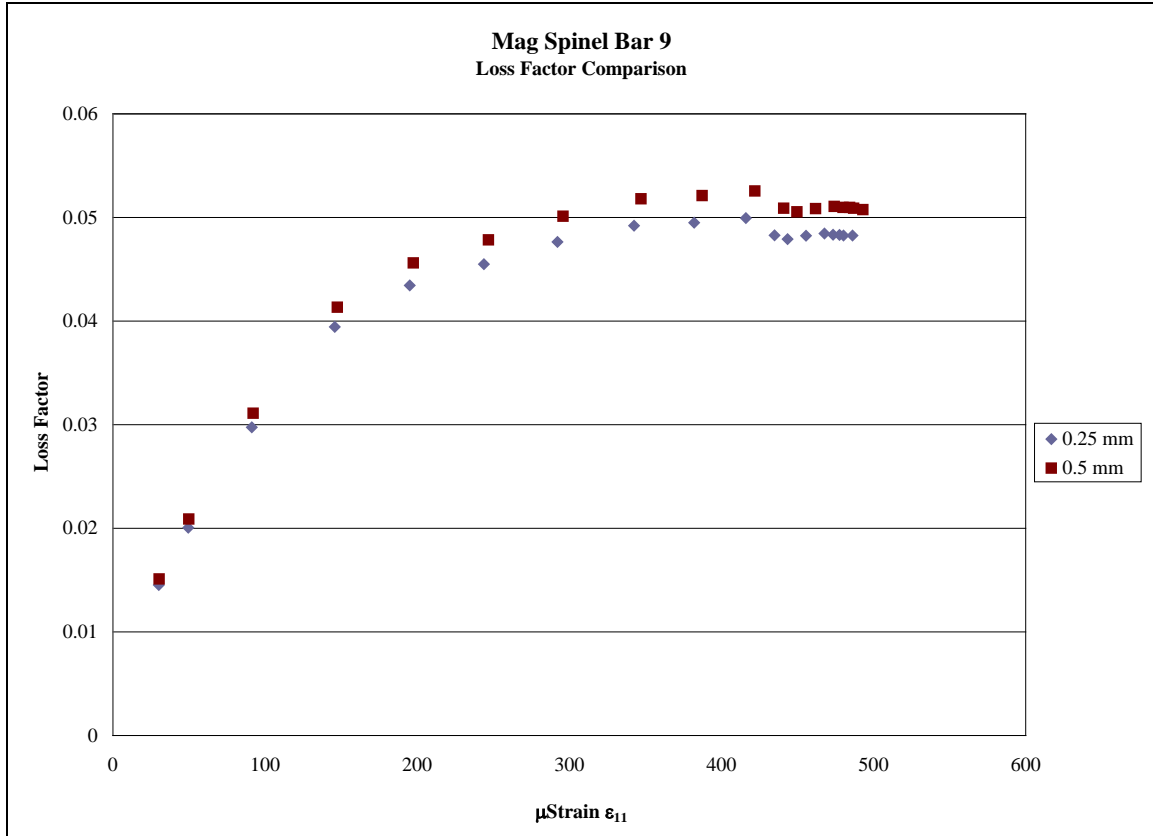
**Figure 51: Coating Thickness Comparison - $E_c$**

It is important to keep in mind that the data used with both models is the same. This results in errors to the outputs. Since the coating mass is greater than the modeled coating mass, it can be inferred that the true results are somewhere in between the ones shown in Figure 51, Figure 52, and Figure 53. It is interesting to note that these results add further evidence that the FEM used in previous work was stiffer then the ABAQUS model used for this research. The percent difference for the coating modulus is shown as approximately 18.8% in Table 11. This is compared to a percent difference of 33% in thickness as input into the FEM.

**Table 11: Coating Modulus Comparison**

| μStrain $\varepsilon_{11}$ | 0.25 mm | 0.5 mm | Mean (GPa) | STD DEV | % Difference |
|---|---|---|---|---|---|
| 30 | 67.163 | 30.456 | 48.810 | 18.353 | 18.80 |
| 50 | 65.922 | 29.902 | 47.912 | 18.010 | 18.79 |
| 92 | 63.671 | 28.900 | 46.286 | 17.385 | 18.78 |
| 147 | 61.146 | 27.781 | 44.464 | 16.682 | 18.76 |
| 197 | 59.127 | 26.891 | 43.009 | 16.118 | 18.74 |
| 247 | 57.390 | 26.128 | 41.759 | 15.631 | 18.72 |
| 296 | 55.817 | 25.439 | 40.628 | 15.189 | 18.69 |
| 347 | 54.294 | 24.775 | 39.534 | 14.760 | 18.67 |
| 387 | 53.000 | 24.212 | 38.606 | 14.394 | 18.64 |
| 422 | 51.773 | 23.680 | 37.727 | 14.046 | 18.62 |
| 441 | 51.216 | 23.440 | 37.328 | 13.888 | 18.60 |
| 450 | 51.659 | 23.631 | 37.645 | 14.014 | 18.61 |
| 462 | 51.828 | 23.704 | 37.766 | 14.062 | 18.62 |
| 474 | 51.633 | 23.620 | 37.627 | 14.007 | 18.61 |
| 480 | 51.452 | 23.541 | 37.497 | 13.955 | 18.61 |
| 484 | 51.245 | 23.452 | 37.348 | 13.896 | 18.60 |
| 487 | 51.245 | 23.452 | 37.348 | 13.896 | 18.60 |
| 493 | 51.245 | 23.452 | 37.348 | 13.896 | 18.60 |

**Figure 52: Coating Thickness Comparison - $\eta_{coat}$**

Figure 52 compares the loss factor calculated for the original coating thickness of 0.25 mm versus the input thickness of 0.5 mm. This shows that the coating thickness does not show as much of an effect as it does on the coating modulus. Table 12 lists a percent difference of about 1.3% which is very small compared to the input difference of 33%. This is likely due to the coating not changing the SER as much as the beam does. Hence, the beam modulus changed the loss factor to a greater degree then the coating thickness.

**Table 12: Loss Factor Comparison**

| μStrain $\varepsilon_{11}$ | 0.25 mm | 0.5 mm | Mean | STD DEV | % Difference |
|---|---|---|---|---|---|
| 30 | 1.453E-02 | 1.511E-02 | 1.482E-02 | 2.918E-04 | 0.984 |
| 50 | 2.005E-02 | 2.090E-02 | 2.047E-02 | 4.242E-04 | 1.036 |
| 92 | 2.975E-02 | 3.111E-02 | 3.043E-02 | 6.763E-04 | 1.111 |
| 147 | 3.944E-02 | 4.134E-02 | 4.039E-02 | 9.509E-04 | 1.177 |
| 197 | 4.344E-02 | 4.561E-02 | 4.452E-02 | 1.085E-03 | 1.218 |
| 247 | 4.550E-02 | 4.783E-02 | 4.667E-02 | 1.170E-03 | 1.253 |
| 296 | 4.763E-02 | 5.012E-02 | 4.887E-02 | 1.242E-03 | 1.271 |
| 347 | 4.920E-02 | 5.179E-02 | 5.050E-02 | 1.293E-03 | 1.280 |
| 387 | 4.950E-02 | 5.210E-02 | 5.080E-02 | 1.301E-03 | 1.280 |
| 422 | 4.994E-02 | 5.256E-02 | 5.125E-02 | 1.306E-03 | 1.275 |
| 441 | 4.828E-02 | 5.089E-02 | 4.959E-02 | 1.303E-03 | 1.314 |
| 450 | 4.791E-02 | 5.054E-02 | 4.922E-02 | 1.315E-03 | 1.336 |
| 462 | 4.823E-02 | 5.084E-02 | 4.954E-02 | 1.305E-03 | 1.317 |
| 474 | 4.844E-02 | 5.107E-02 | 4.976E-02 | 1.311E-03 | 1.317 |
| 480 | 4.834E-02 | 5.096E-02 | 4.965E-02 | 1.312E-03 | 1.321 |
| 484 | 4.833E-02 | 5.097E-02 | 4.965E-02 | 1.320E-03 | 1.329 |
| 487 | 4.826E-02 | 5.088E-02 | 4.957E-02 | 1.313E-03 | 1.325 |
| 493 | 4.827E-02 | 5.075E-02 | 4.951E-02 | 1.240E-03 | 1.253 |
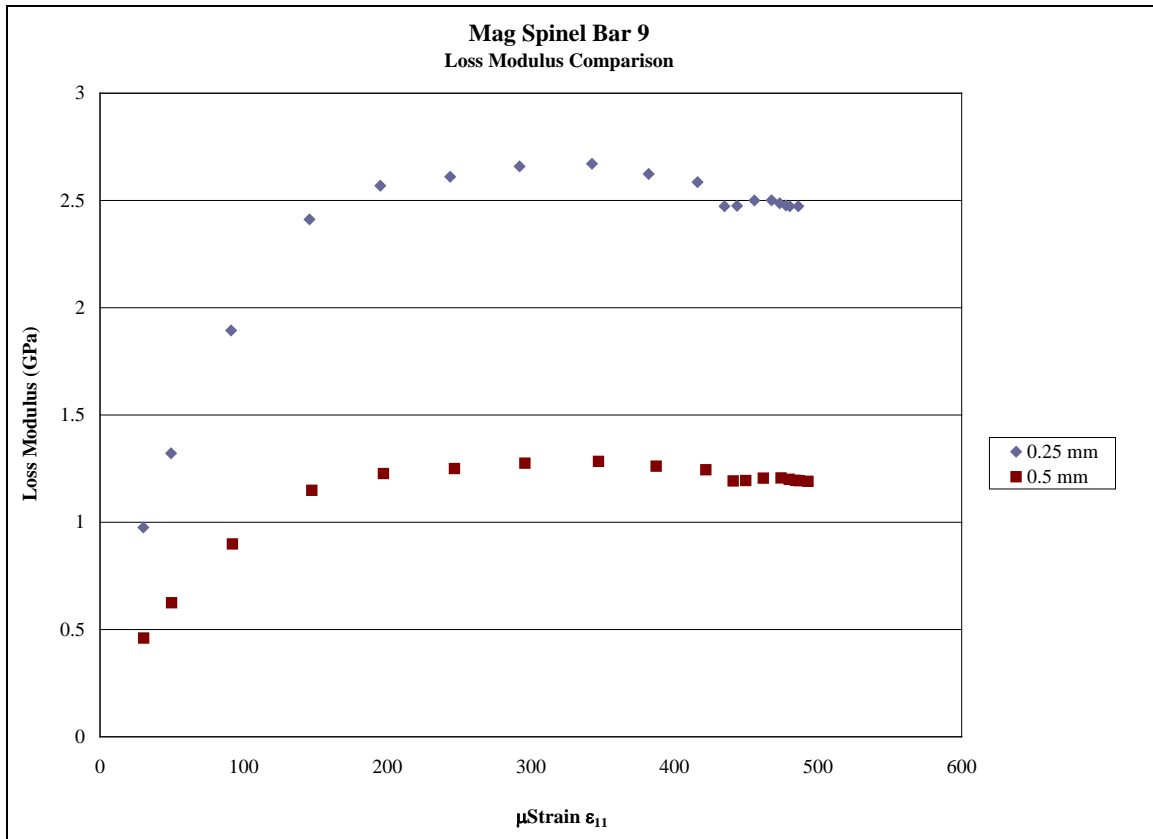
**Figure 53: Coating Thickness Comparison - Loss Modulus**

The loss modulus plot in Figure 53 shows a similar difference as the coating modulus while retaining the shape of the curves of the loss factor. Table 13 lists the percent difference between the two results.

**Table 13: Loss Modulus Comparison**

| μStrain $\varepsilon_{11}$ | 0.25 mm | 0.5 mm | Mean | STD DEV | % Difference |
|---|---|---|---|---|---|
| 30 | 0.976 | 0.460 | 0.718 | 2.578E-01 | 17.949 |
| 50 | 1.322 | 0.625 | 0.973 | 3.484E-01 | 17.898 |
| 92 | 1.894 | 0.899 | 1.397 | 4.977E-01 | 17.818 |
| 147 | 2.411 | 1.148 | 1.780 | 6.315E-01 | 17.739 |
| 197 | 2.568 | 1.226 | 1.897 | 6.710E-01 | 17.681 |
| 247 | 2.611 | 1.250 | 1.930 | 6.806E-01 | 17.628 |
| 296 | 2.659 | 1.275 | 1.967 | 6.919E-01 | 17.589 |
| 347 | 2.671 | 1.283 | 1.977 | 6.942E-01 | 17.555 |
| 387 | 2.624 | 1.262 | 1.943 | 6.810E-01 | 17.529 |
| 422 | 2.586 | 1.245 | 1.915 | 6.706E-01 | 17.507 |
| 441 | 2.473 | 1.193 | 1.833 | 6.400E-01 | 17.460 |
| 450 | 2.475 | 1.194 | 1.835 | 6.403E-01 | 17.451 |
| 462 | 2.500 | 1.205 | 1.853 | 6.473E-01 | 17.472 |
| 474 | 2.501 | 1.206 | 1.854 | 6.476E-01 | 17.467 |
| 480 | 2.487 | 1.200 | 1.843 | 6.437E-01 | 17.459 |
| 484 | 2.477 | 1.195 | 1.836 | 6.406E-01 | 17.447 |
| 487 | 2.473 | 1.193 | 1.833 | 6.398E-01 | 17.451 |
| 493 | 2.473 | 1.190 | 1.832 | 6.416E-01 | 17.514 |

## *Strain*

While studying the material properties of the coating material it is useful to plot their values versus strain. This is a method of normalizing the properties by accounting for the different voltages used in the tests. The voltages that were chosen for the study were not consistent in their range. The coated beams were tested between 50mV and 8000mV with the 18 voltages chosen not evenly spaced. In, addition the response of the coated beam for a specific voltage could not be assumed to be a multiple of another voltage. For instance, the response of a coated beam at 500mV could not be assumed to be 10 times the response of the coated beam tested at 50mV. By using strain, we eliminate this problem and can analyze the material properties properly. As part of the process of determing the strain in the coated beam the FEM must be used as described in the section labelled Procedure. Once the scaling factor $\lambda$ is found it is applied to the normalized strains to determine the actual strains. The normalized strains are calculated by the FEM in the center of the coated beam at the beam coating interface. There are several strains that one could use. The strains in the transverse direction or the strains in the longitudinal direction are obvious candidates. The strains in either direction would work but the longitudinal strains are used due to their larger magnitudes. This is because the nodal strains are the averaged values of the surrounding elements. The larger the magnitudes the less the percentage error assuming the relative error is constant for both cases. As was mentioned the node of interest is located at the interface between the beam and the coating. So the nodal strain lists the averaged values from the eight surrounding

82

elements. Each or the surrounding elements is made up of eight nodes. The strain is calculated at each of the nodes wihich are averaged to return an elemental value. These are the values listed for the node of interest. In this case the eight values include averages from four elements with material properties of the beam and four elements with material proerties of the coating. This is shown in Figure 54. We can look at the strains averaged in the eight elements that connect to the node, or we can look at the eight integration points in the element in the center of the beam and not in the coating. The strain in the transverse direction is $\varepsilon_{22}$ remains linear as it goes from titanium beam to coating.
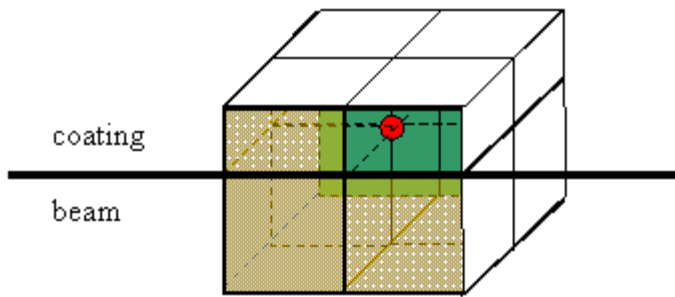


**Figure 54: Eight Elements surround Node**
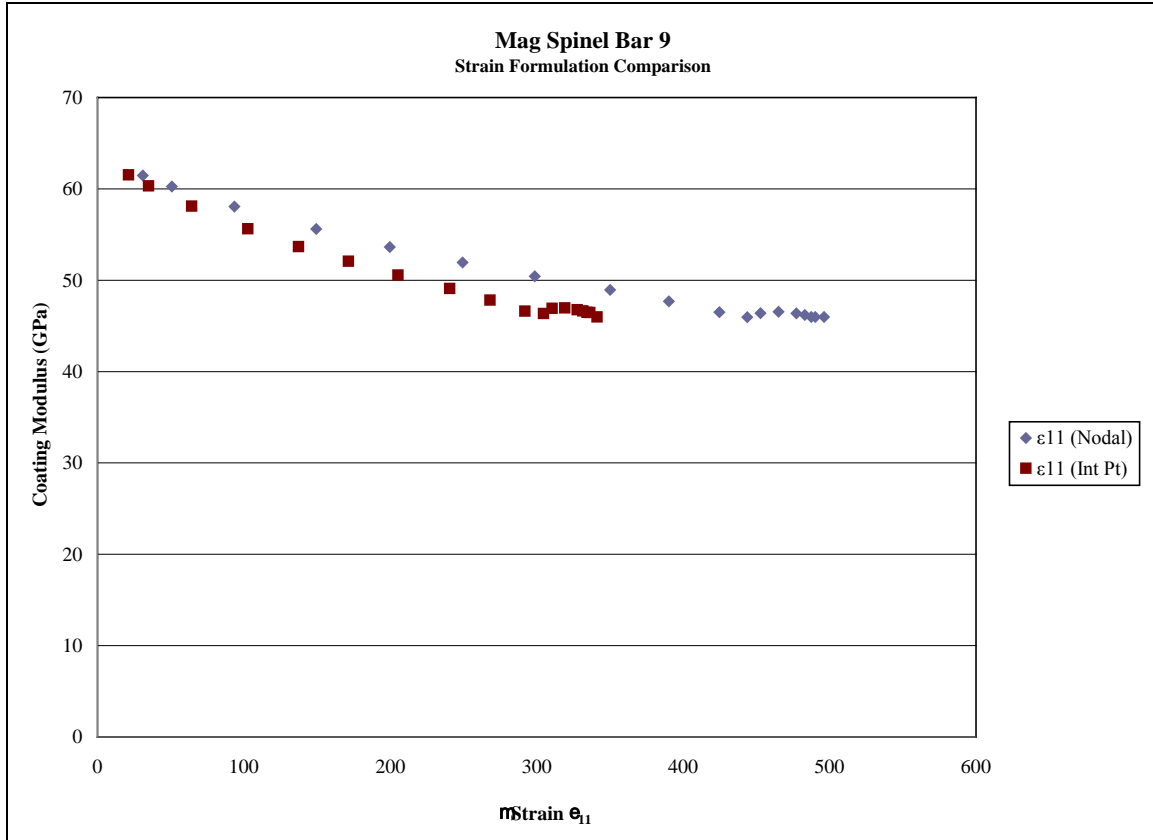
**Figure 55: Strain Calculation Effect on $E_c$**

Figure 55 shows an impact in the $E_c$ reported given the same data set from experimentation. It is clear that close attention must be made to the way that strain is calculated in the FEM. The results are sensitive to the extracted strain values. Table 14 lists the disparity in the values between the strains. The nodal strains include the strains of the coating while the strains calculated at the integration point more accurately reflect the localized strain at the interface experienced by the Ti-6Al-4V beam.

**Table 14: Formulated Strain Comparison**

| $E_c$ | μStrain $\varepsilon_{11}$ | STD DEV | % Difference |
|---|---|---|---|
| 61.5 | 26.06 | 4.83 | 9.26 |
| 60.3 | 42.80 | 7.93 | 9.26 |
| 58.1 | 78.93 | 14.62 | 9.26 |
| 55.6 | 126.02 | 23.34 | 9.26 |
| 53.7 | 168.47 | 31.20 | 9.26 |
| 52.1 | 210.31 | 38.95 | 9.26 |
| 50.6 | 251.87 | 46.64 | 9.26 |
| 49.1 | 295.20 | 54.66 | 9.26 |
| 47.8 | 329.07 | 60.93 | 9.26 |
| 46.6 | 358.25 | 66.33 | 9.26 |
| 46.4 | 373.85 | 69.22 | 9.26 |
| 46.9 | 381.13 | 70.57 | 9.26 |
| 47 | 391.76 | 72.54 | 9.26 |
| 46.8 | 402.09 | 74.45 | 9.26 |
| 46.6 | 406.86 | 75.33 | 9.26 |
| 46.5 | 410.36 | 75.98 | 9.26 |
| 46.5 | 412.72 | 76.42 | 9.26 |
| 46 | 418.71 | 77.53 | 9.26 |

## Constraints (Location & Effect)

This research assumed the modulus of the titanium beam to be the published value the

and the FEM was not "tuned" using experimental data.  Instead, the published value of

Ti-6AL-4V was used and the boundary conditions were changed in an attempt to quantify

the effects of the monofilament wires used as supports in the experiment.  This was done

by placing constraints near the eigenvector nodes to simulate the worst case situation.

The beam was constrained in the transverse direction but allowed to move freely in the

longitudinal direction.  The actual specimen was constrained in the experimental setup in

this manner.  Figure 56 shows approximately where the constraints were located.
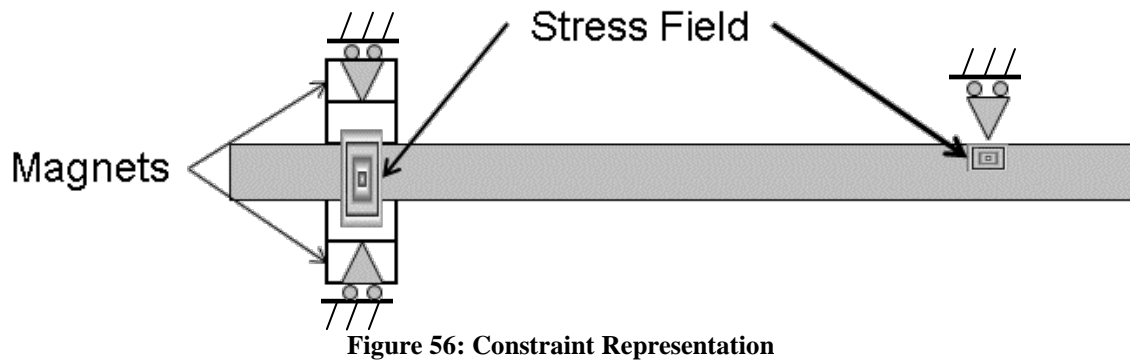


**Figure 56: Constraint Representation**

In addition, the constraints position was varied in order to examine the effects on the

natural frequency of the model.  The meshed nodes of the FEM were not exactly at the

location of the eigenvector nodes.  In the experiment, it is unlikely that the monofilament

wires, magnets, or the tube were perfectly located either.  Figure 58 illustrates this point.

Table 15 presents the results of moving the position of the constraints.  Figure 57 shows

how the positions were varied.  The tube designation refers to the node at the top of the

specimen while TM refers to the equivalent magnet blocks on one side of the specimen

with BM referring to the set of equivalent magnet blocks on the other side of the specimen. The locations are varied on either side of the bending mode nodes. The position was dictated by the location of mesh nodes in the FEM. It is seen that the frequency is slightly changed by moving the constraints. The worst case is defined as the highest frequency attained, in this case 203.51 Hz. This was the position chosen for the constraints when they were compared to the free-free case. This was done so that any effect could be easily seen. Figure 56 also shows a stress field. This is brought about by the constraints and is not present in the free-free case. This stress field means that there is more strain energy in the beam than there actually is in the experiment. This is because the monofilament wires would dissipate some of that energy through their movement which is not the case in this instance. This will result in a difference in the SER which will impact the loss factor results for the coating.

**Table 15: Constraint Locations**

| Case | Tube 1F | Tube 2F | Tube 1B | Tube 2B | TM 1F | TM 2F | TM 1B | TM 2B | BM 1F | BM 2F | BM 1B | BM 2B | FREQ (HZ) |
|---|---|---|---|---|---|---|---|---|---|---|---|---|---|
| | | | | | | | | | | | | | **BARE BEAM** |
| 1 | | | | | | | | | | | | | 203.08 |
| 2 | X | | | | X | | | | X | | | | 203.47 |
| 3 | X | | | | | X | | | | X | | | 203.45 |
| 4 | X | | | | | | X | | | | X | | 203.42 |
| 5 | X | | | | | | | X | | | | X | 203.31 |
| 6 | | X | | | X | | | | X | | | | 203.37 |
| 7 | | X | | | | X | | | | X | | | 203.36 |
| 8 | | X | | | | | X | | | | X | | 203.33 |
| 9 | | X | | | | | | X | | | | X | 203.23 |
| 10 | | | X | | X | | | | X | | | | **203.51** |
| 11 | | | X | | | X | | | | X | | | 203.5 |
| 12 | | | X | | | | X | | | | X | | 203.46 |
| 13 | | | X | | | | | X | | | | X | 203.35 |
| 14 | | | | X | X | | | | X | | | | **203.51** |
| 15 | | | | X | | X | | | | X | | | **203.51** |
| 16 | | | | X | | | X | | | | X | | 203.46 |
| 17 | | | | X | | | | X | | | | X | 203.34 |
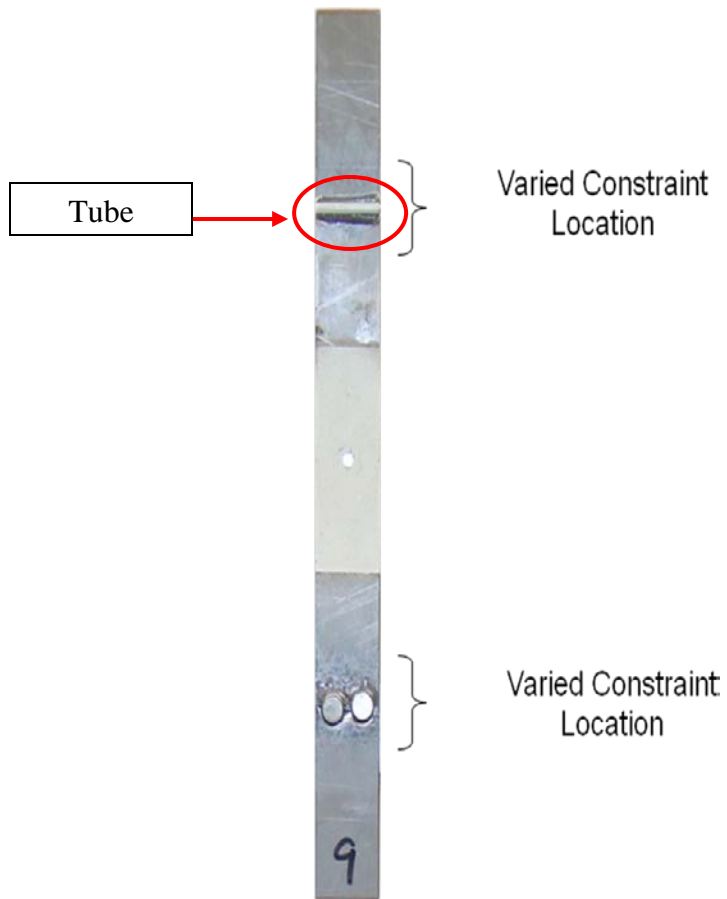
**Figure 57: Constraint Location**



**Figure 58: Constraint Variation Examples**

Figure 59 plots the results of using constraints. It is shown that the constraints increase the stiffness of the FEM.
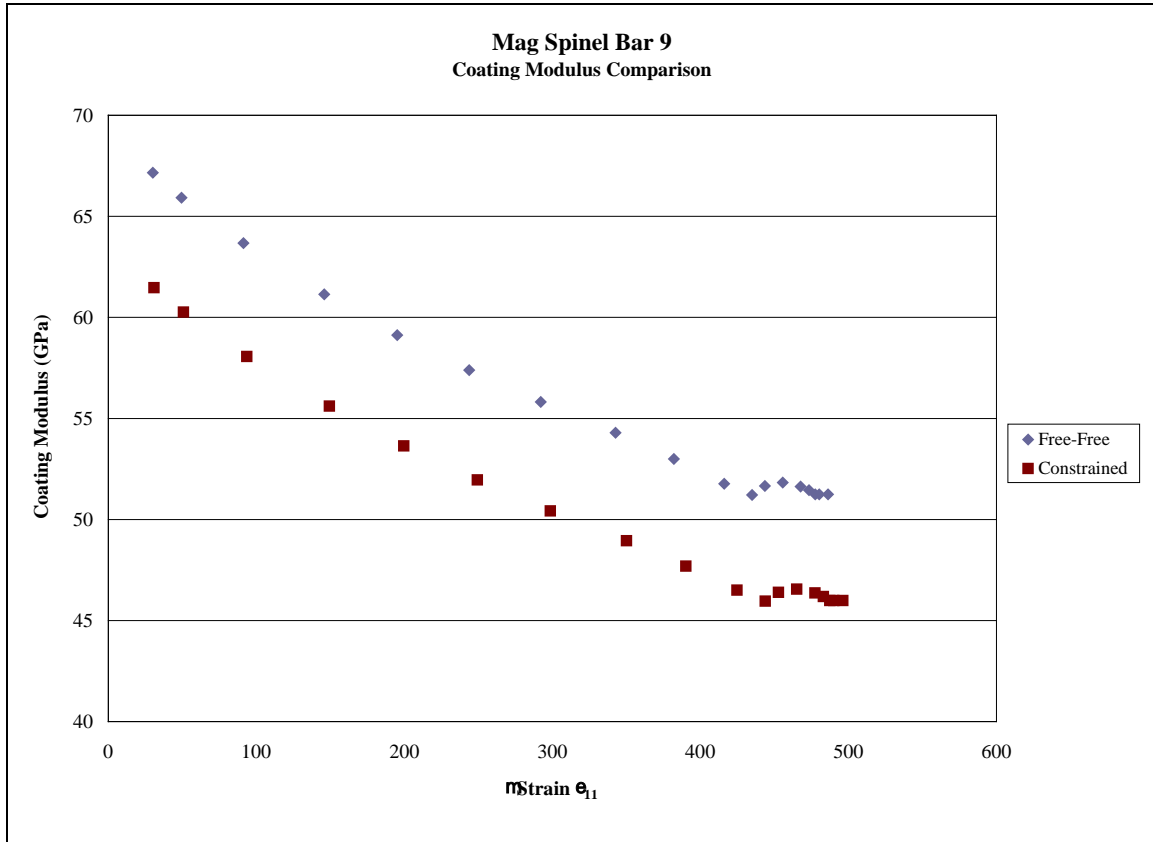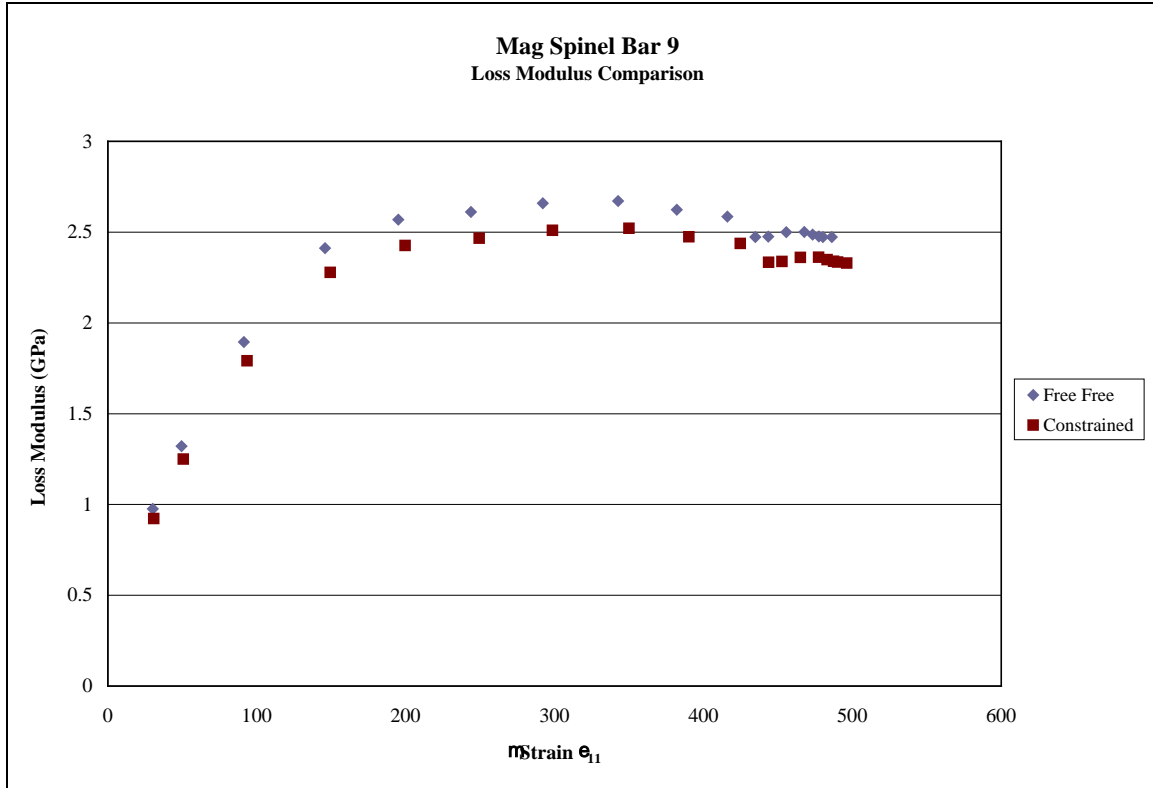


**Figure 59: Constrained vs. Free Free - $E_c$**

Figure 60 shows that the constraints do not affect the loss factor as much as the coating modulus. Since, constraints add stress to the FEM as compared to the free free model, the SER can be expected to decrease as the elastic strain energy of the system increases while the elastic strain energy of the coating remains constant. The SER is in the denominator of Equation 6, the loss factor should increase, and it does as shown in Figure 60.

89
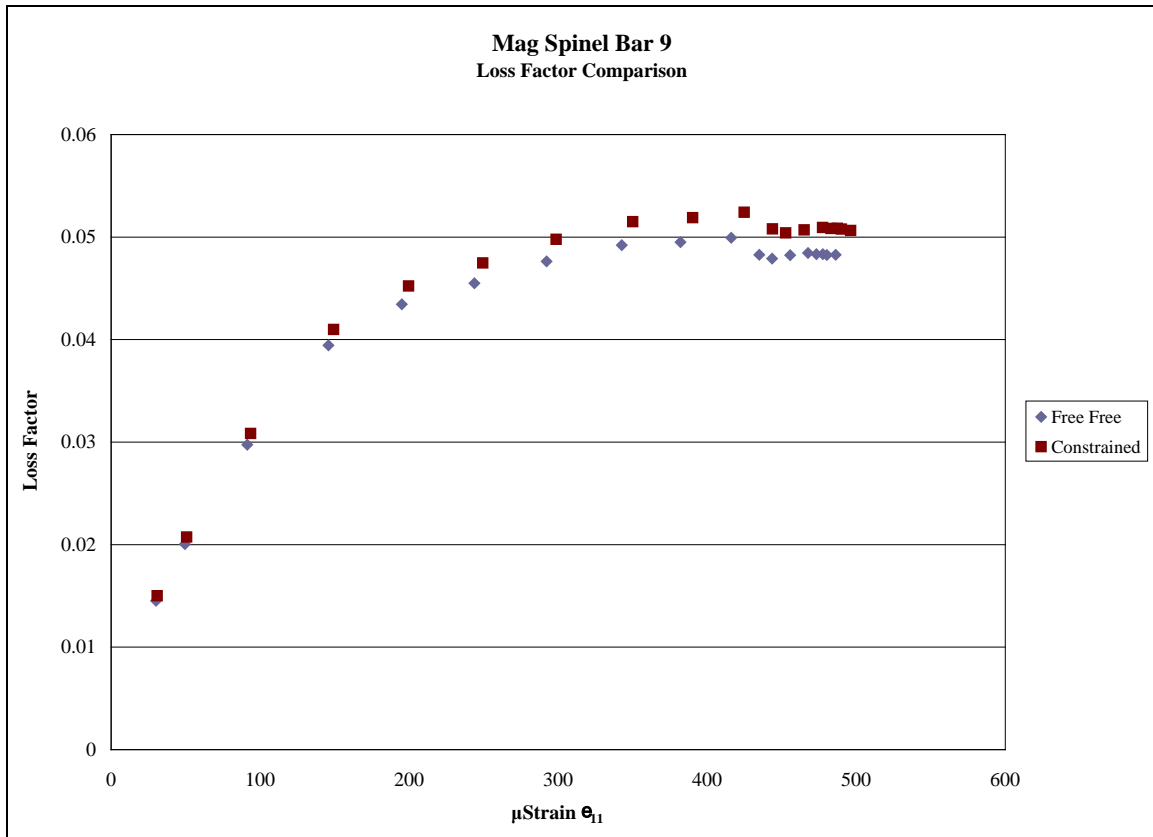
**Figure 60: Constrained vs. Free Free - $\eta_{coat}$**

Figure 61 does not show much of a difference between the constrained case and the free free case. The loss factor and coating modulus differences tend to cancel themselves out in this case.

**Figure 61: Constrained vs. Free Free - Loss Modulus**

## *Springs*

One of the goals of this study was to determine to what extent the monofilament wires

affected the approximation of the material properties for mag spinel.  In order to

accomplish this, the supports had to be simulated with finite element springs.  By using

springs to simulate the monofilament wires, the elastic strain energy in the system could

be better approximated than the use of constraints.  The springs would dissipate energy in

a much more realistic way.  The value of the spring stiffness was needed to successfully

model the monofilament wires with finite elements.  Unfortunately, there were no

measurements taken of the tension in the wires during the experiment so the wave

equation was used to approximate the frequency of the wires.

$$\omega_s = \frac{n\pi \sqrt{\frac{T_s}{\rho}}}{L}$$

(11)

n – Mode of interest
Ts – Tension in wire
ρ – density of wire
L – length of wire

Since the experiment was interested in the first bending mode, it was apparent that the

beam was restrained in two directions.  Figure 62 shows the concept of using springs in

two directions to approximate the supporting wires behavior.  The two directions shown

are the transverse and longitudinal direction.
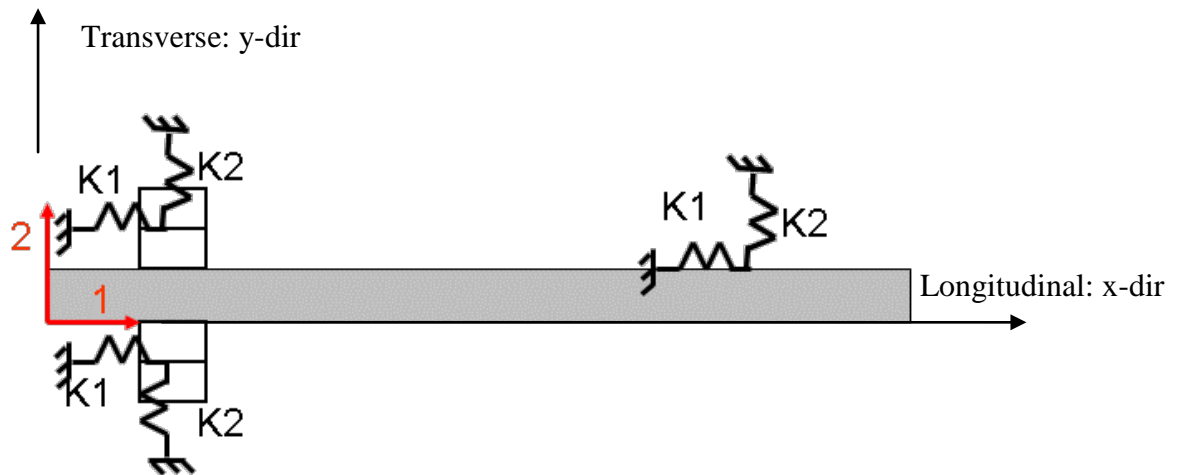


**Figure 62: Modeled Spring Location**

The longitudinal direction is also the direction that gravity acts in. As a result it is possible that the mass supported in the longitudinal direction is greater than the mass supported in the transverse direction. As a first approximation, the mass of the specimen was divided by three to simulate each monofilament wire supporting one third of the mass. This assumption resulted in different values assigned to density ($\rho$) in Equation 12. In addition, the monofilament wires were stretched which increased the tension in the monofilament wires far greater than the tension due to gravity. This was reflected in the wave equation by assigning different tensions due to the direction of loading. The tension in the longitudinal direction was approximated by Equation 12 below, while the tension in the transverse direction was approximated by the Equation marked as K2.

$$T_s = \frac{Mg}{2\sin\theta} \left.\right\} \text{K1} \tag{12}$$

$$
\begin{aligned}
T_s &= \sigma A \\
\sigma &= E\varepsilon \\
\varepsilon &= \frac{\Delta L}{L} \\
\Delta L &= \pi d \\
d &= \text{screw diameter} \\
L &= \text{Length of Line}
\end{aligned}
\left.\right\} \text{K2}
$$

K2

$\rho$- based on line density of

Monofilament Line
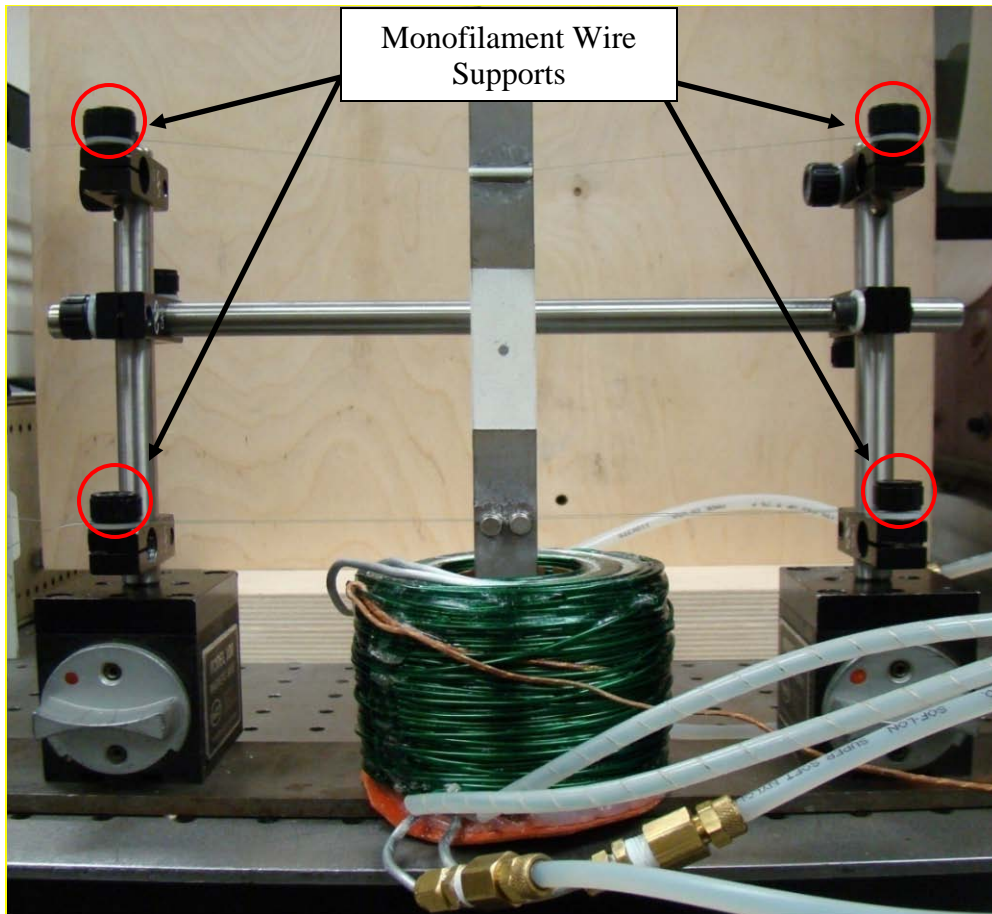
**Figure 63: Monofilament Wire Supports**

Assuming a tension that results in a frequency of approximately 3000Hz for the wires in

the transverse direction seemed reasonable and a good first approximation.  In addition, a

frequency of 22.5 Hz was calculated for the wires in the longitudinal direction.  Although

this is an approximation on the behavior of the monofilament wires, the FEM provided a

means of iterating to instill a measure of confidence in the results.

ODB: Springs_Case_8.odb   Abaqus/Standard Version 6.8-2   Wed Jan 14 08:44:29 Eastern Standard Time 2009

Step: Step-1
Mode        2: Value =  4.52012E+06 Freq =  338.37   (cycles/time)
Deformed Var: U   Deformation Scale Factor: +2.032e+01
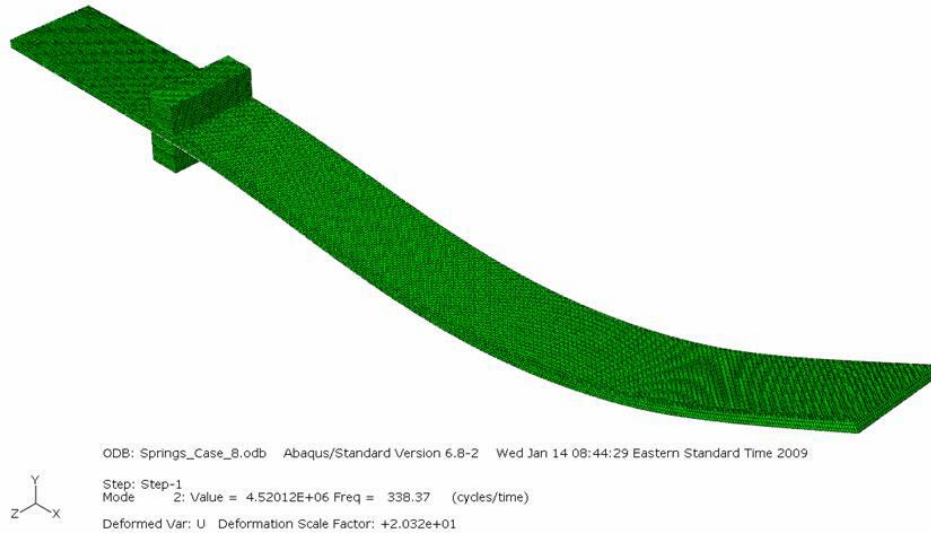
**Figure 64: FEM Rigid Body Mode**

As the tension in the longitudinal direction is increased, the FEM shows an increase in the frequency of the first bending mode as shown in Table 16 (Case 8).  This could result from the monofilament wire impinging on the magnet coil.  This mode is shown in Figure 64.  The elastic strain energy, as calculated by FEA, of this mode was on the same order of magnitude as the first bending mode.  This was not observed in the experiment and would lead to erroneous velocity measurements.

**Table 16: Spring Stiffness Results**

| CASE | K1 | K2 | 1st Bending Mode | ω1 | ω2 |
|------|------|------|------|------|------|
| 8 | 1.36E+06 | 1.36E+04 | 338.37 | 1000 Hz | 100 Hz |
| USED | 2.29E+02 | 1.38E+04 | 204.08 Hz | 22.5 Hz | 3000 Hz |

Figure 65 plots the coating modulus calculated with the springs as well as the coating estimated earlier with a free free beam.  The results are similar to those found with the constraints included.  Since the springs were in the same location as the constraints, the results show a similar stiffening of the model.

95
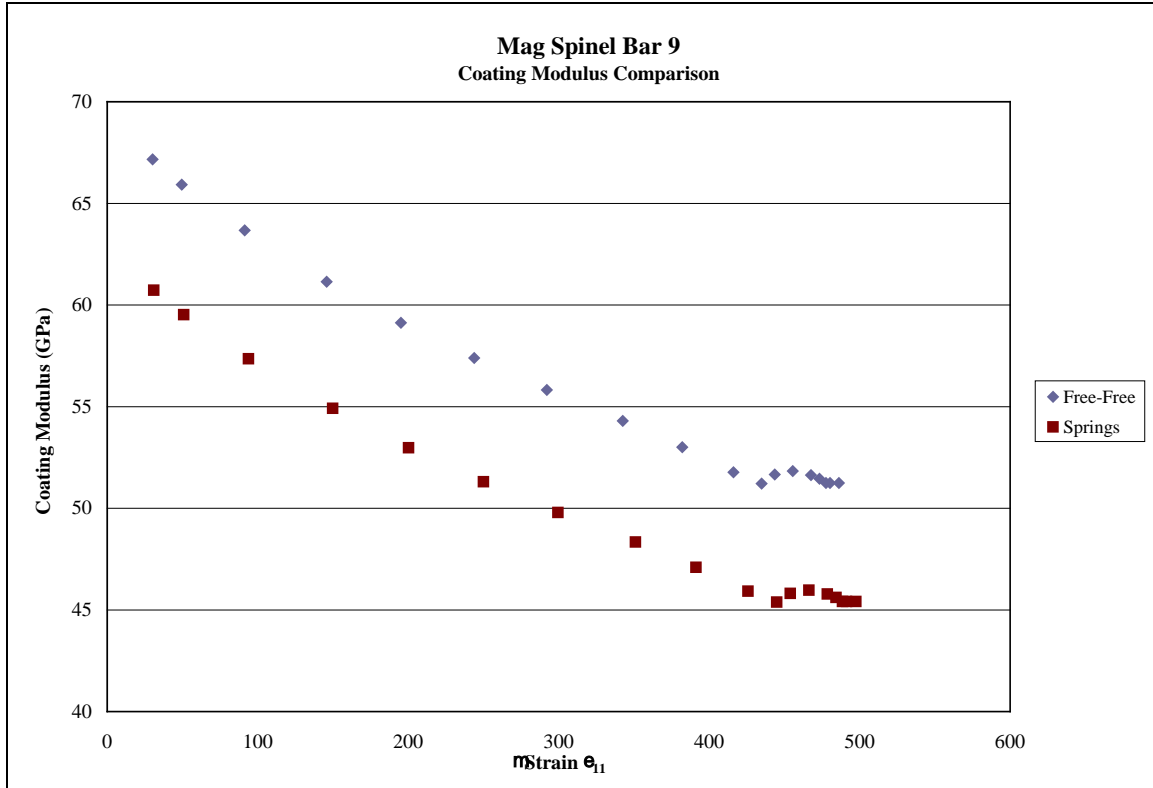
**Figure 65: Springs vs. Free Free - E$_c$**

Figure 66 shows that including springs does not change the loss factor by very much. This tells us that the monofilament wires did not have much effect on the estimation of the loss factor with this experimental setup. The values are very similar to the constraint model which means that there is an increase in elastic strain energy in the beam as a result of the springs. This is in the transverse direction since the springs are much stiffer in that direction. The springs are not as stiff in the longitudinal direction so overall the model acts similar to the constraints which allowed free movement in the longitudinal direction.
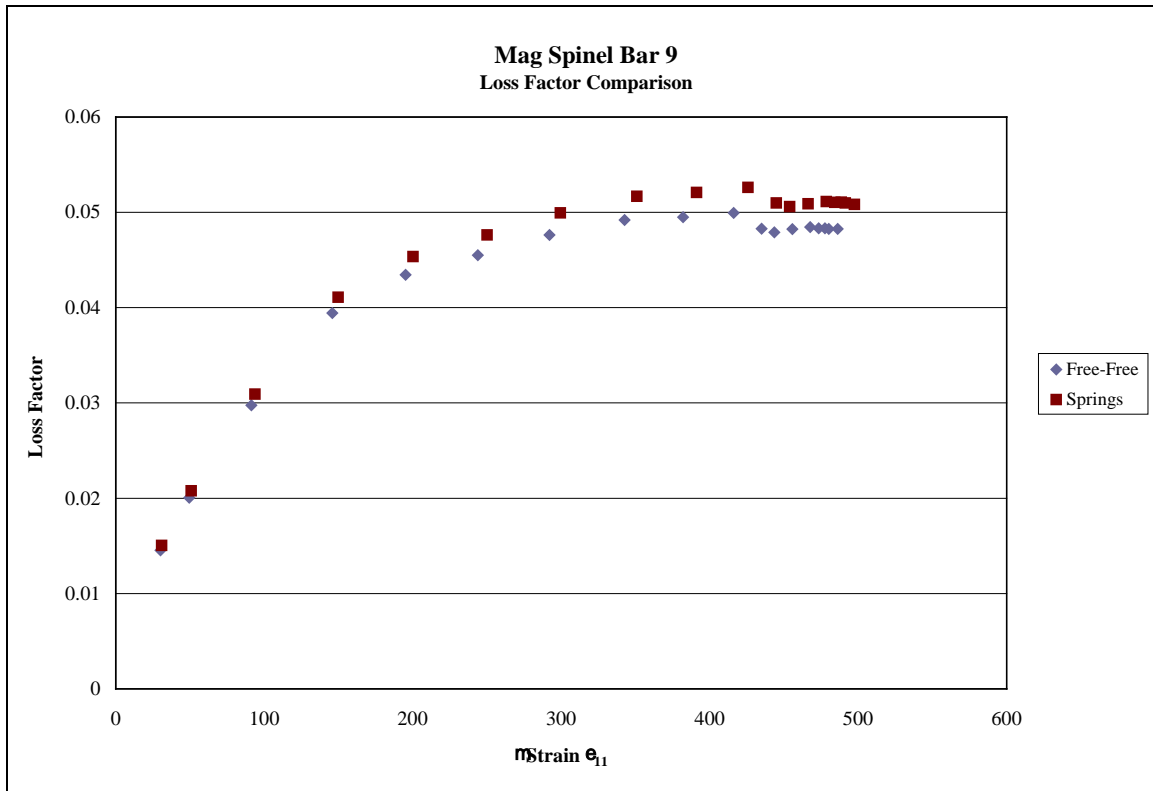
**Figure 66: Springs vs. Free Free - $\eta_{coat}$**

Figure 68 shows that the difference in coating modulus superseded the loss factor difference.
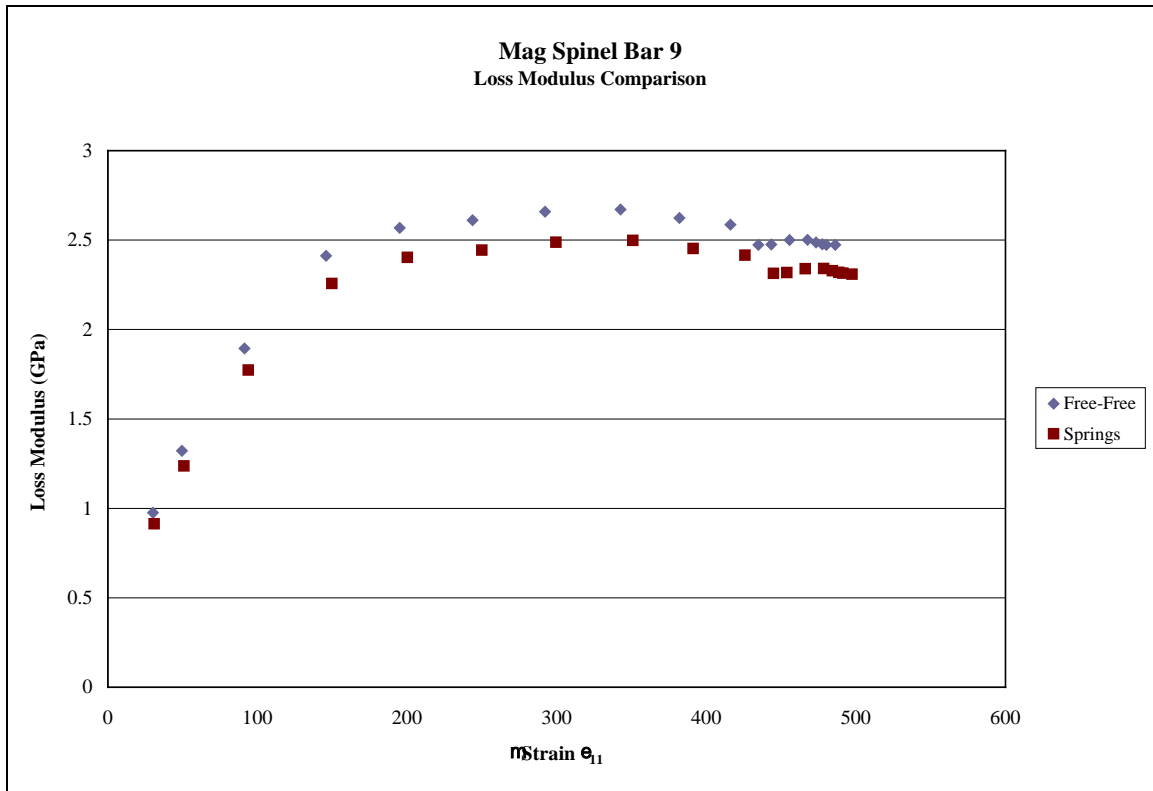
**Figure 67: Springs vs. Free Free - Loss Modulus**

We now compare the FEM with springs to the FEM that approximates the one used by

Pearson (2008) in his research. Figure 68 shows very good correlation with regard to the

coating modulus obtained from both models. This means that the adjustment of the bare

beam modulus does compensate for the monofilament wires in the model.
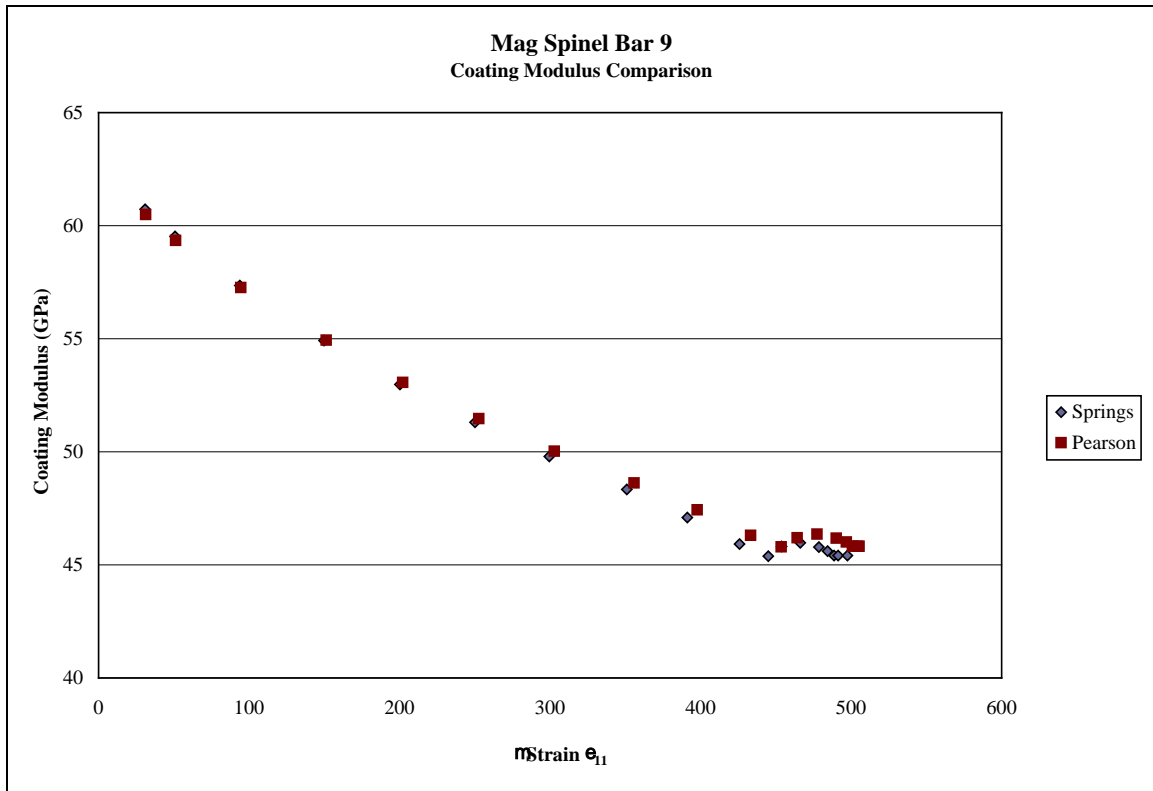
**Figure 68: Springs vs. Pearson results - $E_c$**

Figure 69 shows that the stiffer FEM used b Pearson is not fully compensated for by the

bare beam modulus adjustment. However, the discrepancy is less than when comparing

Pearson's results to the free free model.
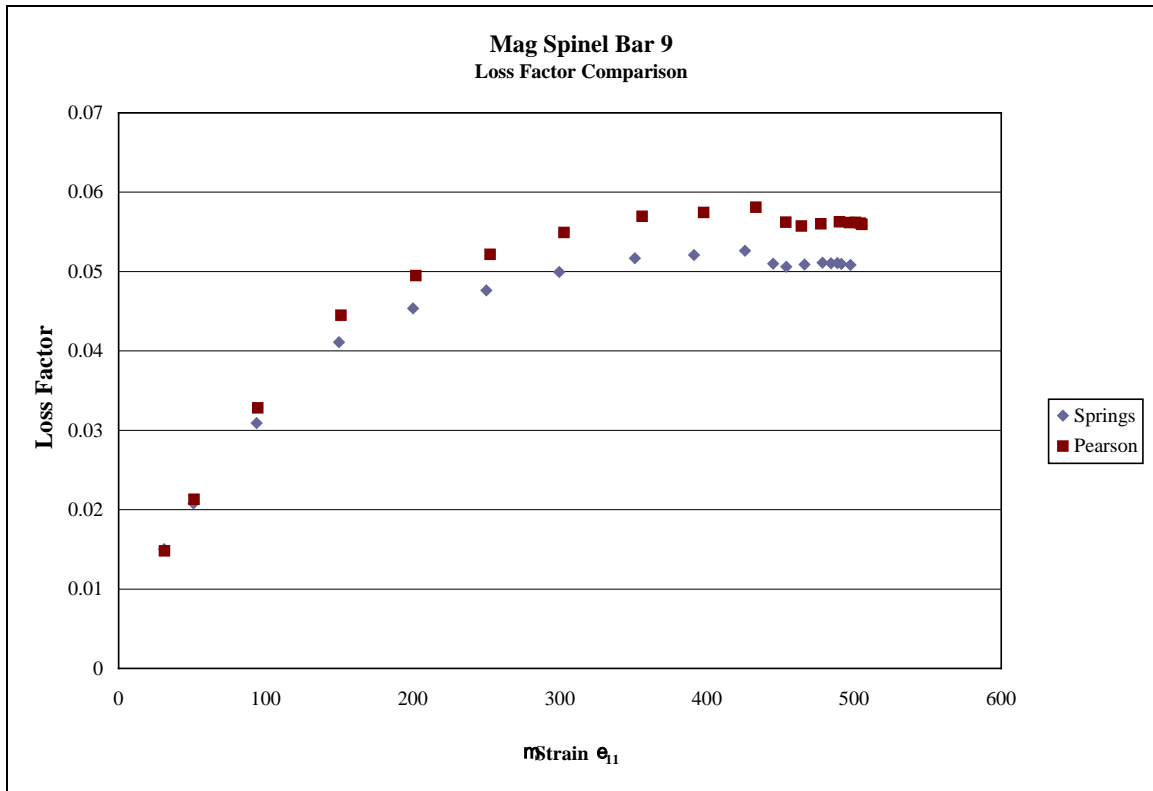
**Figure 69: Springs vs. Pearson results - $\eta_{coat}$**

Figure 70 shows a similar pattern to the previous figure. Since, the coating modulus are so closely correlated, the loss factor difference dominates the loss modulus results.
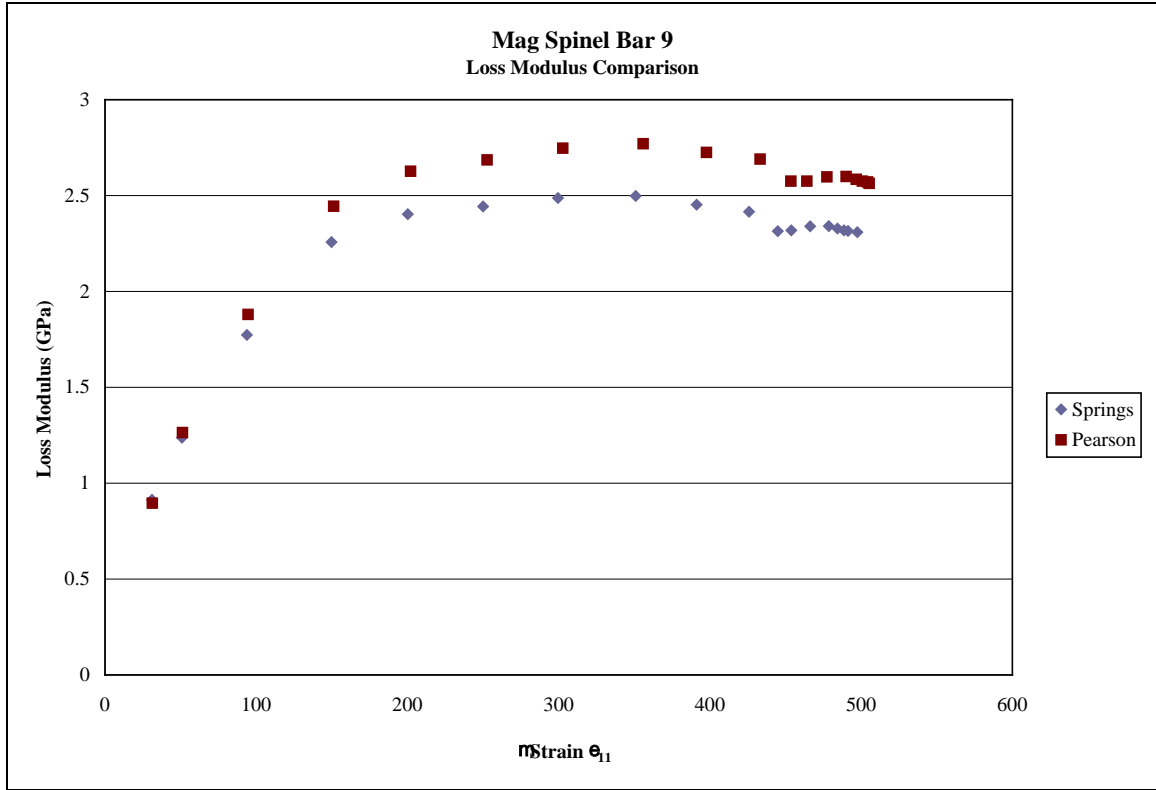
**Figure 70: Springs vs. Pearson results - Loss Modulus**

## *Strain along Coating*

The strain along the length of the coating, in the center of the specimen was examined in order to investigate any impacts to the experimental results that could occur as a result of the choice of the coating patch size.  The coating patch should be smaller in order to decrease the slope of the curve to reduce any strain difference along the measured length. This is also dependent on the spray pattern technology used to apply the coating of course.

101

**Figure 71: Strain along length of coating at coating beam interface in the center of the beam**

# V.  Frequency Response Function Comparison

## *Objective*

Over 500 FEM runs were done in the analysis in the previous chapters.  Several dozen more were done in support of this Chapter alone.  This Chapter deals with the concept of developing a FRF using discrete time integration.  The material properties of mag spinel were estimated in previous research with the understanding that they are non-linear (Reed 2007).  The techniques used are based on linear assumptions.  These linear assumptions included using a FEM that defined material properties as linear elastic in the eigenvalue eigenvector considerations.  By verifying whether a point on the experimental FRF could be duplicated by FE discrete time integration, it was felt that a study of this nature could validate the apparent linear parameters used in the phenomenological study carried out in the previous chapters of this thesis.  In order to accomplish this, several additional steps were required.  The author will state these steps and then present results that address each in turn.  Three areas are covered, each with subsections.  First part will discuss the development of how the discrete integration works in representing the FRF.  Next is how to arrive at the amplitude of the forcing function and why the bare beam data was used.  Finally, how the point on a physical FRF is found with this technique.

## Finite Element Modeling

The first step in any time integration approach is related to the order of accuracy. The FEM developed earlier in this work was suitable from a convergence point of view. However, using the FEM developed for the material parameter evaluation proved to be so time intensive, due to the number of degrees of freedom, that a more modest model was necessary for this final investigation. The time integration size was initially studied. This required an investigation of the bare beam's frequency brought about by a load placed on the structure as shown in Figure 72. The FEM shown consisted of approximately 7000 nodes. The model is supported with the constraints discussed in the previous Chapter. These provided the supports necessary in order to load the beam. In order to load the beam, a forcing function must be calculated. In the experiment a magnet coil provides a force through permanent magnets into the specimen. There is a voltage associated with each test condition, but the force itself is not characterized. Equation 13 is the force that will be input as the forcing function.

$$F = A\sin\left(\omega * t\right) \tag{13}$$

Once an 'A' is selected, a frequency is chosen and the FEM is run as a Dynamic, Implicit step in ABAQUS STD. The STD refers to an implicit, as opposed to an explicit, solution. The FEM is allowed to run for a set time period with discrete time integration steps. Once the solution reaches steady state, the input frequency and output velocity can be plotted and this corresponds to one point on the experimental FRF.

Reaching steady state was required, since we need to determine the FRF for a given loading frequency. The bare beam is used since the experiment provided the value of the natural frequency, approximately 203 Hz. The bare beam response is linear and lightly damped allowing us to plot voltage versus velocity. With this curve, a given steady state velocity can be correlated to an experimental voltage. This steady state velocity is obtained by applying the forcing function at the bare beam natural frequency of 203 Hz since the various voltages tested all result in the same natural frequency. This provides the coefficient of the forcing function 'A' in Equation 13. Once this coefficient is found it can be applied to the coated FEM at a tested frequency to make a comparison to experimental data. This assumes that the 'A' in the forcing function of the experiment used for the bare beam is the same 'A' used for testing the coated specimen.
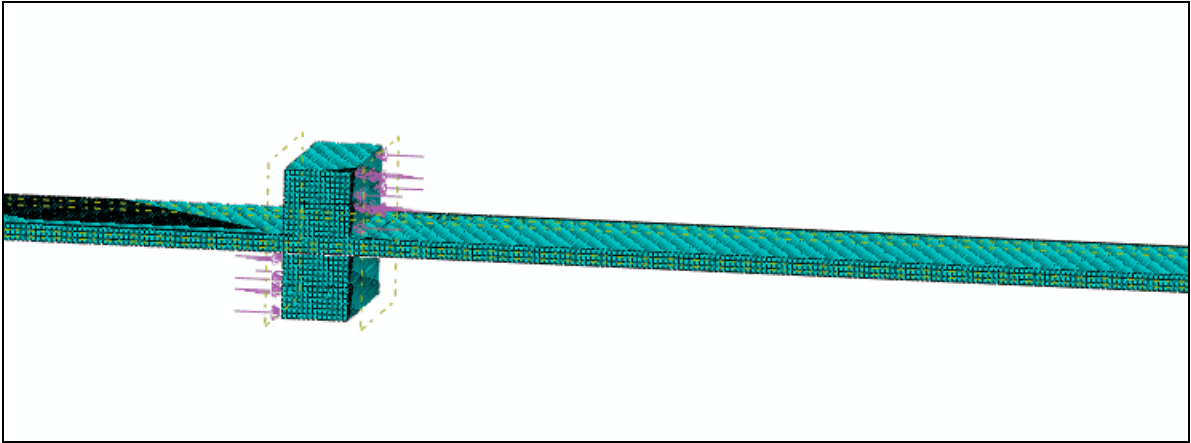


**Figure 72: 3D FEM w/Pressure Load on Magnet Surface**

## *Rayleigh Damping*

The FEM used previously to examine various parameters was needed to extract values. These values resulted from an eigenvalue solution. As such, no damping was included in this analysis. This was important since the damping of the coating was one of the material properties being investigated. We were able to estimate that property using the half-power bandwidth method in conjunction with the elastic strain energy computed by the FEM. In order to simulate the forced response, some damping must be included. Without damping, the FEM response to an imposed harmonic load at resonant frequency would not reach steady state but would continue to grow without bound due to the linear elastic material properties used to describe the beam, magnets, and coating materials.

The type of damping exhibited by mag spinel is not viscoelastic. However, this is the type of damping that can be modeled in ABAQUS. This approximation is along the same lines as the previous approximations. In order to calculate the coefficients of Rayleigh damping, experimental data along with previous FEM output is used. Equation 14 is from Cook et al (2002). The $\beta$ term was found to be orders of magnitude lower than the $\alpha$ term and so was not utilized. The bare beam loss factor ($\eta_{bare\ beam}$) used was 0.0004 and the resulting $\alpha$ was 0.51. An $\alpha$ of 7.81 was found using the same approach, with the exception of the coating loss factor and frequency chosen. With the bare beam these values were the same regardless of voltage since we have a linear response. However, as seen previously these values were different at each voltage for the coated specimens. The

lowest voltage that was investigated with a coated specimen was 50mV. The

corresponding values for loss factor and frequency were used in this research.

$$\eta_{barebeam} = \alpha * (f_1 * 2\pi) + \beta * (f_2 * 2\pi)$$ **(14)**

## *3D Brick Results*

The number of degrees of freedom included in the 3D brick FEM, resulted in long run

times. This FEM was used in an attempt to determine the best choice for a time

integration increment. A time step of 0.001 seconds was too large and gave the results

shown in Figure 73. The power spectrum density (PSD) was calculated and is shown in

Figure 74. It shows that a frequency of approximately 180 Hz is part of the response

displayed in Figure 73. This frequency was not observed in the experiment and as we

decrease the time increment size it disappears. The time increment size of 1E-5 seconds

was chosen through iteration. It provided stable results without the spurious shown

previously.
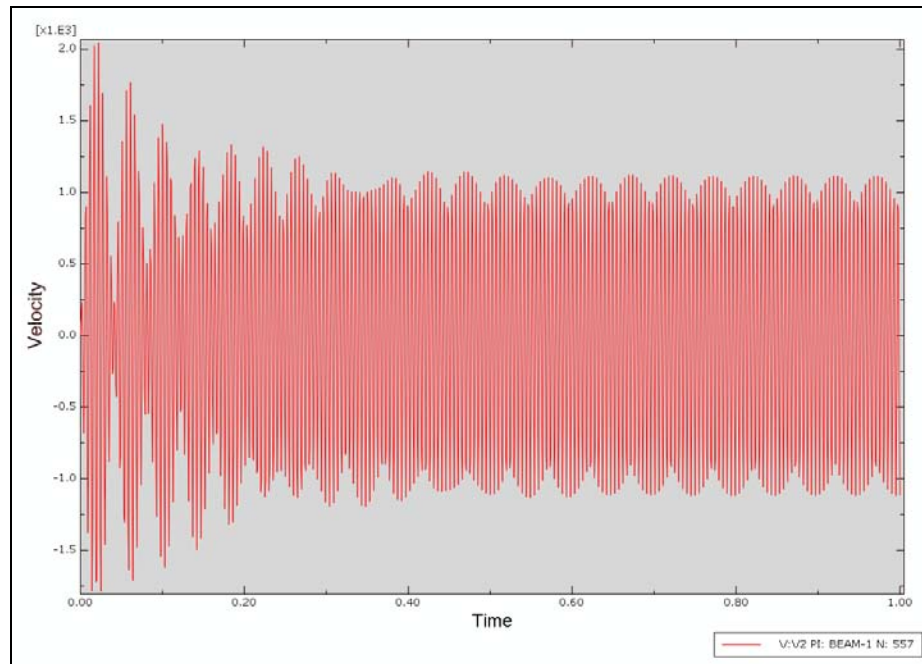
**Figure 73: Bare Beam - time step = 0.001**
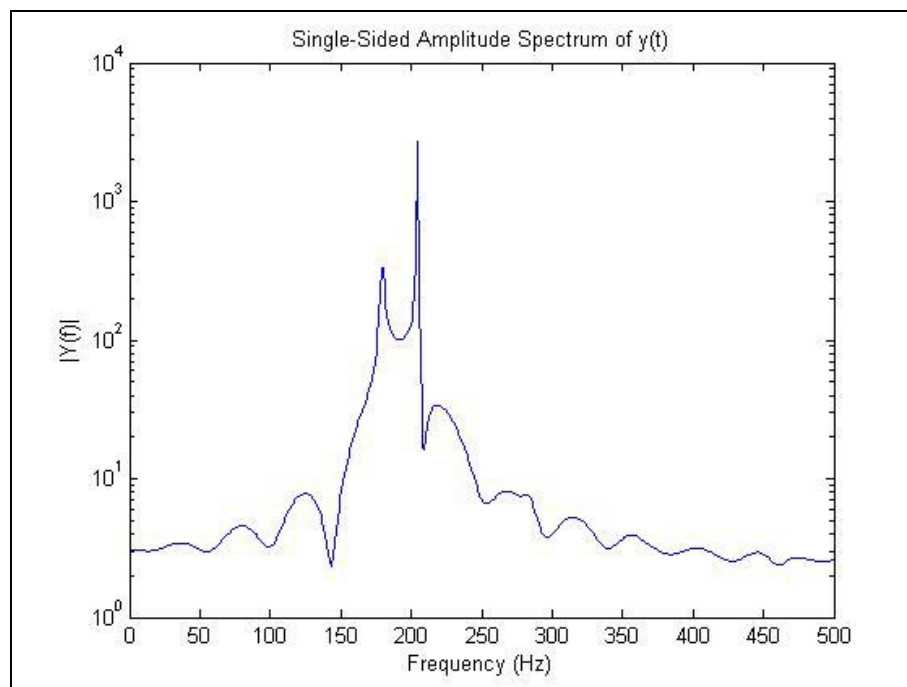


**Figure 74: Bare Beam - time step = 0.001 PSD**

### *Wire Finite Element Model*

The FEM used previously in this research utilized 3D brick elements as described. The strains, elastic strain energy, frequency, and displacement were extracted from this model. In this portion of the research a much simpler model was required due to the time required to reach steady state at the required time step size. The only value of interest is the velocity at the center of the specimen as the FEM reaches a steady state. Timoshenko beam elements were employed in order to reduce computational time. It was found that 1000 elements could successfully replicate the frequencies seen in experiment for the bare beam and the coated specimen. This FEM, while much smaller than the 3D brick model, was also impractical from a time perspective. A smaller number of wire elements in another FEM were used with the purpose of ensuring that the frequency of 203 Hz was still matched. The end result of this study was that a FEM made of 100 wire elements continued to output a frequency of approximately 203 Hz. The bare beam model is shown in Figure 75 and the coated beam in Figure 76.
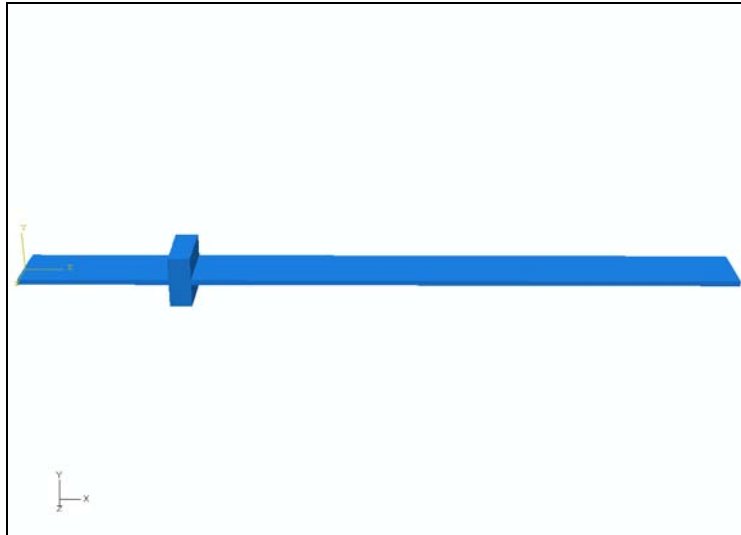
**Figure 75: Bare Beam - Wire Model**
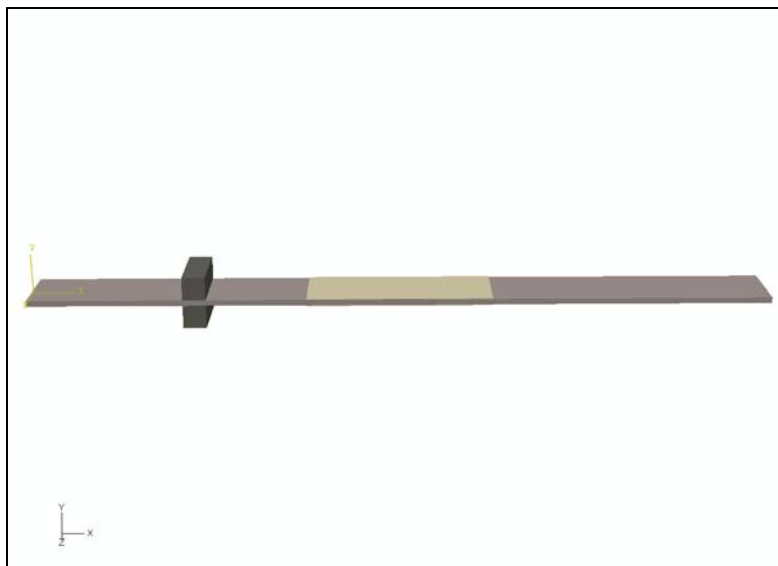


**Figure 76: Coated Beam - Wire Model**

## Forcing Amplitude Characterization

The FEM has now been settled on. It is now necessary to correlate the forcing function to the voltages used in the experiment. Figure 77 is a plot of the bare beam max velocity versus voltage. At each voltage tested there was a natural frequency and maximum velocity associated with it. As stated earlier, the natural frequency of the bare beam was experimentally determined to be approximately 203 Hz. The wire FEM used also produced a natural frequency of 203 Hz. We see that the relationship between maximum velocity and voltage is linear at lower voltages with only slight variations at the higher voltages. This is expected due to the linear behavior of the bare beam to include lightly damped. With this curve we can correlate the steady state velocity output of the FEM @ L/2. For instance, if the magnitude of a forcing function 'A' and the natural frequency (203 Hz) are input into the bare beam FEM, and the result at the steady state response is 142 mm/sec @ L/2, then from the curve it is apparent that the 'A' chosen correlates to the 10mV bare beam experiment.
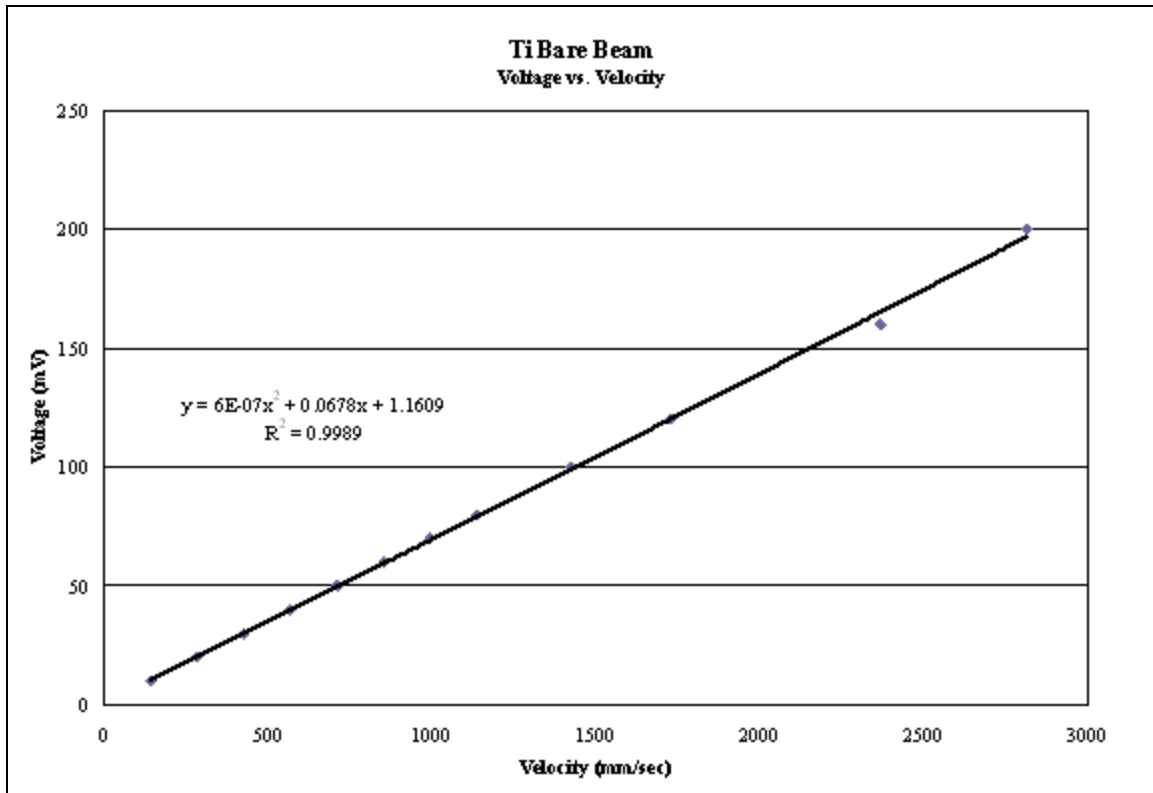
**Figure 77: Bare Beam - Velocity vs. Voltage**

Now this 'A' can be used as the magnitude of the forcing function for the coated

specimen FEM. The frequency chosen in this case is not the natural frequency but rather

a frequency separated from the natural frequency by a few Hz. This was done to clearly

differentiate the response from the natural frequency. Once steady state is reached in this

case, the resulting velocity can be plotted on the experimental FRF since we chose the

frequency of the forcing function. The bare beam response is important because it is a

linear system and as long as the forcing function is at the natural frequency there should

be a correlation with the voltages i.e. curves seen in the experiment. This method is

predicated on the assumption that the magnitude of the forcing function used in the

experiment for the bare beam was the same magnitude of the forcing function used for

the coated beam. For instance, one of the tests of the bare beam was at 50mV. The

coated beam was also tested at 50 mV. It is assumed that these values are correlated by

the magnitude of the forcing function produced by the magnet coil and are not dependent

on the specimen response. This method requires the bare beam FEM achieve a steady

state solution.

Figure 78 is the result obtained during this research and shows that the Wire FEM did not

reach steady state after two seconds. This FEM took numerous hours to complete and a

follow-up run with a longer time span could be done. However, there is a question of just

how long it would take to achieve steady state. The results in Figure 78 suggest that it

could be a relatively long time for steady state to occur. Another method for finding 'A'

and the voltage applies was developed and it is the one that was used in this research and

described below.
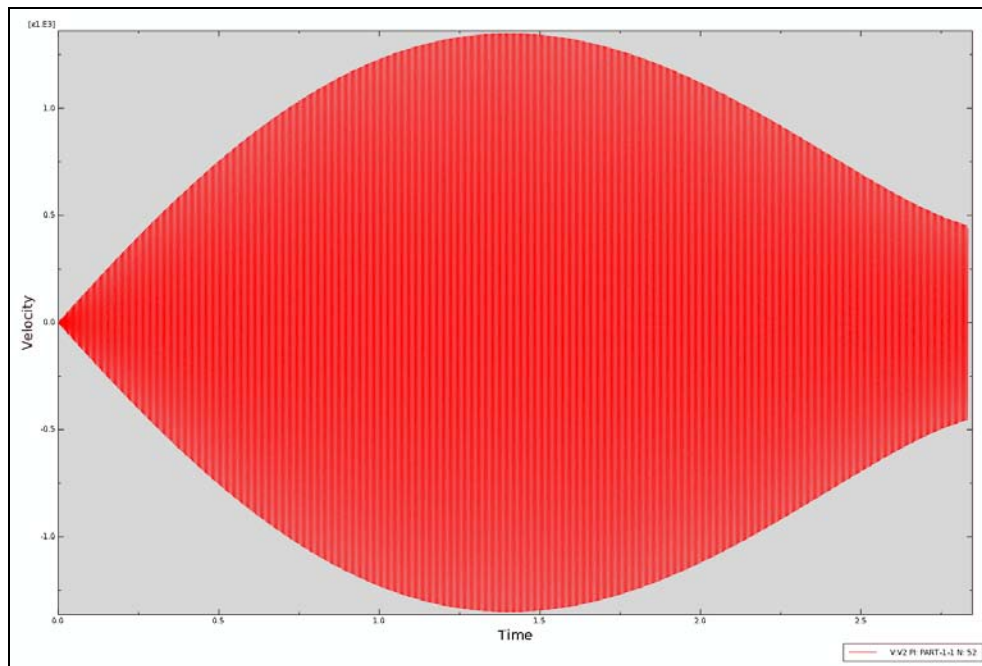


**Figure 78: Bare Beam response to forcing function @ 2.8 seconds**

This method makes use of the point velocity-displacement function that has been

incorporated through this thesis and is shown in Equation 15.

$$\delta = \frac{V}{f_n * 2 * \pi} \tag{15}$$

In this method, we rederive Equation 15 as shown in Equations 16 – 19 with the added

step of differentiating in order to obtain acceleration as a periodic function.

.

$$s = C \sin(\omega t) \tag{16}$$

$$\frac{\partial s}{\partial t} = V = \omega C \cos(\omega t) \tag{17}$$

$$\frac{\partial^2 s}{\partial t^2} = a = -\omega^2 C \sin(\omega t) \tag{18}$$

$$\delta = \frac{V}{\omega} = \frac{a}{\omega^2} \tag{19}$$

Equation 20 shows that we can take the point velocity and multiply by the

frequency. This gives the point acceleration.

$$a = \delta * \omega^2 = V * \omega \tag{20}$$

The acceleration can be incorporated in evaluating the effective force (not the real force

at the magnets but the effective force to be used in determining the voltage input). The

acceleration we calculated is only for that point in which Equation 19 holds. This leads

to a force which is not the real forcing function but a force used to evaluate the voltage

114

related to the velocity of the bare beam @ L/2.  This is not the force at the magnets.  It should only be used to evaluate the voltage.  Since the force caused by the voltage is felt by the entire specimen, this is a reasonable approximation.  Equation 21 shows the amplitude of velocity

$$F = ma = A\sin(\omega t) \tag{21}$$

If this velocity is multiplied by the frequency and then the total mass of the specimen as shown in Equation 22, we have in effect the point force.

$$F = V * \omega * m = A\sin(\omega t) \tag{22}$$

We can now plug values into Equation 23 for a specific voltage that the bare beam was tested at.

$$A = \frac{V * \omega * m}{\sin(\omega t)} \tag{23}$$

## *Results*

Once we have correlated an 'A' value to a voltage, we can compare the FEM coated beam output to the extrapolated output for the comparable voltage.  In this case we have chosen 10 mV as the voltage used to test the bare beam.  At 10 mV we have a maximum velocity of approximately 142 mm/sec at the natural frequency of approximately 203.8 Hz.  By realizing that the maximum deflection occurs at π/2, we can find 'A'(π/2).  The

mass of the bare beam specimen with magnets attached is a measured quantity and is approximately 34.4 grams.  Placing these values into Equation 23 produces a value of 6.24 N.  This force equates to a moment of  0.35 N m.  Since we used the experimental values from the 10 mV test case, we now have the appropriate 'A' for this voltage. Now that we have an appropriate voltage for the bare beam, we need to approximate the behavior of the coated specimen at that voltage.  The lowest voltage tested during the experiment was 50 mV.  Figure 79 is constructed using experimental data of 18 voltages tested with a beam partially coated with mag spinel as discussed previously.  At lower voltages, the specimen was tested to higher frequencies.  By taking experimental points of a coated specimen at 230 Hz and then applying a polynomial fit, an approximate response can be estimated at 230 Hz for the calculated 10 mV case.  This is shown in Figure 79 and Figure 80.  Using the polynomial obtained with the method just described, results in a value of 5.9 mm/sec for the 10 mV coated specimen case.  This is one point on the 10 mV FRF curve.
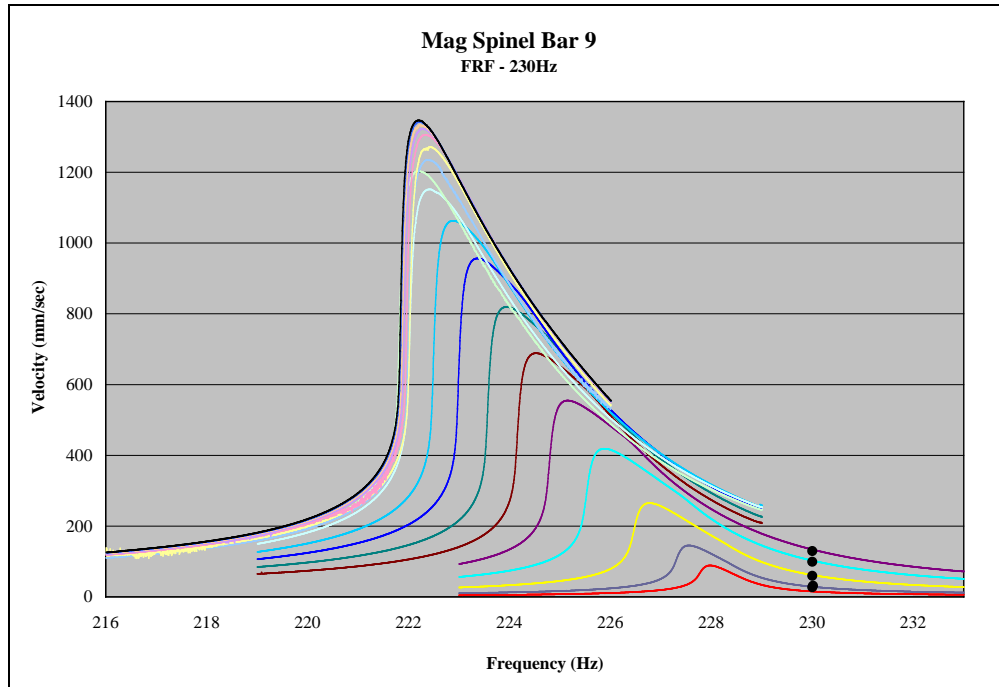
**Figure 79: Voltage - Velocity Correlation @ 230Hz**
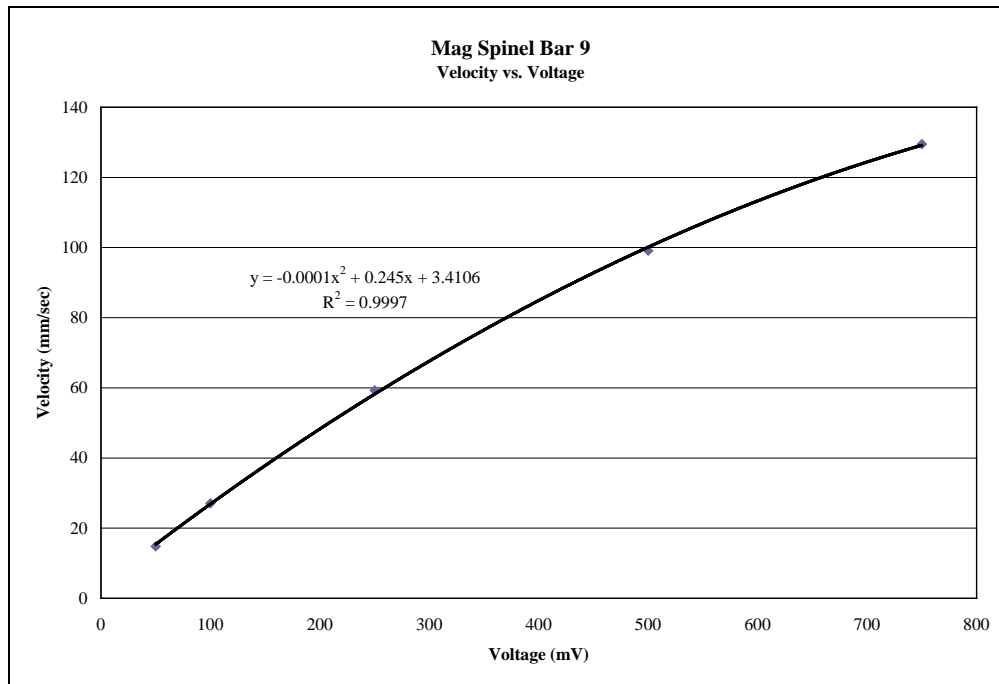


**Figure 80: Coated Beam - Velocity vs. Voltage**

117

We can obtain another point by repeating this process at a different frequency. If we use 229 Hz as opposed to 230 Hz we have another point on the calculated 10 mV curve. One more point can be obtained by using the backbone curve described in Chapter III. It is shown again in Figure 81. The polynomial obtained is used to calculate the maximum velocity theoretically attained by testing the coated specimen at 10 mV. With these three points a polynomial fit can be added to graphically portray the theoretical response of a coated specimen to a 10 mV test. This is shown in Figure 82.
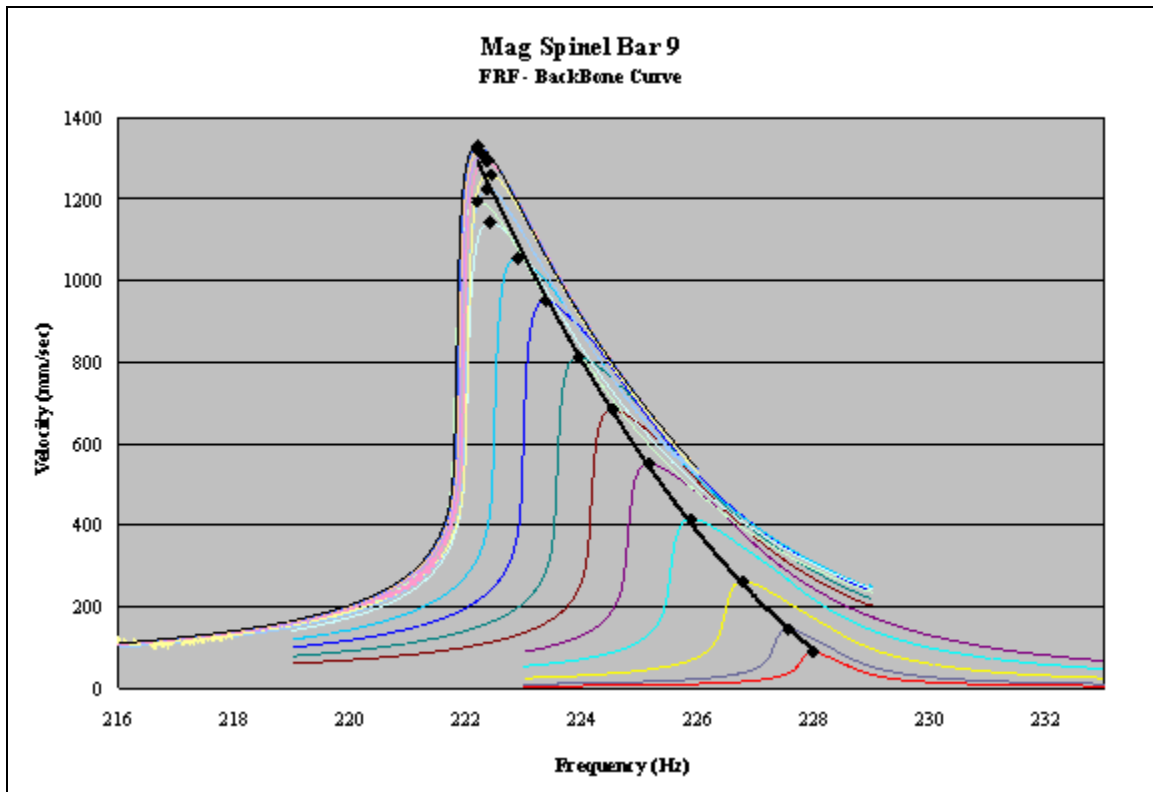


**Figure 81: Backbone Curve of Experimental FRF**
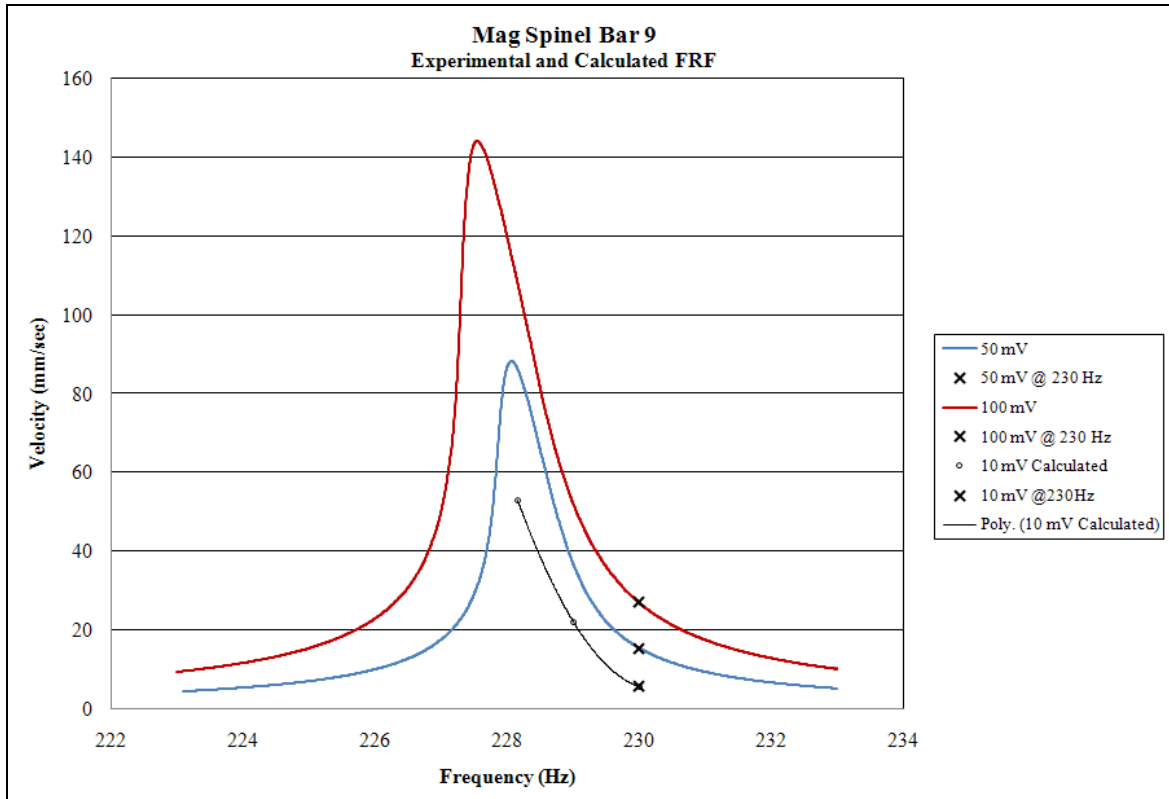
**Figure 82: Experimental and Calculated FRF**

The coated FEM with a moment magnitude ('A') of 2.02 N m has the response depicted

in Figure 83.  It is approaching steady state but not enough time was available for it to

reach steady state conclusively.  Figure 84 shows the frequency of the forcing function of

230 Hz and the natural frequency of approximately 227 Hz.
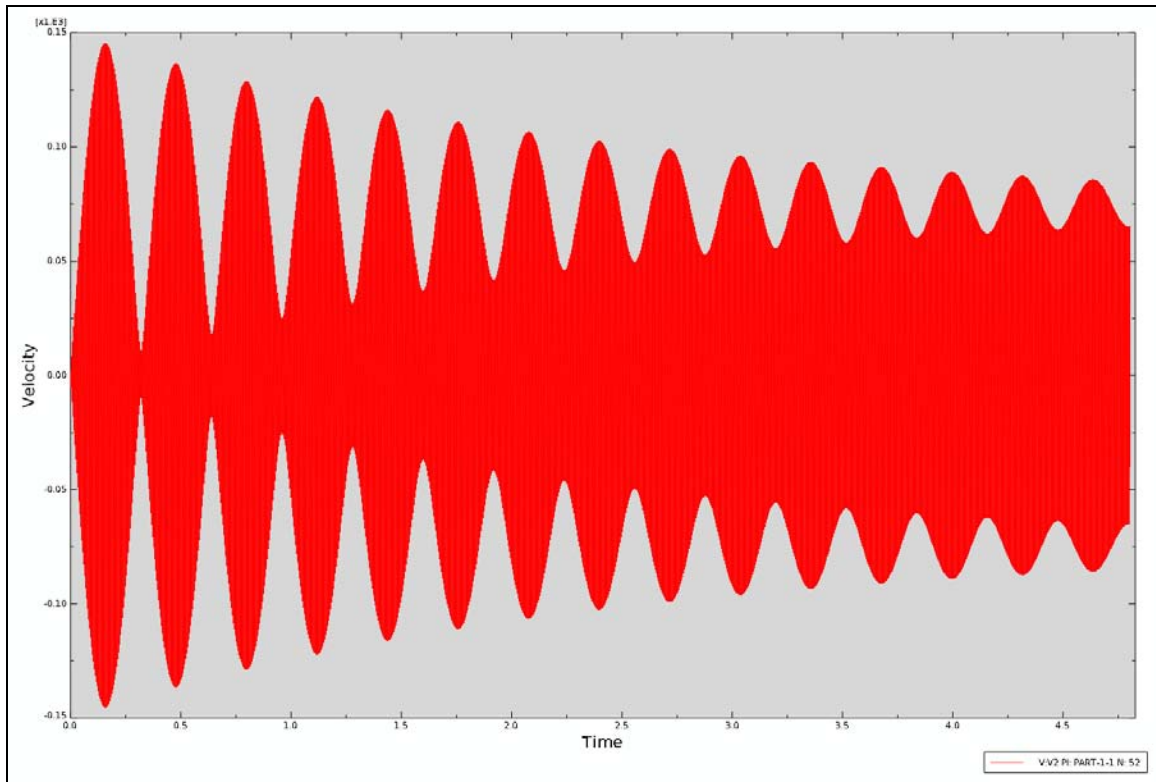
**Figure 83: FEM - Coated Beam response**
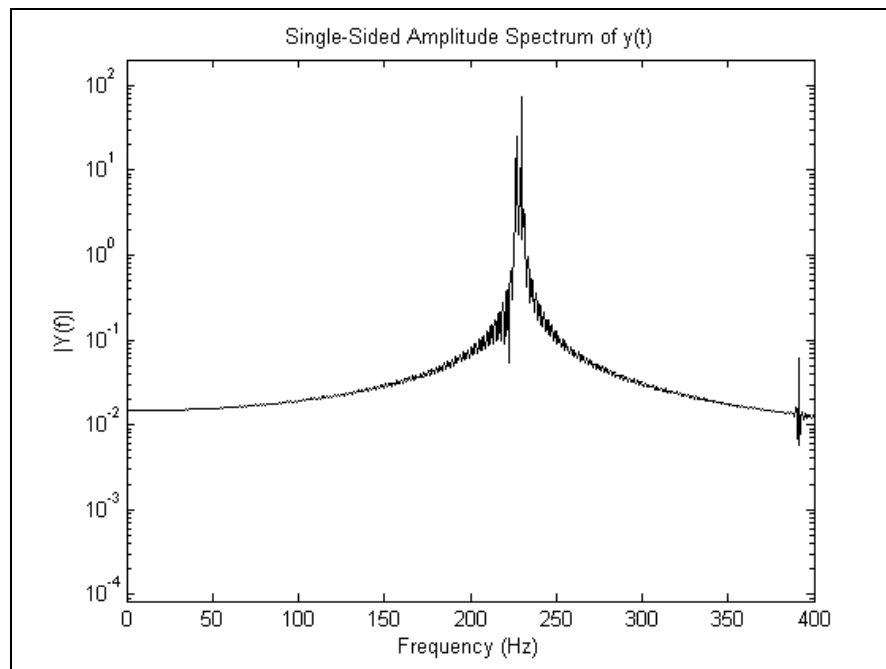


**Figure 84: Coated Beam - PSD**

Since steady state is not conclusively reached, an approximation is made using Figure 85. This extrapolation was done by plotting the peaks of the repeating curves in Figure 83 versus the time that they occur. Next a polynomial curve fit is used and extrapolated in an attempt to approximate when steady state would occur if the simulation continued at its present rate of approaching steady state. The assumption is that this rate continues in a similar fashion. If this assumption is valid then steady state is predicted to occur at approximately 5 seconds with a velocity value estimated at 85 mm/sec. The 'A' value used in the coated FEM was 2.02 N m versus the 0.35 N m calculated using the acceleration approximation method described above. This ratio was applied to the 85 mm/sec and results in a value of 14.7 mm/sec.
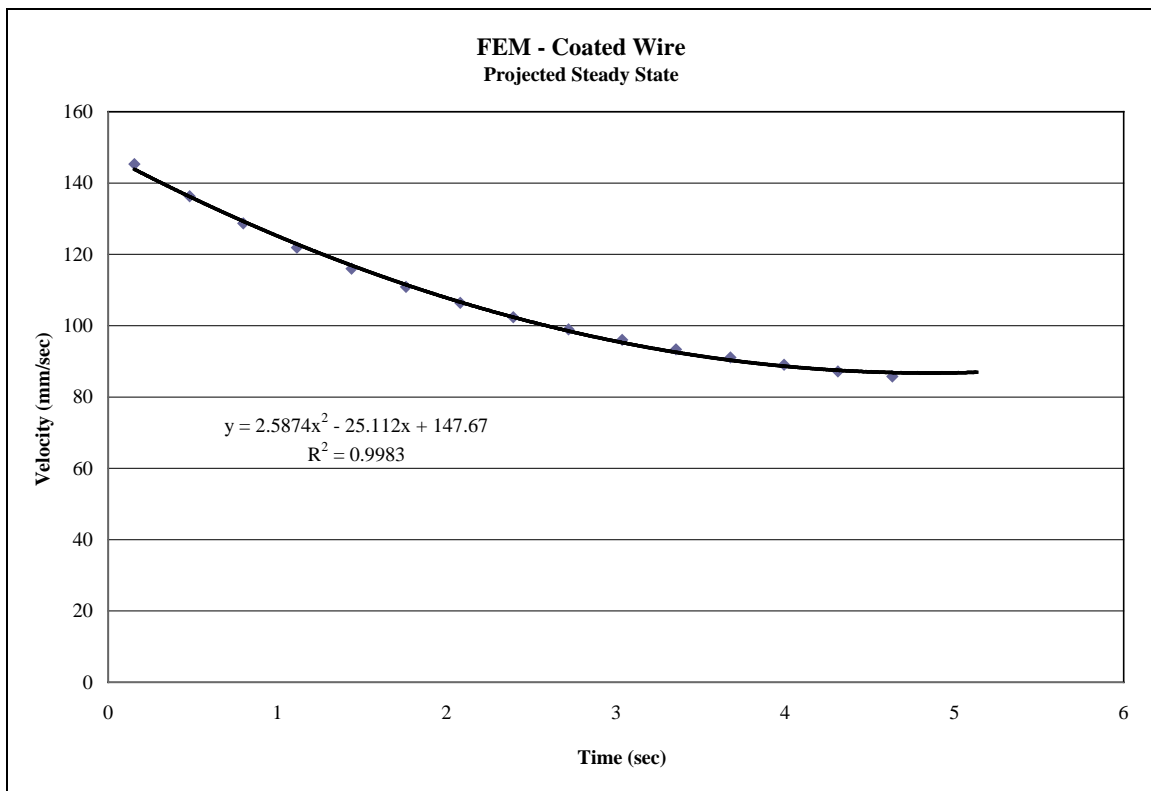


**Figure 85: Coated FEM - Projected Steady State**

This value is compared to the experimental values at 50 mV and 100 mV and to the calculated value at 10 mV in Figure 86 which also includes a few of the other experimental results at different voltages. The 10 mV curve is a calculated curve and not experimental data. It is seen that the velocity value calculated using the FEM is greater than the velocity value calculated using the method described above. The magnitudes of the differences are in mm. This indicates that the linear approximations made are reasonable.

If it were assumed that Figure 78 is approaching steady state, albeit at a slower rate than the coated FEM, another comparison can be made. By taking the peak velocity in Figure 78, and realizing that the velocity will never approach zero, an upper bound can be placed on the bare beam FEM solution. This would correlate with an experimental voltage of 100 mV. This correlates to the coated response shown as a red line in Figure 86. At 230 Hz this equates to a velocity of 26.1 mm/sec. This remains below the coated FEM projected velocity of 85 mm/sec.
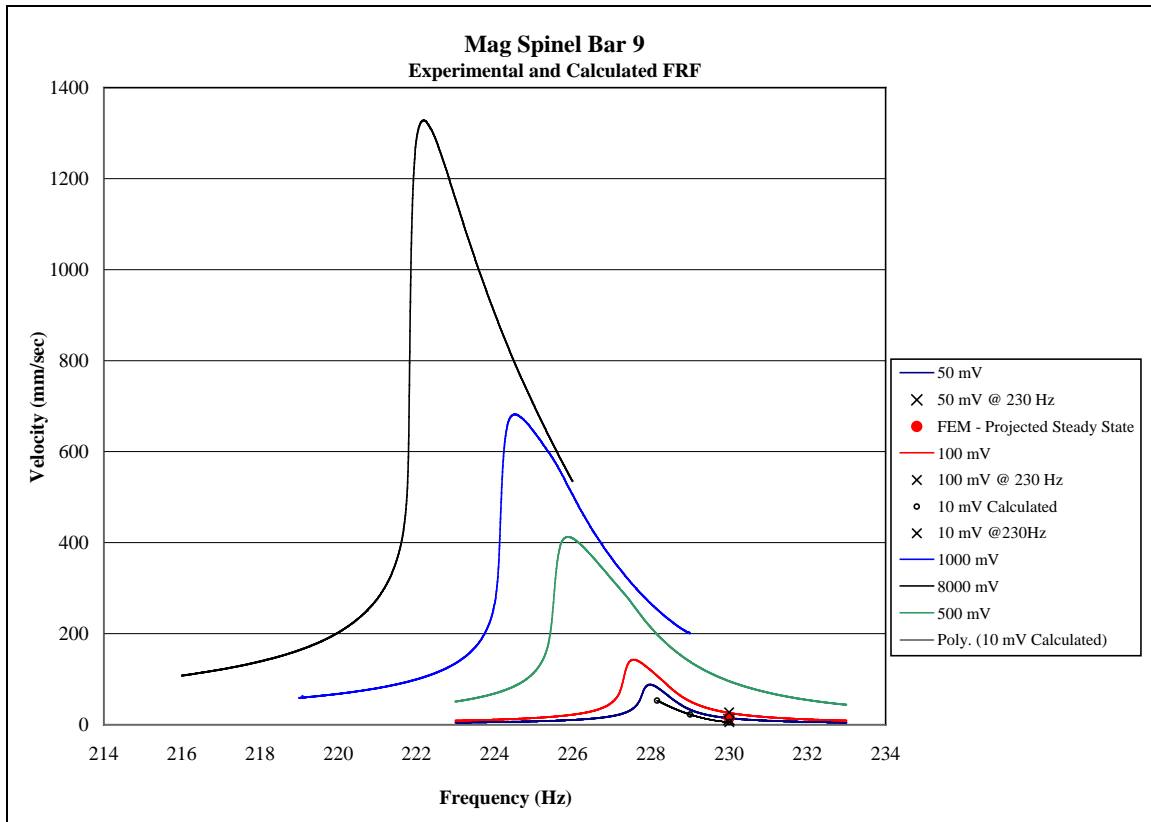
**Figure 86: Experimental & FEM FRF comparison**

The results show that the FEM requires greater stiffness to better approximate the coated

specimen's behavior.

# VI. Conclusions and Recommendations

## *Conclusions*

The findings of this research show that the characterization of TBC's continues to increase in accuracy. Following up on coated plates research, the approach used by Reed and Pearson uncovered characterization issues that other approaches only hinted at. By minimizing boundary condition energy dissipation as well as air damping, the material's underlying damping behavior could be better understood. The results of the research lead to several conclusions regarding the approach used in the previous work.

1) The ANSYS model was too stiff.

2) The Bare Beam modulus did compensate for the monofilament wires and magnets effect

3) Half-Power bandwidth introduces error due to its use for this non-linear system

4) Bare beam sweep rate performed by Pearson (2008) was too fast to estimate the loss factor for the Ti-6Al-4V beam using the half-power bandwidth method

5) Location of the monofilament wire supports does affect the experimental results

6) The procedure developed by Reed (2008) provides reasonable results

7) The phenomenological approach needs to be superseded by a constitutive approach

The FEM used in the developed procedure to approximate the material properties is clearly important. Although the approach is robust several errors can be introduced

through this path. The errors are associated with the inputs to the FEM and with measurement error which dictate those parameters. In this case the ANSYS model used was stiffer than the ABAQUS model. This was due to the element used, the mesh density i.e. aspect ratio, and even possibly the software itself. This last point cannot be conclusively proven without the actual ANSYS FEM that was used, for detailed examination.

The results also show that the bare beam modulus did well in compensating for the monofilament wires and magnet effects in the set-up. We have seen that the ANSYS model was too stiff, but the errors were minimized by "softening" the structure using the beam modulus. However, the change in modulus could not entirely compensate for the overly stiff FEM since only the frequency was matched without investigating the strain.

The results obtained by Pearson were based on the half-power bandwidth. This method is sensitive to the FRF's recorded during the experiment. An attempt to "merge" the upsweep and downsweep data was made with decent results for the coated beam. It is clear that $\eta_{sys}$ strongly influences the calculation of $\eta_{coat}$. The loss factor is estimated with the half-power bandwidth method which itself is based on linear assumptions. This requires the use of compensation techniques that introduce a certain amount of error.

This research has shown that the sweep rates used to estimate the loss factor of the bare beam was too fast. This explains the different results reported by Reed and Pearson of 0.0004 and 0.0008 respectively.

The supports made use of by the experimental set-up consisted of monofilament wires that were positioned at the node points of the beam's first bending moment. These

positions were approximate and varied from specimen to specimen. This research has shown that although this results in slightly different material properties for the coatings they were a minor source of error in the results. However, stiffer springs in the FEM caused a jump in the frequency of the first bending mode of the beam. This is akin to the specimen impinging on the magnet in the longitudinal direction resulting in rigid body modes. This effect would be seen in the experiment however, resulting in a reset of the monofilament wires prior to recording data.

It is clear from the variations of the parameters used in this analysis that the procedure produced reasonable results. Varying the parameters did change the results but they were not dramatic and were approximately linear giving confidence that the results are valid over their range. In addition, the FEM produced a result from a forced response that was not unreasonable. Although different from the values predicted, the magnitude of the difference was on the order of millimeters. This indicates that the linear assumptions made were useful in approximating the behavior of the non-linear coating mag spinel.

The approach taken serves to better characterize the material properties of mag spinel. However, its phenomenological approach makes it difficult to fully characterize these types of materials. Numerous variables are taken into account to utilize this procedure; unfortunately there are numerous others that were not. For instance the specimens went through numerous cycles in an attempt to "break-in" the material for more consistent results with success, but the time between tests seems to have an effect on the response that would be difficult to account for in an experiment of any reasonable length (Reed

2007, Pearson 2008).  The underlying physical structure of these materials that lead to

their dissipation of energy needs to be characterized with a constitutive model that can

better explain the various idiosyncrasies that they exhibit.


## *Recommendations*


There are several recommendations as a result of this research.  First is that the

tension in the monofilament wires needs to be measured in order to provide better

confidence in the FEM.  This was an unknown that led to approximations that may

introduce error to the results.

The second recommendation is that a scanning laser should be used to

characterize the different modes experienced by the specimen as it is undergoing the

forced response.  There may be modes that are occurring and dissipating energy that are

unseen due to the limitations of taking data from one position.

Another recommendation is to research if the window material in the vacuum

chamber interfered with the readings taken by the laser.  In particular, a scanning laser

would need to record at different angles rather than the perpendicular angle used in

Pearson's research (2008).

In order to properly characterize the material properties of mag spinel it is

important to "break-in" the material.  The material properties change with strain but seem

to approach an almost steady value at higher strains.  Finally, the higher voltage cases for

the coated specimens should be tested to the same higher frequencies as the lower voltage cases.

This FEM could be used to study thermal stresses in the structure.  Although the boundary conditions are approximately free-free, the coating has a different thermal expansion coefficient than the Ti-6Al-4V underlying beam.  This causes stresses that should be studied.

# Bibliography

*ABAQUS User's Manual* (2008) (v 6.8-2) Dassault Systèmes, 2009

Allen, K. S.  *Evaluation Techniques for Determining Damping Mechanisms on Titanium Plates*. MS Thesis, AFIT/GAE/ENY/05-M01.  Graduate School of Engineering and Management, Air Force Institute of Technology (AU), Wright-Patterson AFB OH, March 2005 (ADA436467).

*ANSYS Theory Reference for ANSYS and ANSYS Workbench* (2008) (v 11.0) ANSYS Inc 2009

Blackwell, C., Palazotto, A., George, T. J., and Cross, C. J.  "The Evaluation of the Damping Characteristics of A Hard Coating on Titanium," *Shock & Vibration, 14*(1): 37-51 (2007).

Bishop, J. E. and Vinra, V. K., "Some Improvements in the Flexural Damping Measurement Technique,"  *M³D:  Mechanics and Mechanisms of Material Damping, ASTM STP 1169,* American Society for Testing and Materials, Philadelphia, 1992, pp. 457-470.

Cook, R.D., Malkus, D.S., Plesha, M.E., and Witt, R.J. *Concepts and Applications of Finite Element Analysis 4ᵗʰ Edition,* NY: John Wiley & Sons Publishing, 2002

Cowles, B. A.  "High Cycle Fatigue in Aircraft Gas Turbines - An Industry Perspective," *International Journal of Fracture, 80*(2-3):  147-163 (1996).

Ivancic, F., and Palazotto, A.  "Experimental Considerations for Determining the Damping Coefficients of Hard Coatings," *Journal of Aerospace Engineering, 18*(1): 8-17 (2005).

Johnson, C. D., Kienholz, D. A., and Rogers, L. C., "Finite element prediction of damping in beams with constrained viscoelastic layers," *Shock Vibration Bulletin,* vol. 51, pt. 1, pp. 71-81, May 1981.

Lee, D. W.  *Evaluation of Factors Contributing to Damping of Coated and Uncoated Titanium Plates*.  MS Thesis AFIT/GAE/ENY/06-M06.  Graduate School of Engineering and Management, Air Force Institute of Technology (AU), Wright-Patterson AFB OH, March 2006 (ADA449409).

Limarga, A. M., Duong, T. L., Gregori, G., and Clarke, D. R.  "High-Temperature Vibration Damping of Thermal Barrier Coating Materials," *Surface & Coatings Technology, 202*(4-7):  693-697 (2007).

Miller, R.A. "Thermal barrier coatings for aircraft engines: history and directions," *Journal of Thermal Spray Technology: Chemistry and Material Science,* 6(1): 35-42 (1997).

*MatWeb Material Property Data*.  Retrieved February 20, 2009, from http://www.matweb.com/search/DataSheet.aspx?MatGUID=a0655d261898456b958e5f825ae85390 Titanium Ti-6Al-4V (Grade 5), Annealed

Patsias, S., Tassini, N., and Stanway, R.  "Hard Ceramic Coatings: An Experimental Study On A Novel Damping Treatment," *Smart Structures and Materials 2004, Damping and Isolation, 5386*(1):  174-84 (2004).

Pearson, Lindell. E.  *Vibration Analysis of Commercial Thermal Barrier Coatings*.  MS Thesis AFIT/GAE/ENY/08-J05.  Graduate School of Engineering and Management, Air Force Institute of Technology (AU), Wright-Patterson AFB OH, June 2008.

Reed, Shad. A.  *Development of Experimental, Analytical, and Numerical Approximations Appropriate for Nonlinear Damping Coatings*.  PHD Dissertation AFIT/GA/ENY/DSY-07S.  Graduate School of Engineering and Management, Air Force Institute of Technology (AU), Wright-Patterson AFB OH, March 2007.

Shipton, M. and Patsias, S. "Hard Damping Coatings: Internal Friction as the Damping Mechanism," *Proceedings, 8th National Turbine Engine High Cycle Fatigue Conference*, Monterey, CA, April 2003.

Timoshenko, S., Young, D.H., and Weaver Jr., W., *Vibration Problems in Engineering 4th Edition.*  NY:  John Wiley & Sons Publishing, 1974.

Torvik, P. J.  "Damping of Layered Materials," AIAA-1989-1422, 1989.

Torvik, P. J.  "Analysis of Free-Layer Damping Coatings," *Key Engineering Materials, 333*:  195-214 (2007).

Torvik, P. J.  "Determination of mechanical properties of non-linear coatings from measurements with coated beams," *International Journal of Solids and Structures.* 46(2009) 1066-1077.

Torvik, P. J., Patsias, S., and Tomlinson, G. R.  "Characterising the Damping Behaviour of Hard Coatings: Comparisons from Two Methodologies," *6th National Turbine Engine High Cycle Fatigue (HCF) Conference.*  Jacksonville, FL:  (2001).

Walker, R. L. *Finite Element Solution: Nonlinear Flapping Beams For Use With Micro Air Vehicle Design*. MS Thesis AFIT/GAE/ENY/07-M26. Graduate School of Engineering and Management, Air Force Institute of Technology (AU), Wright-Patterson AFB OH, March 2007 (ADA449409).

*VibrationVIEW* (2007). (7.0.5 HFE ed.). Janison, MI: Vibration Research Corporation